SHIFTING THE BALANCE OF INFLAMMATORY AND PRO-RESOLVING LIPID MEDIATORS IN VOLUMETRIC MUSCLE LOSS INJURIES

A Dissertation
Presented to
The Academic Faculty

by

Thomas Colin Turner

In Partial Fulfillment
of the Requirements for the Degree
Doctor of Philosophy in the
Wallace H. Coulter Department of Biomedical Engineering

Georgia Institute of Technology
Emory University
December 2022

SHIFTING THE BALANCE OF INFLAMMATORY AND PRO-RESOLVING LIPID MEDIATORS IN VOLUMETRIC MUSCLE LOSS INJURIES

Approved by:

Edward A. Botchwey, PhD, Advisor
Wallace H. Coulter Department of Biomedical Engineering
Georgia Institute of Technology and Emory University

Matthew Spite, PhD
Medical School
Harvard
Center for Experimental Therapeutics and Reperfusion Injury (CETRI), Department of Anesthesiology, Perioperative and Pain Medicine
Brigham and Women's Hospital

Nick J. Willett, PhD
Phil and Penny Knight Campus for Accelerating Scientific Impact
University of Oregon

Andrés J. García, PhD
Parker H. Petit Institute for Bioengineering & Bioscience
George Woodruff School of Mechanical Engineering
Georgia Institute of Technology

Andrew S. Neish, MD
Department of Laboratory Medicine and Pathology
Emory University

Valeria T. Milam, PhD
Materials Science and Engineering
Georgia Institute of Technology

Date Approved: 9/21/2022

ACKNOWLEDGEMENTS

The first thing I thought of when thinking of writing these acknowledgements is the phrase – “it takes a village to raise a child.” I guess I am implying that this thesis is my child, but what I am trying to get at is that there is no way this thesis would have materialized without the constant support, help, and encouragement from quite literally a village of people. I first want to thank my advisor, Edward Botchwey, for all his guidance over the past 5 years. I really don’t I could’ve made it through this PhD program in any other lab or with any other mentor. Scientifically, Ed has always been a “big idea” kind of person and its these innovative and exciting ideas that kept me motivated and excited about our work. The ability to inspire me and motivate me to contribute to the scientific world is no small task and I will always appreciate Ed’s unique ability to do so. Maybe my absolute favorite part about having Ed as my mentor, is the random life advice that he would (regularly) share with me throughout the last few years. We could be in his office for 2 hours and have talked about science for ten minutes of that time. His obvious care and investment in all his students is something I admire. His mentorship will continue to impact the way I approach new challenges, whether scientific or not, and is one of the things I am taking from this PhD that I will value the most.

I am extremely grateful for the expertise and insight that my thesis committee has given me, which includes Drs. Matthew Spite, Nick Willett, Andrés García, Andrew Neish, and Valeria Milam. Their unique take on different directions and approaches to the work and constructive feedback has helped mold my thesis work into what it is and has certainly increased the impact of it. Each individual committee member has provided invaluable input into my thesis, but I want to particularly thank Drs. Andrés García and Nick Willett for having to deal with me on a pretty regular basis for the past five years and in helping me achieve the work presented in the thesis.

Apart from the numerous collaborations that I have had with both of their labs, their scientific and professional advice has also gone a long way in impacting the scientist I am today and hope to be in the future. It is also the conversations that I have had with both Nick and Andrés away from science and their general advice that I appreciate immensely. Funny enough, upon getting engaged I received emails from both out of the blue congratulating me and my fiancée on our engagement – a little anecdote that describes the wonderful person both of them are and the awesome relationship I have with both of them and that I hope to continue to have.

Next, I would like to thank the staff at BME, IBB, and in the PRL for their assistance in allowing the research community to operate smoothly and produce fantastic work. Specifically, the PRL facility and all their staff, especially Andera Gibson and Dr. Richard Noel. The work the PRL staff performs to take care of our animals 24/7 including holidays has never gone unnoticed to me and is something I am immensely grateful for. I would not have been able to perform any of this work without their continuous dedication.

I next want to thank my labmates for their friendship, support and advice throughout my time in the lab. There have been many times that I have been quite stressed, needed to vent and someone to pretty much just agree with all my complaints. I want to thank them for always dealing with my disastrous organization, messy lab bench, hectic scheduling and yet always being ready to help and provide advice when needed. First, I want to thank a few former Botchwey lab members, Drs. Molly Ogle, Cheryl San Emeterio and Caitlin Sok, for pretty much teaching me everything I know and being the cornerstone of quite literally all the work done in this thesis – none of this would have been possible without them. This work builds on the fantastic work achieved by both Cheryl and Caitlin and their ability to balance finishing their thesis with teaching me and helping me build my thesis I appreciate now more than ever. I am not sure I know someone with more knowledge and technical expertise in the field as Molly. If I ever needed a question answered (which was often) Molly was always the first person I thought of because she pretty much has the answer to everything. I am so grateful to her for always taking time to answer my questions in ways that I could understand and build upon. Finally, to the current students, Daniel, Melody, Lechuan, Jasmine, Dre, who continue to make the Botchwey lab the best lab at Georgia Tech and who will, no doubt, continue to produce impressive work.

I have had many students from collaborating labs who have been integral in this thesis. First and foremost, Chapter 5 in this thesis could not have happened without Dr. Shannon Anderson. Shannon taught me the quadriceps VML model used in the chapter, and I always enjoyed her continuous help and friendship in lab and out of lab. Huge shoutout to Julia Harrer for flying out here all the way from Oregon for less than 48 hours just to help with functional testing and Dr. Luke Mortensen and his student Tianyi Zheng for their SHG analysis and generating my favorite images in this thesis. Special thank you to my undergrads throughout the years – Frank Pittman, Monica Behara, Natalie Van Slyke, Eeman Uddin , Mashoor Ahammed (special thanks for working overtime on some analysis) and Brendan Tan Fahed. Being a mentor to undergrads has been one of my favorite parts of being a PhD student. In particular, I want to thank Frank Pittman who I had the joy of mentoring for 4+ years. He was involved in much of this work, and I am so happy that he is able to pursue a PhD himself in the Willett lab and have nothing but confidence he will be able to achieve anything he puts his mind to.

I have so many friends and family who I am forever grateful for who have given me love and support through these long years of school. First, to all the friends I have made throughout grad school (both in school and out of school) and put up with my many complaints and are always ready to have a great time. In particular, I want to thank Jason Wan for keeping me sane and being the best friend I could ask for ever since the first day in Core 1. A huge thank you to my parents for making everything I do and achieve possible by their constant sacrifice and work. I am the person I am today first and foremost because of your love and support. Being just two hours away from you during my time in grad school has been a huge blessing and appreciate the countless things you do for me always. I have the best role models I could have possibly asked for – my brothers Paul and Chris. I constantly try to live up to the people that you are and am eternally grateful for your inspiration, advice and friendship. Paul played a large part in my decision of coming to Atlanta as he was already living here. Thank you for always being there for me, letting me live with you for so long and raising a puppy with me. That leads me to the obligatory dog shoutout – thank you Rey for being adorable and always bringing a smile to my face.

Finally, unquestionably the best thing to have happened to me in grad school is meeting my future wife - Lauren Hymel. There is nothing that brings me more joy and happiness than her presence in my life. Her positivity, happiness and smile is infectious and I could not have made it these past five years of grad school without it. Add that to the fact that she is also conveniently in the Botchwey lab and was always down to go to a bar immediately after a long meeting with Ed to “decompress”. We sit next to each other and are with each other at work and after work and I wouldn’t have had it any other way. This thesis should absolutely have her name on it as well because there is not a single experiment in it that she wasn’t an integral part of, or paper published that she is not on. She is one of the smartest people I have met and her ability to think creatively, critically, and impactfully has added immeasurable scientific value to the work in this thesis. I could write pages and pages thanking you but just know that meeting you is what made the past 4 years of my life the best ones yet. I cannot be more excited to build a life with you full of adventures and unending happiness.

Table of Contents

LIST OF FIGURES

LIST OF SYMBOLS AND ABBREVIATIONS

AA Arachidonic acid

AT-RvD1 Aspirin triggered resolvin D1

DHA Docosahexaenoic acid

ECM Extracellular matrix

eMHC Embryonic myosin heavy chain

EPA Eicosapentaenoic acid

FAPs Fibro-adipogenic progenitors

FPR2 Formyl peptide receptor 2

H&E Hematoxylin & Eosin

HPLC High-performance liquid chromatography

IFN-γ Interferon gamma

IGF-1 Insulin like growth factor 1

IHC Immunohistochemistry

IL-10 Interleukin 10

LC-MS/MS Liquid chromatography with tandem mass spectrometry

LXA Lipoxins

M1 Classically activated (pro-inflammatory) macrophages

M2 Alternatively activated (pro-resolving, pro-regenerative) macrophages

MAR Maresins

MPO Myeloperoxidase

MuSC Muscle stem cell

NET Neutrophil extracellular traps

NSAIDS Non-steroidal anti-inflammatory drugs

OA Osteoarthritis

PCTRs Protectin conjugates in tissue regeneration

PEG Poly(ethylene glycol)

PEG-4MAL Four-armed maleimide-terminated PEG

PLGA Poly(lactic-co-glycolic acid)

PMN Polymorphonuclear neutrophils

RvD D-series resolvins

RvE E-series resolvins

SHG Second harmonic generation

SIS-ECM Small intestinal submucosa extracellular matrix

SPADE Spanning-tree progression analysis of density-normalized events

TGF-β Transforming growth factor beta

TNF-α Tumor necrosis factor alpha

UMAP Uniform manifold approximation and projection

VEGFR Vascular endothelial growth factor receptor

VML Volumetric muscle loss

vWF Von Willebrand factor

SUMMARY

A major challenge in the care and treatment of traumatic injuries is designing a therapeutic strategy that is able to overcome the overwhelming inflammatory response and achieve functional tissue regeneration. More broadly, this is a challenge in the treatment of many chronic inflammatory conditions that is only exacerbated by an increasingly ageing population. There have been great advances made in the field of regenerative medicine approaches to traumatic injuries, but they have yet to achieve much clinical success owing to the complicated nature of treating traumatic, non-healing wounds. Much of the research as it relates to traumatic injury is focused on bone healing rather than the resulting soft-tissue loss, including volumetric muscle loss (VML). The current gold standard VML treatment is surgical reconstruction with muscle flap autografts or free tissue transfer. This often leads to excessive fibrosis and fatty infiltration that impairs regeneration and leads to significant long-term disabilities and chronic pain. Therefore, the need exists for therapies that are able to promote muscle regeneration, overcome long-term strength deficits and reduce chronic pain caused by traumatic, non-healing injuries that result in VML.

Innate immune effectors, including granulocytes (i.e., neutrophils, eosinophils, basophils, and mast cells), monocytes/macrophages, and dendritic cells, have attracted considerable attention for their roles in determining tissue repair outcomes after tissue injury. Essential roles have also been described for various immune cell subtypes, specifically neutrophils (aged and non-aged), monocytes (classical and non-classical) and macrophages (pro-inflammatory and pro-regenerative) in the regulation of vascular remodeling, innervation and remodeling of extracellular matrix (ECM). Moreover, heterotypic intercellular communication between immune effectors and tissue resident stem and progenitor cells establish the microenvironmental cues that are vital to successful regeneration and restoration of immune homeostasis after traumatic injury. This thesis

investigates key molecular mechanisms through which innate immune effector functions are dysregulated following VML injury and evaluates “pleiotropic” immune modulatory strategies to resolve inflammation and restore immune homeostasis as a novel means of treatment.

Recently, a superfamily of bioactive lipids has been discovered to be the molecular mediators and drivers of the active resolution of inflammation. The biosynthesis of these pro-resolving lipid mediators during inflammation has been intimately linked with a resolution of the inflammatory environment and return to homeostasis. Thus, we characterized this lipid mediator response in a pre-clinical model of traumatic volumetric muscle loss injury. We leveraged a pre-clinical quadriceps VML model where the injury size threshold between a healing and a non-healing defect has been characterized and determined. We compare the lipid mediator response between these two extents of VML injury to show that the non-healing VML injury exhibits an increased pro-inflammatory lipid mediator production. We follow these results up with an in-depth characterization of the concentration of lipid mediators up to 14 days throughout the inflammatory response to critical, non-healing VML injuries. Our comprehensive quantification shows a pathological deficiency in the ability of the local environment to produce pro-resolving lipid mediators that may be driving the persistent inflammation characteristic of VML injuries. With this in mind, we developed and characterized a novel pro-resolving hydrogel with the ability to promote the endogenous biosynthesis of pro-resolving lipid mediators and the resolution of inflammation.

To engineer an injectable biomaterial that activates local pathways of inflammation resolution, we used a synthetic hydrogel platform based on a four-arm poly(ethylene glycol) (PEG) macromer functionalized with maleimide groups for controlled delivery of SPMs. In this synthetic design, the maleimide in PEG-4MAL macromers were functionalized with thiol-containing cell-adhesive peptide (RGD) via Michael-type addition. These functionalized macromers are then crosslinked through the reaction of the remaining maleimides with cysteine-flanked protease-degradable peptides to yield a crosslinked hydrogel that is enzymatically degraded in vivo. This crosslinking reaction is performed in the presence of AT-RvD1 to encapsulate and locally release this SPM. This process generates a hydrogel delivery platform that is applicable to a wide range of injury contexts in which immune homeostasis is disrupted by severe tissue trauma

Using localized delivery of aspirin-triggered resolvin D1 (AT-RvD1), one such pro-resolving lipid mediator, we demonstrate that we can promote the resolution of inflammation following tissue injury. Local delivery of AT-RvD1 modulates the early infiltration of neutrophils and enhances vascularization and wound healing in different models of skin inflammation (dorsal skinfold window chamber and skin transplant models). We then expanded upon these findings and explored the effectiveness of this pro-resolving hydrogel in mediating the inflammatory response after VML injuries. Using LC-MS/MS analysis, we observe that pro-resolving hydrogel implantation after VML significantly increases the concentration of total SPMs 3-fold compared to vehicle control hydrogel. Specifically, the concentration of RvD3, RvD4, PCTR1, and AT-RvD1 are all increased at least 2-fold at 3 days post VML with local AT-RvD1 delivery. Pseudotime analysis of single cell flow cytometry profiles of infiltrating immune cells showed that local AT-RvD1 delivery limits the infiltration of neutrophils while promoting the accumulation of pro-regenerative mononuclear phagocytes. This is a shift away from the persistent pro-inflammatory and fibrotic response that is characteristic in non-healing VML injuries. Given that ECM remodeling is driven by FAPs, we also isolated muscle cells in vitro to show that AT-RvD1 may act directly on FAPs to reduce their fibrotic differentiation. Furthermore, whole mount immunohistochemistry at 14 days post VML reveals that local AT-RvD1 delivery promotes

muscle regeneration to achieve a 90% increase in defect closure compared to untreated vehicle control hydrogel. Additionally, second harmonic generation imaging shows that pro-resolving hydrogel treatment after VML injury results in increased collagen and muscle fiber organization at 14 days post VML. Finally, we assessed the ability of the local AT-RvD1 delivery strategy to recover muscle function after traumatic VML injury and found a striking recovery in muscle function with pro-resolving hydrogel treatment achieving 85% of the force compared to a healthy muscle while untreated VML injuries are only able to achieve 50% force compared to healthy muscle.

This research presents an important characterization of the lipid mediator response to volumetric muscle loss injury that is informative to future therapeutic design for traumatic injury treatment. Furthermore, we develop a novel pro-resolving hydrogel system that may aid in promoting the successful resolution of inflammation in conditions with a persistent inflammatory response and may increase the functional regeneration of muscle after VML injuries. These findings represent an important step in designing immunomodulatory treatments focused on activating local resolution pathways to restore tissue function.

CHAPTER 1. INTRODUCTION AND SPECIFIC AIMS

1.1 Introduction

Extremity trauma involving large tissue loss presents a significant clinical challenge for both general and military populations. In challenging cases resulting in volumetric muscle loss (VML), the current gold standard treatment is surgical reconstruction with muscle flap autografts or free tissue transfer. However, excessive fibrosis and fatty infiltration frequently impair regeneration and lead to significant long-term disabilities and chronic pain. The molecular triggers induced by VML injury initiate a complex inflammatory response resulting in the recruitment, proliferation, and activation of a wide range of hematopoietic and non-hematopoietic cells including neutrophils, monocytes, macrophages, T cells, fibro-adipogenic cells (FAPs) and muscle stem cells (MuSC). Together these cells can produce opposing outcomes where their intercellular interactions result in chronic inflammation and pathological fibrosis, or inflammation resolution and muscle repair. However, there is a fundamental lack of understanding of the molecular pathways that determine repair and fibrosis outcomes in the hostile environment of VML defects and new therapies are needed for successful muscle repair.

Our team has developed a series of severe pre-clinical rodent trauma models of full thickness VML injury in the murine spinotrapezius and quadriceps muscle. In addition to the ability to test our therapeutic strategy on the two main mammalian muscle types, these models also hold many unique advantages including whole-mount imaging to visualize intact muscle architecture and robust functional analysis, respectively, while also performing similar cellular analysis to evaluate our treatment across muscle types . Preliminary data show that persistent macrophages reach between 50-60% of all cells in critical size VML defects, many of which express markers of an M2-like phenotype and high levels of pro-fibrosis mediators TGF-β and TNF-α. Our results also suggest that FAPs transition to an adherent and highly fibrotic phenotype expressing high levels of CD29 (β1-integrin) and low levels of CD184 (CXCR4).

We examined biosynthesis of inflammatory lipid mediators and specialized pro-resolving lipid mediators (SPM) that are critical determinants of wound repair using liquid chromatography mass spectrometry (LC-MS). Our analysis suggests that critical size defects contain only low levels of pro-resolving lipid mediators and comparatively high levels of proinflammatory mediators. Therefore, we leveraged a modular polyethylene glycol-maleimide (PEG-4MAL) biomaterial platform that can enable local release of a stable isomer of Resolvin D1 (aspirin-triggered resolvin D1 (AT-RvD1)) to promote the molecular and cellular resolution of inflammation after VML to improve functional muscle regeneration. Our hypothesis is that local stimulation of pro-resolving lipid mediator production and initiation of inflammation resolution via delivery of AT-RvD1 will decrease the persistence of pro-inflammatory and pro-fibrotic cell states in critical VML defects and improve muscle regeneration.

1.2 Specific Aims

Aim 1. To test the immunomodulatory effect of locally delivered AT-RvD1 in the context of tissue inflammation. Aim 1 examines the changes in immune cell recruitment, vascular remodeling, and associated wound healing after local treatment with AT-RvD1 following tissue injury. In Aim 1A, we will assess the effects of local AT-RvD1 delivery on neutrophil recruitment and polarization along with associated vascular remodeling in the murine dorsal skinfold window chamber by SPADE analysis of flow cytometry and whole mount immunohistochemistry (IHC). In Aim 1B, the effects of hydrogel-mediated delivery of AT-RvD1 on pro-inflammatory and pro-resolving mononuclear phagocytes will be assessed via SPADE analysis of flow cytometry in a murine skin transplant model.

Aim 2. To quantify the pro-inflammatory and pro-resolving lipid mediator biosynthesis after VML injury and its modulation via PEG hydrogel-based delivery of AT-RvD1. Aim 2 characterizes the lipid mediator response after critical VML injury and its modulation via local AT-RvD1 delivery. In Aim 2A, we will use liquid chromatography-tandem mass spectrometry (LC/MS-MS) analysis to quantify the concentration of pro-inflammatory eicosanoids and pro-resolving mediators post VML and their modulation via the pro-resolving hydrogel treatment. In Aim 2B, we deliver AT-RvD1 containing PEG-4MAL hydrogels into the murine VML defect and compare the modulation of local immune cell infiltrate and muscle progenitor cells. In aim 2C, we leverage whole-mount IHC and SHG imaging to observe the changes in muscle regeneration and collagen organization after local AT-RvD1 treatment.

Aim 3. To evaluate the effects of local immunomodulation with pro-resolving PEG hydrogels on muscle regeneration after VML injury. Aim 3 investigates the effect of local AT-RvD1 delivery on the inflammatory cascade and associated enhancement of functional muscle regeneration after VML. In Aim 3A, we will use liquid chromatography-tandem mass spectrometry (LC/MS-MS) analysis to quantify the concentration of pro-inflammatory eicosanoids and pro-resolving mediators at various timepoints post VML. In Aim 3B, we will characterize the modulation of immune cell recruitment and polarization after pro-resolving hydrogel treatment in the pre-clinical quadricep VML model. In Aim 3C, we will analyze the effects of local AT-RvD1 on muscle regeneration via quadricep cross-section H&E and IHC. In Aim 3D, we will assess the ability of our treatment platform to improve muscle function after VML.

1.3 Significance

Extremity trauma involving large tissue loss (e.g., VML) presents a significant clinical challenge for both general and military populations. The frank loss of musculature characteristic of VML sufficiently disrupts or eliminates the wound's endogenous repair mechanisms, such that healing becomes very difficult usually resulting in substantial scar tissue formation; these injuries subsequently result in permanent functional impairments and chronic pain [1]. Given the lack of treatment options, many groups have investigated various tissue engineering approaches, including implantation of cellular/acellular scaffolds formed by *in situ* bioprinting, direct injection, or implantation of previously fabricated scaffolds that serve as immunomodulators of the injury milieu [2-4]. However, there is a lack of immunomodulation strategies that are designed to target specific dysregulated pathways of inflammation resolution that come about as a results of VML injuries. The roles of specialized pro-resolving lipid mediators (SPM) in the pathogenesis and treatment of VML is unknown. Our findings are among the first liquid chromatography mass-spectrometry profiling analysis of SPMs in an established pre-clinical model of VML that demonstrate the pathological deficiency in SPM biosynthesis. Furthermore, we show that the local and early presentation of AT-RvD1 via synthetic hydrogels significantly increases *in vivo* biosynthesis of multiple other SPMs and initiates a pro-regenerative shift in the immune cell composition in the muscle injury niche that leads to an increase in functional muscle regeneration after traumatic VML injury.

CHAPTER 2. BACKGROUND

2.1 The burden of volumetric muscle loss (VML), subsequent fibrosis and functional deficits.

Extremity trauma occurs due to a diverse range of scenarios spanning from high speed motor vehicle accidents to penetrating blast wounds and represents a significant healthcare burden [5]. These injuries often result in damage to multiple tissue types, with a notably high incidence of soft tissue trauma; many involving extensive damage to the muscle, and volumetric muscle loss (VML) [5]. VML can also occur in non-traumatic scenarios, including congenital birth defects, tumor resection, and diabetic ulcers [6]. The clinical gold standard for treatment of VML injuries is to cover the wound with autologous free flaps or rotational flaps, but these approaches achieve only limited success and result in tissue morbidity at the donor site [7]. Successful outcomes are typically restricted to thin superficial injuries and defects, while larger VML injuries are associated with significant mass loss, fibrosis, and fatty infiltration even after autograft treatment. Chronic functional deficits in patients treated with autogenous grafts have been observed at both 2 and 7 years, and severe pain can persist for decades thereafter [8].

New biomaterial-based strategies for muscle repair are an exciting treatment alternative for VML. Decellularized extracellular matrix (ECM), including skeletal muscle ECM [2], as well as porcine small intestine submucosa (SIS-ECM) [9] have limited pre-clinical success in restoring muscle function but still show significant fibrosis and fat infiltration. Various cell-material combinations have also been proposed to achieve muscle stem cells (MuSC) engraftment and the promotion of newly formed aligned functional fibers in thin and partial thickness VML defect models [3]. However, the inhospitable microenvironment of large volume skeletal muscle can overwhelm myogenic cells and often leads to fibrosis [10]. This “functional fibrosis” can serve in small defects as a matrix to protect the muscle from prolonged overload injury but may be insufficient when scaling up to larger defects and larger animal models (or humans) [11]. While these other regenerative engineering strategies under development remain promising, the clinical problems posed by the aberrant, pro-fibrotic host environment characteristic of VML injury remain unaddressed. Therefore, there is a critical need for improved regenerative intervention that will produce better long-term functional outcomes for patients after severe extremity trauma.

2.2 The proper coordination of immune cells is crucial for prompt and proper muscle regeneration after acute injury.

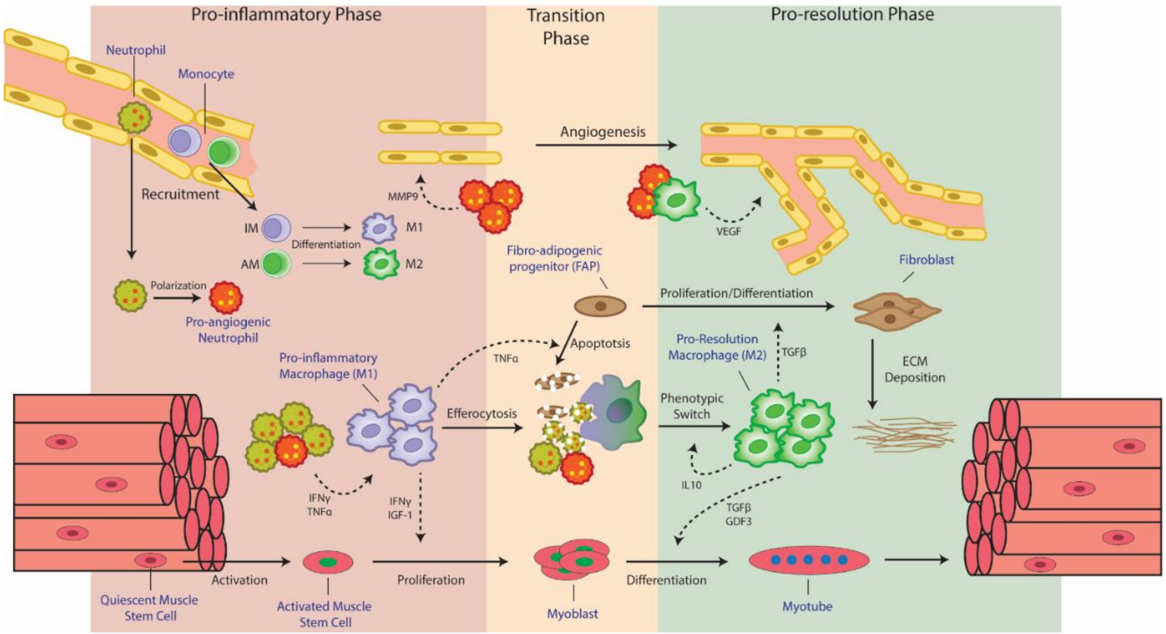

Figure 1. Inflammatory cascade after skeletal muscle injury.
Immune cell recruitment, polarization, and signaling outlined in the three main phases of inflammation – pro-inflammatory, transition and pro-resolution. The shift from pro-inflammatory immune cell phenotypes that act to potentiate MuSC proliferation to pro-resolution immune cell phenotypes that promote myotube and muscle fiber formation is shown.

Following injury, there is degeneration and necrosis of damaged myofibers [12], triggering the invasion of neutrophils, peaking within hours following injury and dropping off after 24 hours

[13]. Highly reactive aged neutrophils are diverted from clearance pathways in the bone marrow, liver and spleen to act “first responders” in injured muscles where initiate Toll-like receptor-4- and p38 MAPK-dependent signaling [14]. As neutrophils secrete tumor necrosis factor (TNF) and interferon-γ (IFN-γ), monocyte derived pro-inflammatory phagocytic (M1) macrophages infiltrate the muscle to aid in the removal of tissue debris and propagate pro-inflammatory signlaing by secretion of cytokines [15]. Both TNF- α and IFN-γ play a role in both macrophage induction and skeletal muscle regeneration by silencing Pax7 and preventing the expression of MyoD, maintaining MuSCs in an activated, proliferative state [15]. M1 macrophage secretion of TNF-α is also a mechanism to induce FAPs clearance by apoptosis [16]. By 4 - 7 days post-injury, there is a peak in pro-regenerative (M2) macrophages [15]. The transition to an interleukin-10 (IL-10) and TGF-β-rich environment corresponds with both a transition to M2 macrophage phenotypes as well as the differentiation and growth stages of myogenesis [17]. FAPs can also secrete MMP-14 and BMP-1 to drive macrophages towards an M2 phenotype. Additionally, insulin-like growth factor-1 (IGF-1) released by local macrophages during muscle regeneration has strong pro-myogenic effects [18].

Unfortunately, traumatic injuries, including VML, also disrupt dynamics of immune trafficking [19] with a sustained presence of CD4+ T cells and CD8+ T cells. Moreover, improper macrophage polarization results in macrophages that express the M1 and M2 phenotype simultaneously [20]. Additionally, a muscle microenvironment rich with both pro- and anti-inflammatory factors can also drive FAPs towards a pro-fibrotic phenotype. Because skeletal muscle is not well adapted to chronic injury stimulus, host mechanisms of inflammation resolution are unable to shift local immune cells from a transient pro-inflammatory state to an anti-inflammatory, pro-regenerative state [21]. Therefore, targeting of host inflammation resolution pathways in the muscle using locally-implanted biomaterials may be an effective strategy for achieving tissue regeneration after VML injury [22].

2.3 Bioactive lipid mediators are essential in orchestrating and regulating a self-limited inflammatory response.

After many years of research in which the termination of inflammation was thought to be a passive process involving the dilution of inflammatory mediators from the site of injury [23]. Numerous studies now demonstrate that the resolution of inflammation is an active response, largely mediated by the functions of bioactive lipids. The superfamily of bioactive lipids that actively reprogram the immune response to resolve inflammation and re-establish organ function are collectively termed the specialized pro-resolving lipid mediators (SPMs) [24]. After tissue injury or trauma, pro-inflammatory eicosanoids (prostaglandins and leukotrienes) are crucial in initiating the first stages of inflammation. These mediators, along with many cytokines, chemokines and complement components, stimulate the migration of neutrophils to the tissue [25].

As a part of the neutrophil-monocyte temporal transition, accumulated prostaglandins induce a lipid mediator class switch by switching on the transcription of enzymes required for the biosynthesis of SPMs ~ a superfamily composed of structurally distinct families of signaling molecules – lipoxins, resolvins, protectins, and maresins - derived from the conversion of omega-3 fatty acids [26]. Generally, the lipoxins and resolvins act to stop leukotriene-stimulated neutrophil influx and regulate nonphlogistic recruitment of monocytes. This triggers the production of other SPMs, such as protectins and maresins, that, along with lipoxins and resolvins, stimulate efferocytosis of apoptotic neutrophils and cellular debris by mononuclear phagocytes [27]. Increased efferocytosis also induces a phenotypic switch in macrophages from a pro-inflammatory M1 phenotype to a pro-regenerative M2 phenotype [24]. As macrophages shift from an M1 to an M2 phenotype, they also alter their metabolism from biosynthesis of pro-inflammatory eicosanoids to pro-resolving SPMs [28], producing a powerful feedback loop that further enhances inflammation resolution and leads to a restoration of homeostasis.

Imbalances in bioactive lipid mediator biosynthesis can lead to failed resolution that may underlie the persistent inflammation associated with many diseases or trauma [22], and there is growing appreciation of the pivotal role that SPMs play in wound healing and regenerative engineering. Resolution-pharmacology strategies, in contrast to traditional therapeutic strategies to antagonize the initiators of inflammation directly (e.g. cytokines and pro-inflammatory eicosanoids), harness endogenous resolution mechanisms to limit tissue destruction and fibrosis while also stimulating repair and regeneration [29-31]. Therefore, implications for understanding the SPM metabolism and cascade during muscle repair may hold the keys to developing a resolution-based therapeutic strategy to activate endogenous inflammation resolution mechanisms and regenerate muscle tissue after VML.

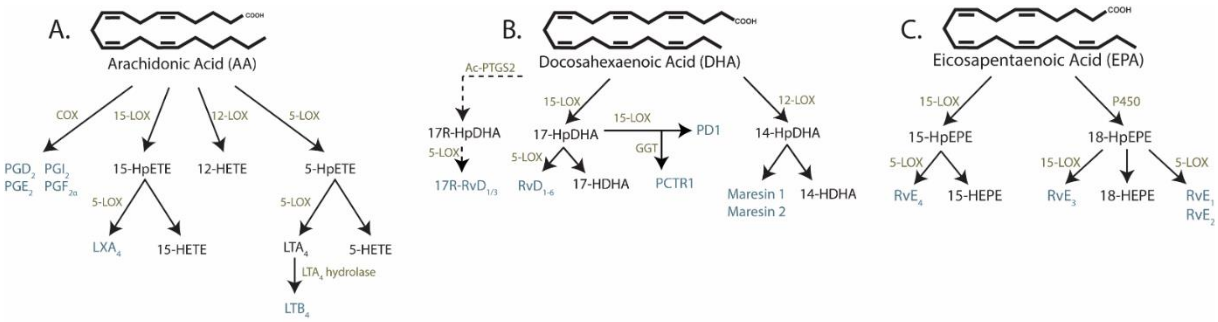

Figure 2. AA, DHA and EPA lipid metabolism.
A brief summary of the main enzymatic pathways derived from AA (A), DHA (B), and EPA (C) that generate the downstream pro-inflammatory eicosanoids and SPMs.

2.3.1 AT-RvD1: Origins and function

Docosahexaenoic acid (DHA) is the substrate for two groups of resolvins produced by different biosynthetic routes during the resolution of inflammatory exudates: 17S alcohol-containing resolvins (RvDs; via LOX-initiated mechanisms) and 17R alcohol-containing resolvins (17R-RvDs or AT-RvDs; via aspirin and COX-2 initiated mechanisms) [24]. Specifically, 17-R isomers of RvDs are produced when aspirin acetylates COX-2 to produce 17R-alcohol-containing intermediates that are then converted by 5-LOX [32]. In addition to aspirin, N-acetyl sphingosine, generated via a sphingosine kinase 1-dependent pathway, also acetylates COX2 to produce the 17R-RvDs [33]. Within this D-series resolvin family, Resolvin D1 (RvD1) and its 17R-isomer (17R-RvD1 or AT-RvD1) are the most extensively studied. They are both potent regulators of human and murine phagocytes at picomolar concentrations [34] These aspirin-triggered Resolvin D1 (AT-RvD1) molecules are particularly potent regulators of human and mouse neutrophils. Both RvD1 and AT-RvD1 stimulate macrophage phagocytosis of microbes, efferocytosis of apoptotic PMNs, promotes clearance of necroptotic cells, increases pro-resolving macrophage phenotype polarization, and increases regulatory T-cells [30]. AT-RvD1 exerts these actions on immune cells via the GPCR ALX/FPR2.

These compounds can be produced through total organic synthesis in which the synthetic compounds match the physical and biological properties of those enzymatically generated. The main difference between the two isomers lies in their *in vivo* half-life and bioactivity. The 17S alcohol on RvD1 rapidly converted enzymatically by eicosanoid oxidoreductase to 17-oxo-RvD1 rendering it inactive; however, when in the 17R alcohol configuration the molecule resists rapid inactivation allowing for a longer *in vivo* bioactivity [32, 35]. This specific advantage of AT-RvD1 holds powerful therapeutic potential for the reduction and resolution of inflammatory processes.

2.4 The therapeutic potential of specialized pro-resolving lipid mediators in regenerative medicine

Uncontrolled or persistent inflammation is a well-recognized root cause of disease and poor wound healing (e.g. osteoarthritis, traumatic injury, obesity, periodontitis, etc.) [19, 22, 36, 37]. The pursuit of successful "anti-inflammatory" treatments dates back to ancient physicians who employed willow bark decoctions and are aimed at blocking or antagonizing the onset of inflammation, when proinflammatory soluble mediators initiate the inflammatory cascade as a means of suppressing the inflammatory cascade [38-40]. However, the inhibition of key inflammatory pathways responsible for inflammation can also lead to immune suppression, collateral tissue damage and other unwanted side effects [38] enumerated below:

(1) NSAIDs: Chronic pain, stomach bleeding, cardiovascular/kidney toxicity

(2) COX2 Inhibitors: Increased risk of thrombosis, heart attack

(3) Anti-TNFα: Increase risk of infections

(4) Steroids: Osteoporosis, impaired wound healing, fungal infections, immunosuppressive

2.4.1 Modulation of SPM bioactivity and biosynthesis

Lipidomic analysis of human tissues in various models of inflammation has demonstrated the critical role and importance of SPM pathways in disease pathology and tissue healing [30]. In patients with rheumatoid arthritis, higher RvE2 concentrations in synovial fluid has been associated with reduced symptoms of arthritis [41]. Additionally, in tissue obtained from knee Osteoarthritis patients, RvD2 and other pathway markers of resolution were identified [42]. In an analysis of human atherosclerotic plaques, regions with significantly thicker fibrous caps, higher necrosis and increased reactive oxygen species had a marked decrease in the concentration of RvD1 [43]. In scleroderma, a condition characterized by persistent lung inflammation and fibrosis, analysis of patient bronchoalveolar lavage fluid compared to healthy patients revealed an imbalance of lipid mediators distinguished by deficient biosynthesis of SPMs compared to their pro-inflammatory counterparts [44]. These lipidomic studies, along with others reviewed in [22], reveal the importance of SPM pathways in human disease fuel the desire to develop new therapeutic approaches to harness these pathways in other significant clinical problems.

Recently, a model of surgically induced knee OA in high-fat-fed mice was leveraged to evaluate the effect of RvD1 administration on OA progression. Intra-articular treatment with RvD1 was shown to diminish the progression of OA in the knee joint, ultimately improving the severity of synovitis and cartilage degradation [45]. Moreover, intraperitoneal administration of LXA4 attenuated the progression of surgically induced OA in mice [46]. Pain is a major symptom of OA and is currently treated by NSAIDs and eventually opiates, both of which are associated with serious side effects. A study investigating the potential role of targeting the resolving pathway to modify OA pain uncovered that exogenous delivery of a D-series resolvin precursor to a rat model of OA pain effectively reversed established pain behaviour which was associated with significant elevation in levels of RvD2 [47].

The ability for SPMs to enhance tissue regeneration is of significant interest [48]. Various group have leveraged pre-clinical murine models of muscle injury to characterize the lipid mediator response [49-52]. In acute cardiotoxin and exercise induced muscle injury models, results have shown that the concentration of pro-inflammatory lipid mediators and SPMs are correlated with periods of inflammation and resolution/regeneration, respectively. Moreover, the administration of exogenous lipid mediators, namely RvD1 and RvD2, significantly improves muscle regeneration in both models of acute cardiotoxin induced and in models of Duchenne muscular dystrophy [50-53]. The mechanism by which SPMs increase muscle regeneration include both their direct actions on immune effector cell functions as well as their stimulation of resident progenitor cells to increase proliferation [52]. Similar results were seen in a model of aged bone fracture healing where the administration of increased bone deposition and resistance to fracture in the later stages of repair [54]. Given that extremity trauma involves damage to both hard and soft tissues; pro-resolving therapeutics hold considerable promise for treating complex musculoskeletal trauma leading to VML.

2.4.2 SPM-modified Biomaterials

Although SPMs are highly potent molecules, these endogenous ligands are highly prone to metabolic inactivation in vivo which often limits their effects with traditional delivery methods [55, 56]. Furthermore, SPMs carry out their functions via short-range signalling interactions [57]. Thus, the development of biomaterial-based platforms that both protect these lipids from being enzymatically inactivated and facilitate their local delivery is an exciting frontier for translation of resolution pharmacology strategies.

One of the first studies investigating the efficacy of local SPM delivery developed nanoparticles containing a Lipoxin A4 analogue using human neutrophil-derived microparticles. This pro-resolving nanomedicine was tested in a murine model of temporomandibular joint inflammation and was shown to reduce inflammation by limiting PMN infiltration and enhance the rate of wound healing [58]. These studies paved the way for the development of the “first generation” of SPM-modified synthetic materials that focused on the delivery of RvD1 via polymeric thin films to enhance vascular remodelling. A surgically adaptable, perivascular thin film PLGA device capable of unidirectional release of RvD1 to the vasculature was developed and shown to attenuate vein graft hyperplasia without associated toxicity in a rabbit carotid bypass model [59, 60]. Our lab previously developed PLGA thin films that facilitate the local and sustained delivery of AT-RvD1, a RvD1 analogue that possesses a longer in vivo half-life. Delivery of AT-RvD1 from degradable thin films compared to non-biomaterial mediated AT-RvD1 delivery was able to alter the tissue microenvironment after injury by limiting neutrophil infiltration and increasing the accumulation of Ly6C^{Low} monocytes [61].

Recently, we have seen further innovation towards the development of a “second generation” of SPM-modified biomaterial platforms. This includes lipid- and polymer-based nanoparticles for enhanced tissue or cell targeting and soft polymer materials that allow for combination delivery and cell encapsulation for cell therapies. In the nanomedicine space, polymeric nanoparticles encapsulated with RvE1 targeted to intestinal mucosa was seen to promote intestinal epithelial wound repair and, similarly, RvD1-loaded nanoliposomes formulated for intra-articular delivery showed an ability to prevent cartilage damage along with an analgesic effect [62, 63]. In our work contained in this thesis, pro-resolving soft materials have been fabricated using a PEG-4MAL hydrogel platform to achieve the delivery of AT-RvD1. This pro-resolving PEG hydrogel exhibits in situ gelation and is thus able to be directly injected to a site of injury or inflammation. Taken together, it is clear that SPM-modified biomaterials are an attractive approach for harnessing the potential of SPM therapeutics for novel regenerative immunotherapies.

CHAPTER 3. THE LOCAL DELIVERY OF ASPIRIN-TRIGGERED RESOLVIN D1 PROMOTES THE ACCUMULATION OF PRO-REGENERATIVE IMMUNE CELL SUBSETS THAT CONTRIBUTE TO THE PROCESSES OF INFLAMMATION RESOLUTION AND WOUND HEALING.

3.1 Introduction

Neutrophils have classically been viewed as a largely homogeneous population of myeloid immune cells that do not have the ability to polarize into subsets, unlike other leukocyte populations with multiple phenotypes, such as T lymphocytes or macrophages [64, 65]. Traditional neutrophil activities include phagocytosis, degranulation, and release of neutrophil extracellular traps (NETs) aimed at responding to and combating microbial invasions or tissue injury [66]. Neutrophils are considered the immune system's short-lived "first responders" to infection or injury with limited and well-defined responses [67]. While traditional neutrophil functions serve a beneficial role in containing infiltrating foreign cells, excessive neutrophil accumulation, degranulation, and release of NETs can contribute to tissue fibrosis, chronic inflammatory responses, and the development of diseases such as diabetes, atherosclerosis, and cancer [68]. Moreover, there is now emerging evidence for the existence of heterogeneous subsets within the larger neutrophil population that are able to carry out functions in both homeostatic and pathogenic immune responses in which they can actively contribute to regenerative processes following tissue injury [69, 70]. Specific subpopulations of neutrophils are also implicated in the early establishment of a healthy vasculature. Specifically, pro-angiogenic neutrophils, identified by their high expression of CD49d, VEGFR1 (vascular endothelial growth factor receptor 1), VEGFR2, and CXCR4, are efficiently recruited to non-vascularized tissues and are capable of inducing angiogenesis [71]. In addition, aged neutrophils, identified by their small size and increased expression of CD11b and CD49d, are highly reactive phenotypes that are long lived in the circulation compared with classical neutrophils and serve as first responders in inflammatory reactions [14]. We believe that a regenerative medicine approach that selectively targets specialized neutrophil subpopulations holds substantial promise.

Advancements in the understanding of the mechanisms that lead to the resolution of inflammation have also led to the discovery of proresolving lipid mediators that regulate key signaling events that are involved in inflammation resolution. One example of such proresolving mediators is resolvins, which are derived from both eicosapentaenoic acid (EPA) and docosahexanoic acid (DHA) [24]. Conversion of membrane lipids into specialized bioactive lipid mediators is a critical step in cessation of polymorphonuclear neutrophil infiltration and active resolution of inflammation [27]. Aspirin-triggered resolvin D1 (AT-RvD1) is a D-series resolvin, which only differs functionally from resolvin D1 in that it is resistant to rapid conversion and inactivation in vivo. Thus, with a relatively longer in vivo half-life, it is an attractive small molecule for sustained local delivery to reduce chronic inflammation and promote tissue regeneration [34]. We and others have shown that treatment with D-series resolvins is able to promote angiogenesis after both ischemic and nonischemic tissue injury while also reducing the damaging aspects of prolonged neutrophil interactions with implanted biomaterials [61, 72]. We believe that the application of advanced single-cell analytical techniques on traditional flow cytometry data could elucidate how nontraditional neutrophil functions may be targeted for immunotherapy using locally administered AT-RvD1 or other bioactive lipids.

Assessing the functional heterogeneity of neutrophil subpopulations based on surface marker expression profiles is notoriously challenging. Recent multicenter studies, such as the Immunological Genome Project, show that manual gating is one of the largest confounding factors when analyzing single-cell data-based experiments [73]. Innovative methods of dimensionality reduction are emerging to enhance the robustness of surface marker expression profiles of single cells and their association with functional cell states. In this chapter, we explore neutrophil heterogeneity in the context of sterile inflammation using murine dorsal skinfold window chamber as a model of excisional skin injury (Fig3 A). The window chamber allows for the longitudinal intravital imaging of the injury microenvironment and single-cell tracking of immune cell invasion in the presence or absence of sustained AT-RvD1 presentation [74]. The sustained AT-RvD1 delivery is accomplished using a poly(lactic-co-glycolic acid) (PLGA) thin film, which we have characterized in previous studies [61]. We used traditional "manually gated" immune populations, where regions of interest (manual gates) were drawn over a series of bivariate plots, for further analysis (Fig 3B). We used several advanced analytical techniques to identify a pro-angiogenic neutrophil subset that is involved in the early angiogenic process, which is important in the successful resolution of inflammation [71]. Because of its unique ability to resolve subtly different cell populations while preserving the global structure, we first applied uniform manifold approximation and projection (UMAP) for dimension reduction and unbiased cluster detection based on the canonical markers of innate immune cells (Fig 3C). We then performed a novel pseudotime analysis based on spanning-tree progression analysis of density-normalized events (SPADE) [75, 76] to reconstruct complex cellular hierarchies of immune cell transitions to reveal rare cell states and order single-cell expression profiles in "pseudotime"—a quantitative measure of progress through a biological process (Fig 3D) [77]. In addition, we classified each node to an immune cell subset and calculated the percent cell frequency of each population relative to the total number of events in each node. The response of these identified subpopulations to AT-RvD1

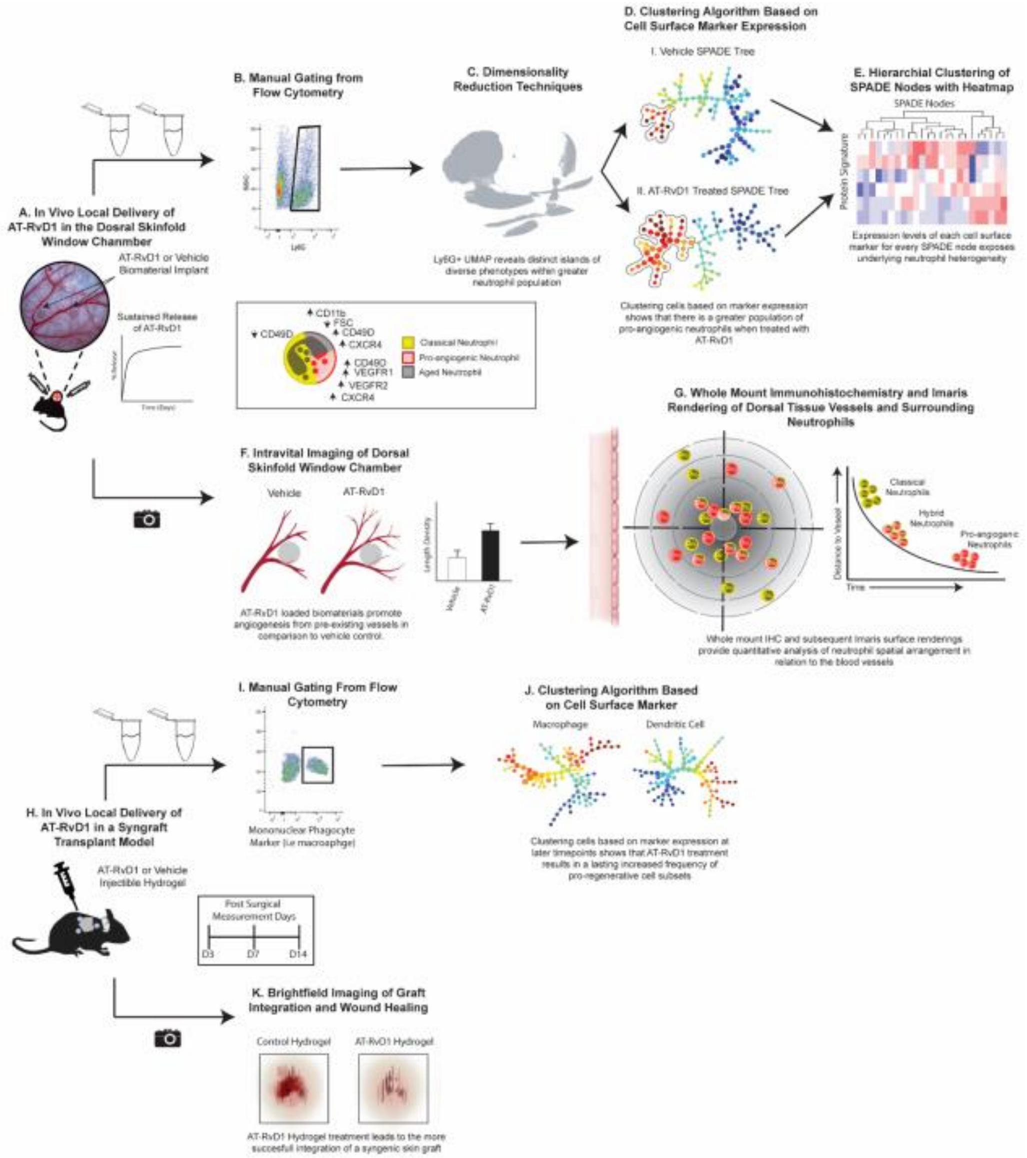

Figure 3. A model workflow for characterizing immune cell heterogeneity. Our approach utilizes high dimensional single-cell flow cytometry data and complementary dimensionality reduction algorithms to generate a 2D projection of immune cell heterogeneity (A to E). Subsequent steps infer a functional role for immune cell subsets based on spatial distribution of infiltrating cells within damaged tissues as well as responsiveness to AT-RvD1 treatment (A, F, and G). This approach is used in a different model and with a different delivery platform (H-K) to validate the therapeutic potential of AT-RvD1 delivery.

could then be analyzed within SPADE. Because every SPADE node carries its own unique surface marker expression combination, these can be compiled into a heatmap including every node on a SPADE dendrogram (Fig. 3E). In addition to the single-cell analysis, we performed bright-field imaging and whole mount immunohistochemistry to prescribe functional significance to the neutrophil subpopulations identified using SPADE (Fig. 3F and G). We developed a poly(ethylene glycol)–maleimide (PEG-MAL) hydrogel to deliver AT-RvD1 in the murine syngeneic skin transplant model (Fig. 3H). This model was chosen to chronicle wound healing and tissue integration over time (Fig. 3K) and validate biomaterial-mediated AT-RvD1 as a therapeutic approach. Macrophage and dendritic cell heterogeneity has been well characterized in the wound healing response, as M2 macrophages and IL10+ dendritic cell subsets specifically are notable for promoting a proregenerative injury milieu [78, 79]. Thus, to establish the rigor of our analytical approach, we identify macrophage and dendritic cell subpopulations using SPADE and investigate their response to AT-RvD1 treatment.

In this chapter, we show that local, sustained delivery of AT-RvD1 is able to selectively enrich injured tissue with pro-angiogenic neutrophils that have high expression of CD49d, VEGFR2, VEGFR1, and CXCR4 at the onset of the inflammatory response. Furthermore, we show that this shift in the early microenvironment increases the downstream accumulation of M2 macrophages, a pro-regenerative macrophage subset, and IL10+ tolerogenic dendritic cells, a dendritic cell subset responsible for activating regulatory T cells and graft tolerance [79]. Our findings demonstrate the importance of applying single-cell dimensionality reduction and pseudotime analysis techniques for the study of rare cellular heterogeneity. Moreover, it suggests that a novel small molecule–based strategy for enhancing early angiogenesis can be achieved through the targeting of a pro-angiogenic neutrophil subset, which is understudied due to the novelty of neutrophil heterogeneity and difficulty in analyzing neutrophil subset response to therapeutic perturbations [80].

3.2 Results

3.2.1 SPADE analysis identifies distinct pro-angiogenic neutrophil trajectories.

To investigate the role of inflammation progression and AT-RvD1 treatment on neutrophil heterogeneity in the blood and in the tissue, we created an array of UMAPs and SPADE dendrograms (Fig. 4). We collected blood and tissue samples at days 1 and 3 after surgery for both vehicle control and AT-RvD1 treatment groups. Using manual gating techniques, we selected CD11b+ cells as representative of myeloid cells and made UMAP and SPADE projections of this group of cells. By overlaying where the neutrophil population (depicted as red dots) lies on these projections, we show that regardless of time point and treatment, the circulating neutrophil population is constrained to a single island and, thus, is composed of a homogeneous group (Fig. 4A-D). However, when these neutrophils extravasate into the tissue, they show increased diversity, visualized by the spread of neutrophils among distinct clusters in the UMAP and in different trajectories in the SPADE dendrogram (Fig. 4E-H). In the tissue, neutrophil heterogeneity increases at day 3 and with AT-RvD1 treatment. When compared with day 1, the day 3 UMAP

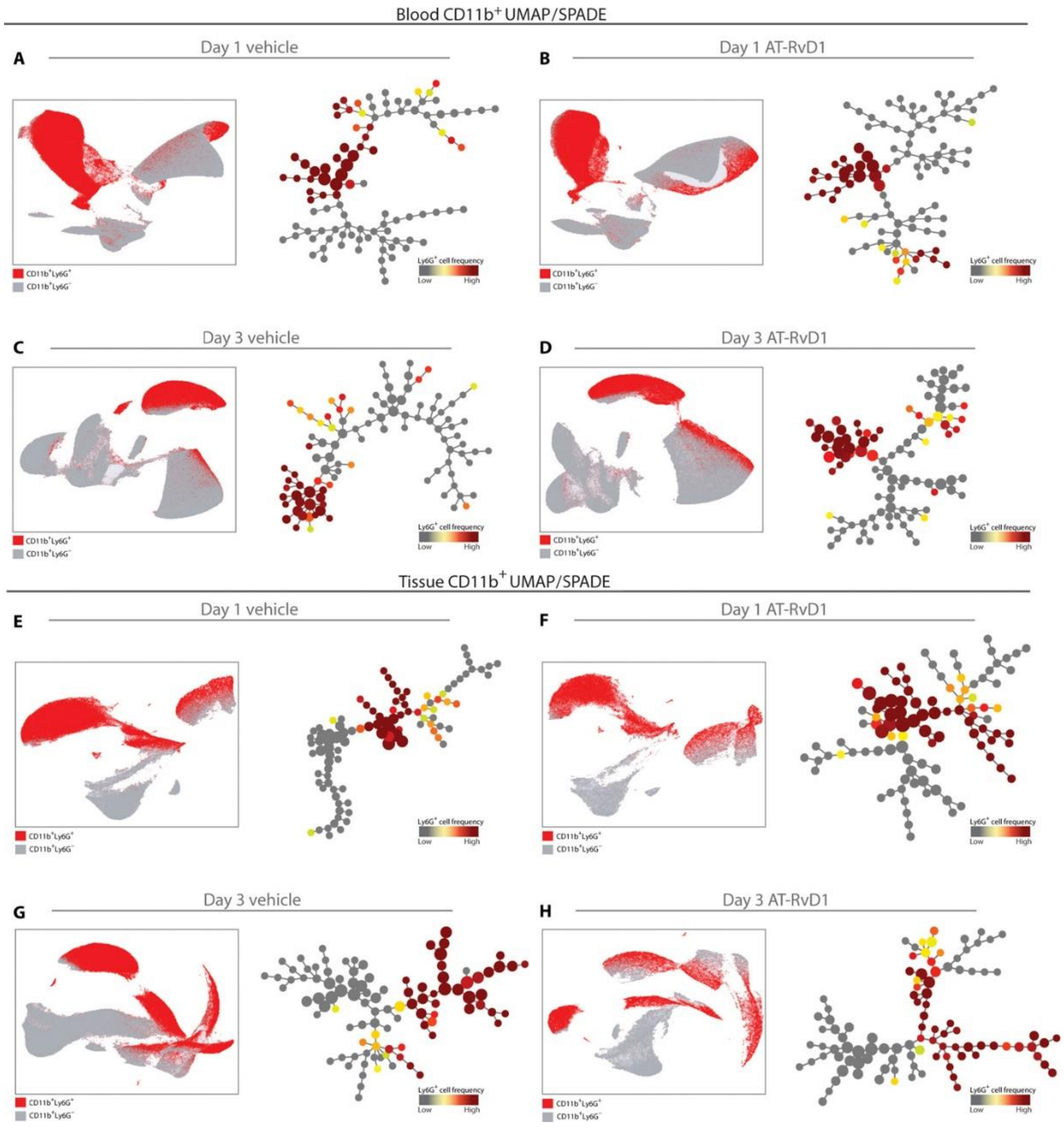

Figure 4. Visualization of neutrophil heterogeneity using UMAP and SPADE.
A traditional gating strategy in which live, single cells were analyzed using CD11b+ as a general myeloid cell marker, and Ly6G+ within the CD11b+ population as a neutrophil marker was used to visualize neutrophil heterogeneity in the myeloid cell compartment. UMAP (left) and SPADE (right) of CD11b+ cells analyzed from the blood (A to D) and tissue (E to H) with an overlay showing the location and frequency of Ly6G+ cells. With a limited set of markers, neutrophil populations are not constrained to a single homogeneous cluster on the UMAP, which would imply one population. Comparison of UMAP and corresponding SPADE-based pseudotime trajectory at day 1 after surgery with a vehicle control (A and E), day 1 after surgery with sustained AT-RvD1 treatment (B and F), day 3 after surgery with a vehicle control (C and G), and day 3 after surgery with sustained AT-RvD1 treatment (D and H). Each UMAP/SPADE was created with the pooled data of four mice.

shows a similar number of CD11b+ islands; however, the spread of Ly6G+ neutrophils among these islands is increased at day 3, which suggests an increased neutrophil heterogeneity. Similarly, at 3 days after surgery with sustained AT-RvD1 treatment, the UMAP shows neutrophils scattered among separate islands, and the SPADE pseudotime analysis shows the neutrophils progressing along separate trajectories while the vehicle control shows neutrophils clustered along one main trajectory (Fig. 4H). These results indicate that neutrophil heterogeneity is induced by local inflammatory signals along with lipid signalling pathways modulated by sustained AT-RvD1 treatment in the tissue microenvironment.

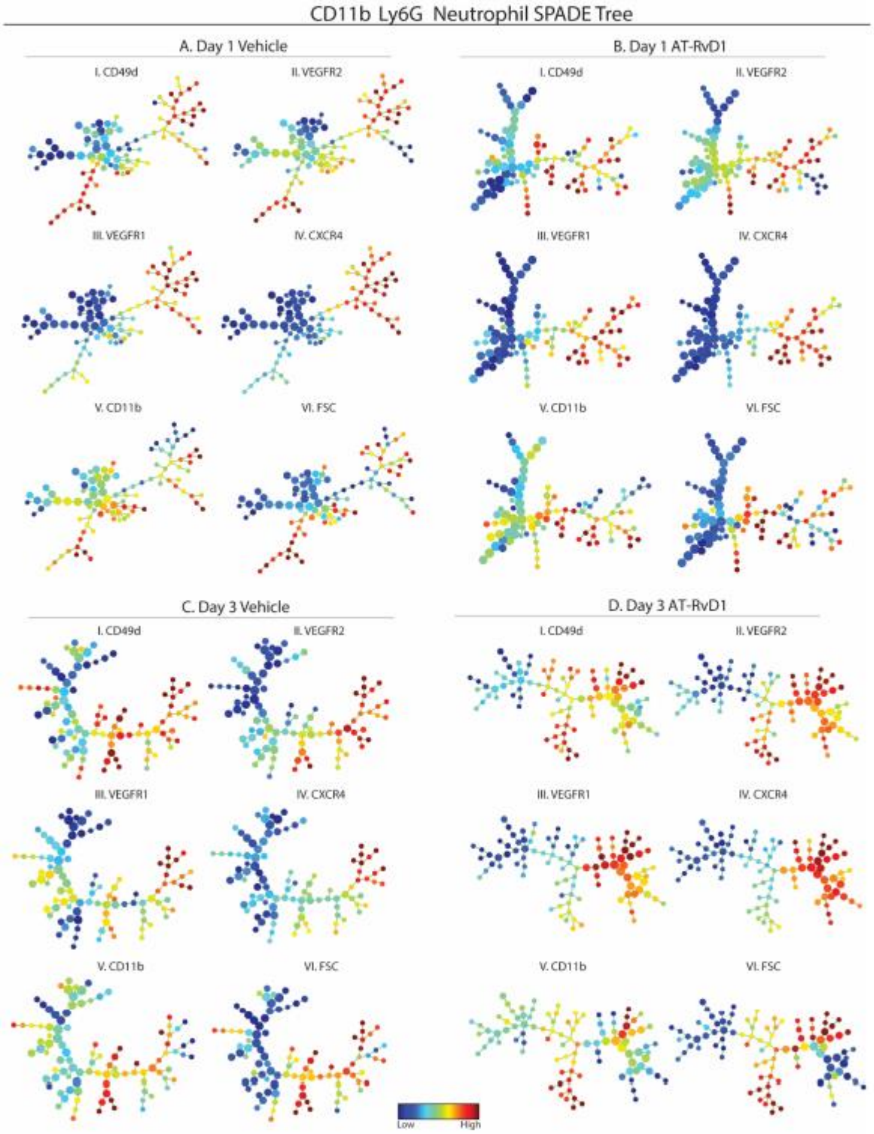

Figure 5. SPADE marker expression array informs neutrophil subset identification. Pseudotime analysis generated SPADE trees consisting of CD11b+Ly6G+ neutrophils from tissue at day 1 after surgery with vehicle control (A), day 1 after surgery with sustained AT-RvD1 treatment (B), day 3 after surgery with a vehicle control (C), and day 3 after surgery with sustained AT-RvD1 treatment (D). An array of six trees that have a marker expression heatmap overlay is generated for each condition (I-VI). The marker expressions shown are CD49d (I), VEGFR2 (II), VEGFR1 (III), CXCR4 (IV), CD11b (V) and FSC (VI) with blue colors indicating a node with low expression and red colors indicating a node with high expression of the respective marker.

We then took a closer look at the heterogeneity of neutrophils in the tissue by analysing the pseudotime dendrograms generated by a SPADE analysis of CD11b+Ly6G+ neutrophils. To interpret and annotate the SPADE trees shown in Fig. 3, we created several versions of each tree, coloured according to the median intensity of each measured marker (Fig. 5A-D). These coloured trees were then used to identify the subpopulation of neutrophils represented on the different parts of the tree. This method has been shown to identify cell populations that are mischaracterized in

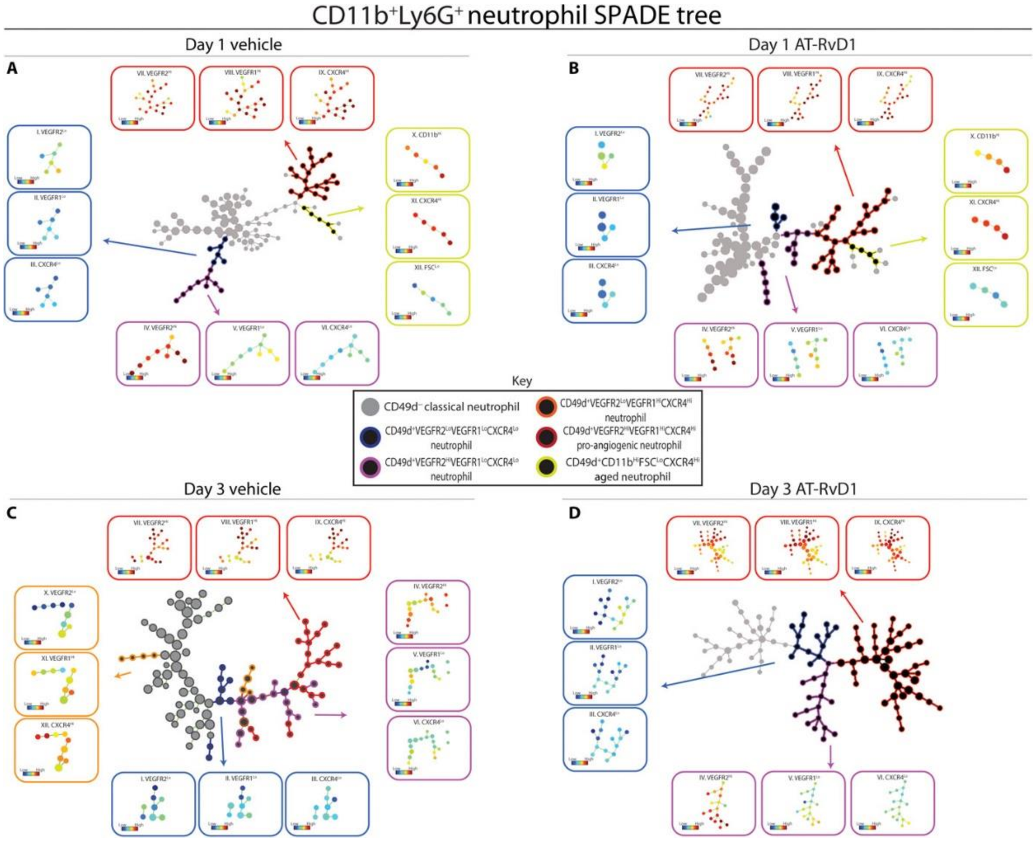

Figure 6. Analysis of neutrophil pseudotime trajectories using SPADE culminates in a unique marker expression profile of a putative pro-angiogenic subpopulation.
Pseudotime analysis generated SPADE trees consisting of CD11b+Ly6G+ neutrophils from tissue at day 1 after surgery with vehicle control (A), day 1 after surgery with sustained AT-RvD1 treatment (B), day 3 after surgery with a vehicle control (C), and day 3 after surgery with sustained AT-RvD1 treatment (D). Pseudotime trajectories show that distinct neutrophil phenotypes emerge. Day 1 after surgery shows the presence of an aged neutrophil phenotype (A and B). At day 3, the aged neutrophil subpopulation is not present, but the accumulation of pro-angiogenic neutrophils is notable in response to AT-RvD1 (D). Gray nodes are CD49d− classical neutrophils, and black nodes are CD49d+ with color strokes separating these cells into separate neutrophil phenotypes based on functional markers. The expression level, in the form of a heatmap overlay onto the nodes, of these functional markers for every subpopulation is displayed as a call-out box. Each SPADE tree was constructed with pooled data of n = 4.

manual gating strategies (18). We used selected angiogenic markers—VEGFR1, VEGFR2, and CXCR4—and integrin markers—CD11b and CD49d—to assign phenotype definitions to the SPADE dendrogram trajectories. At day 1, we identified a pro-angiogenic neutrophil subset (red stroke) expressing high levels of CD49d, VEGFR1, VEGFR2, and CXCR4 and an aged neutrophil subset (yellow stroke) with a small size and expressing high levels of CD49d, CD11b, and CXCR4 (Fig. 6A and B). At day 3, the aged neutrophil subset is not present in the neutrophil population, but the pro-angiogenic subset persists (Fig. 6C and D). We identify transitioning/intermediate neutrophil subsets (blue, purple, and orange strokes) within the CD49d+ population that lack the expression of one or more of the angiogenic markers (Fig. 6I to VI). The relative marker expressions of each node on the SPADE tree can also be visualized on the corresponding heatmap showing every node's unique surface marker expression level above or below the means of the population (Fig. 7A-D). This validates the phenotypes assigned to the SPADE tree as being unique subsets. The ability to separate the transitioning phenotypes from the pro-angiogenic population allows a more specific insight into the effects of AT-RvD1 on the neutrophil population.

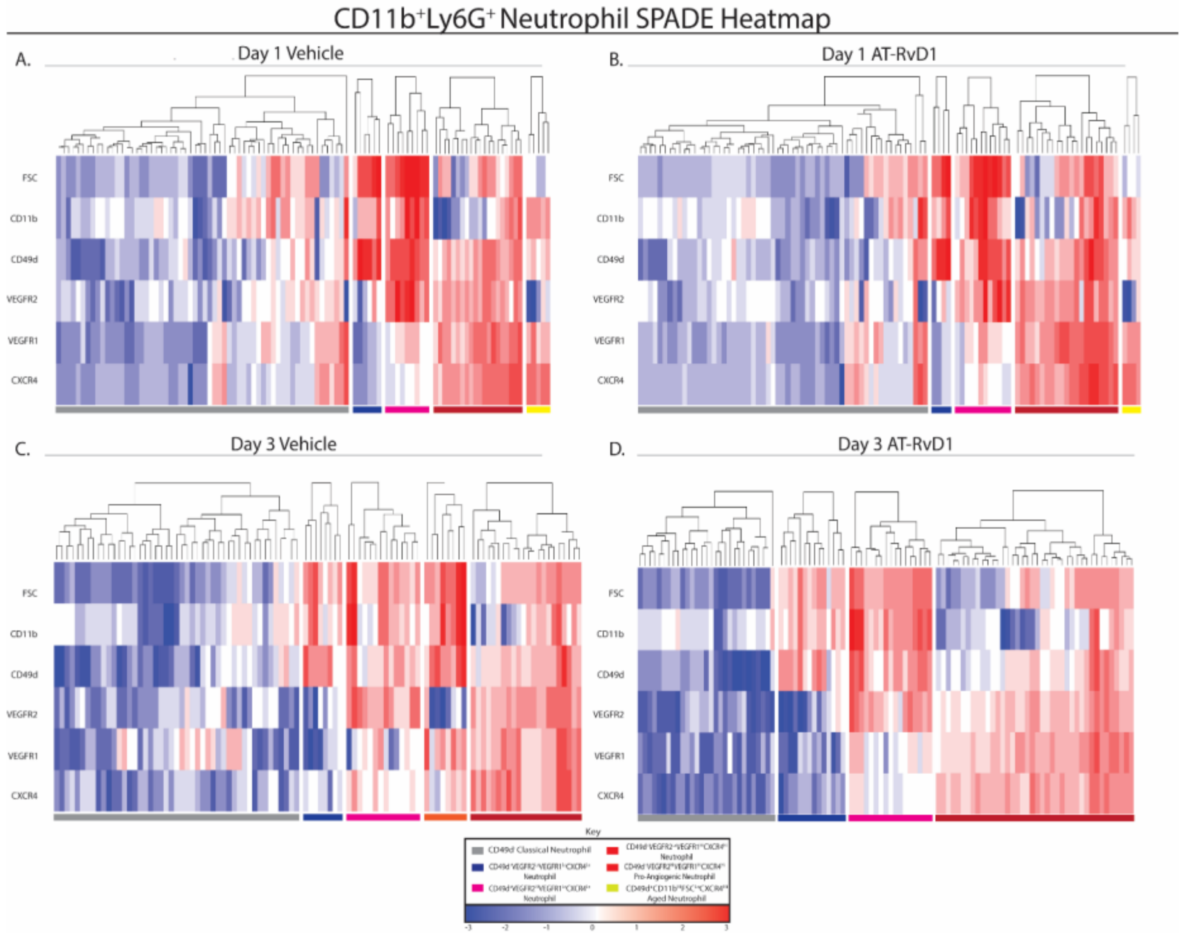

Figure 7. Marker expression heatmap of SPADE nodes reveals subtle neutrophil heterogeneity.

Every node of the SPADE tree has a distinct surface marker fingerprint that can be shown using a heatmap. Heatmap showing marker expression (rows) in every node (column) of the day 1 vehicle control (A), day 1 AT-RvD1 treated (B), day 3 vehicle control (C) and day 3 AT-RvD1 treated (D) Ly6G+ SPADE dendrograms shown in Fig.3. The colors along the bottom of each heatmap correspond to the neutrophil phenotypes identified using the corresponding SPADE tree. The marker expression shown is reported using a z-score calculated using the mean and standard deviation of every marker expression where the population is CD11b+Ly6G+ Neutrophils. Blue shows an expression level below the mean of the population and red shows an expression level above the mean of the population.

3.2.2 Local, biomaterial-mediated AT-RvD1 delivery modulates the heterogenous neutrophil response to injury.

To assess the effect sustained AT-RvD1 has on the different neutrophil populations in an inflammatory environment, we quantified the cell frequency of each SPADE-identified neutrophil subset (Fig. 8). At 3 days after injury, there is an increase in nonclassical CD49d$^+$ neutrophils in the local tissue environment in response to sustained AT-RvD1 treatment (Fig. 8A). The driving force behind this increase in CD49d$^+$ neutrophils is a targeted increase in pro-angiogenic

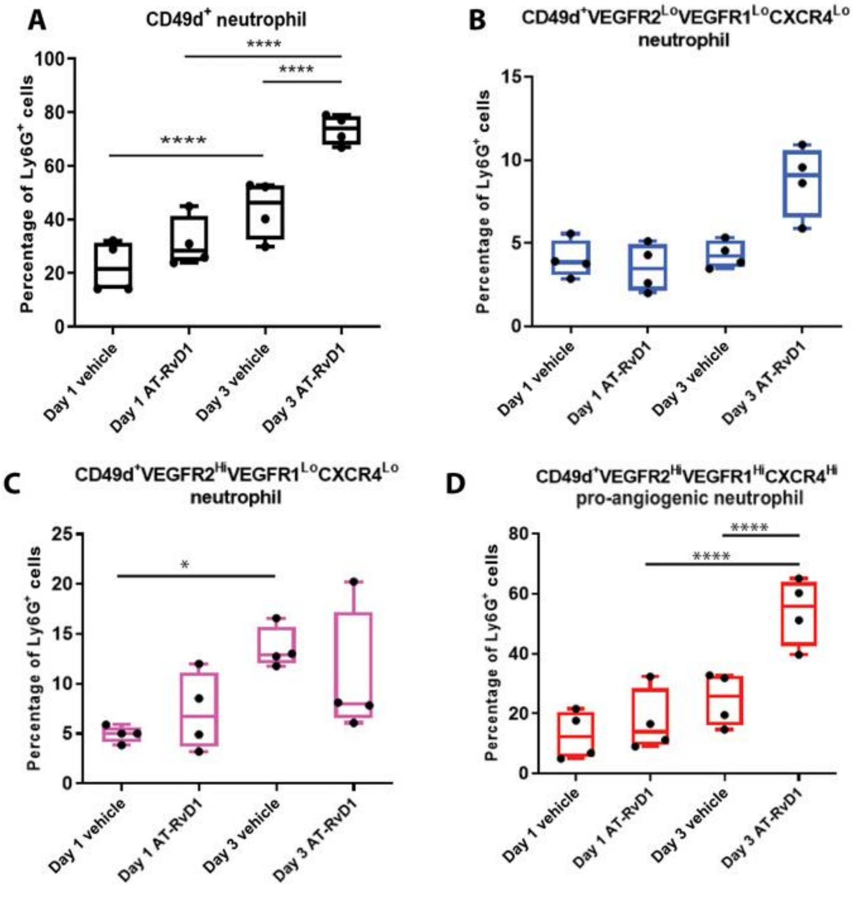

Figure 8. AT-RvD1 treatment selectively increases the frequency of pro-angiogenic neutrophils.

Frequency of the neutrophil populations identified using SPADE as a percentage of all CD11b$^+$Ly6g$^+$ neutrophils (A-D) show the driving force for an increase in frequency of CD49d$^+$ neutrophils due to AT-RvD1 treatment is specifically the pro-angiogenic population (E and F). Statistical analyses were performed using a one-way analysis of variance (ANOVA) with Tukey's multiple comparisons; *$P < 0.05$ and ****$P < 0.0001$; $n = 4$ animals per group.

neutrophils, as that is the only subset affected by AT-RvD1 delivery (Fig. 8B-D). We explored this targeted effect further by constructing days 1 and 3 tornado plots (Fig. 9). To do so, we generated a day 1 and day 3 SPADE tree that includes both cells from AT-RvD1–treated and vehicle control dorsal tissue (Fig. 9 A and B). The difference of the frequency of cells from the

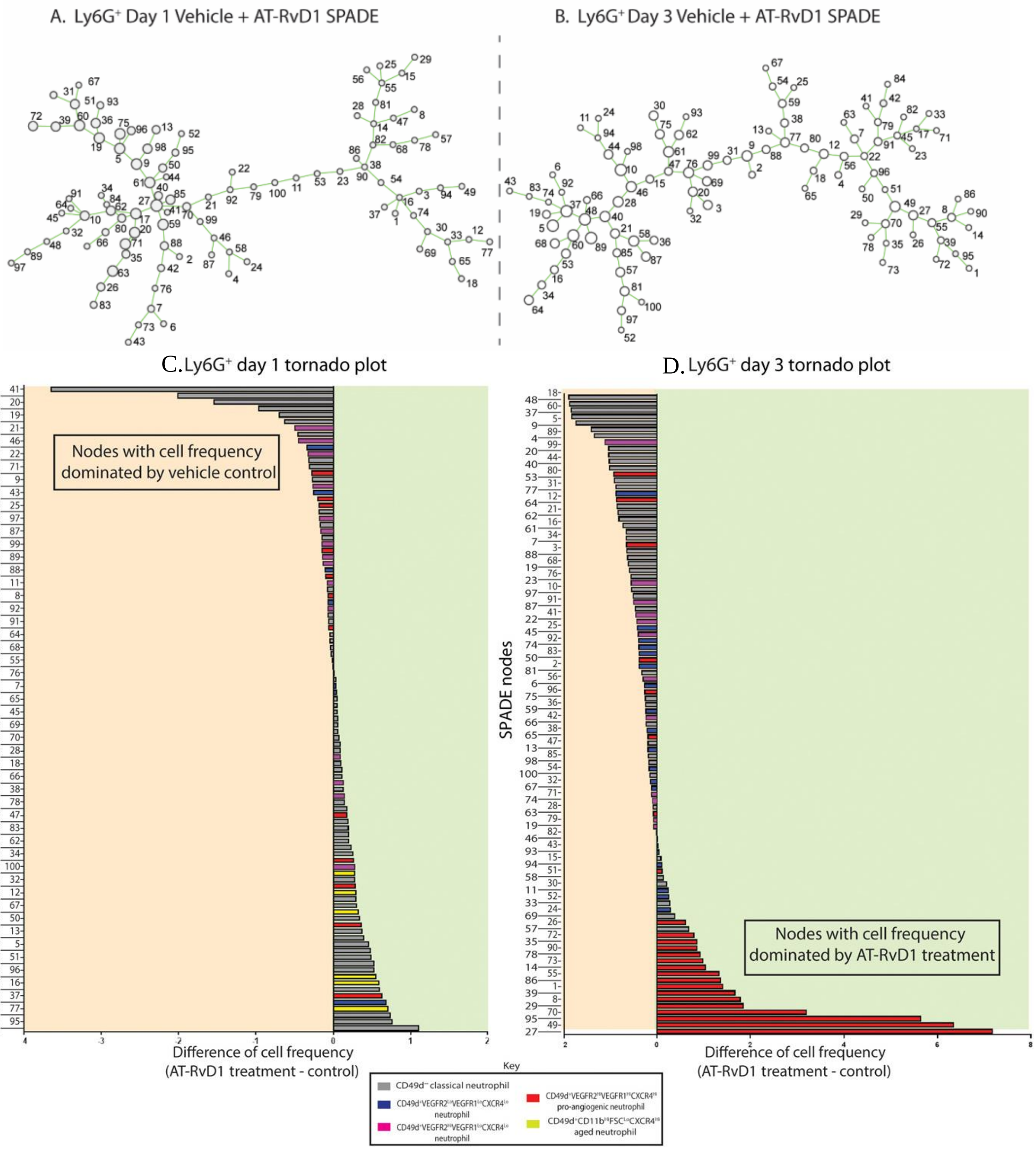

Figure 9. Day 1 and day 3 SPADE tornado plot analysis.
Day 1 (A) and day 3 (B) SPADE dendrograms containing both vehicle control and AT-RvD1–treated CD11b$^+$Ly6G$^+$ neutrophils. Every node on the SPADE tree is assigned a neutrophil phenotype and then whether the cells in that node are dominated by those that come from a treated sample or not are visualized in a tornado plot. The corresponding tornado plots for day 1 and day 3 are shown in (C) and (D), respectively. A difference (AT-RvD1 treated to vehicle control) under 0 reflects a decrease in that particular cell phenotype number with AT-RvD1 treatment, whereas a positive difference suggests that there is an increase in cell number with AT-RvD1 treatment.

treated tissue and the frequency of cells from the control tissue is calculated for each node. The greater the number resulting from this calculation, the more dominated the node is by cells from the AT-RvD1–treated tissue. The nodes are assigned a phenotype according to their expression of angiogenic and integrin surface markers and the corresponding bar on the tornado plot is colored according to the phenotype. At day 1, there is no specific neutrophil phenotype that is dominated by treatment; however, at day 3, the pro-angiogenic neutrophil nodes are dominated by AT-RvD1 treatment (Fig. 9 C and D). In addition, at day 3, 20 of the 30 nodes found to be dominated by cells from AT-RvD1–treated tissue are a pro-angiogenic neutrophil cluster of cells (Fig. 9D). Thus, the pseudotime analysis of neutrophils using SPADE reveals a selective increase in pro-angiogenic neutrophils due to AT-RvD1–sustained release.

Pro-angiogenic neutrophils have been implicated in playing a role in local vessel remodeling during inflammation [64, 81]. Therefore, we sought to validate our finding from the SPADE analysis that AT-RvD1 results in an accumulation of pro-angiogenic neutrophils and gain further insights on the functional effects of AT-RvD1. We rendered the whole mount confocal images into surfaces using Imaris (Fig. 10A). This allows us to count the number of $Ly6g^+$ neutrophils along with the number of $Ly6g^+$ neutrophils also expressing CD49d while calculating the distance of these cells to the surrounding vessels. In line with the SPADE analysis showing an increase in $CD49d^+$ neutrophils due to AT-RvD1 treatment, using immunohistochemistry, we see a significant increase in these cells due to AT-RvD1 treatment (Fig. 10B and D). In addition to a higher number of the $CD49d^+$ neutrophils, this analysis reveals that

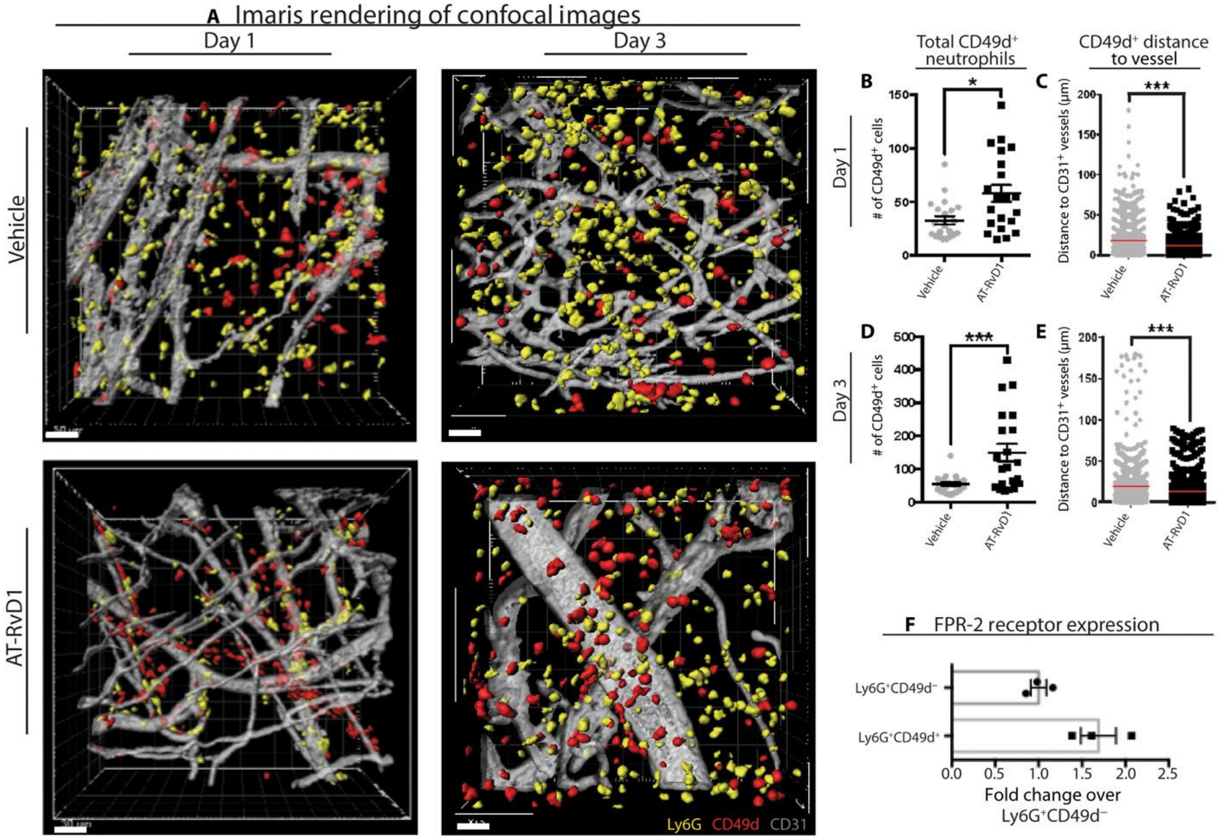

Figure 10. Recruitment and infiltration of CD49d$^+$ neutrophils into the dorsal tissue. CD49d was the marker chosen to extrapolate pro-angiogenic neutrophil functionality in response to AT-RvD1 released from PLGA thin films. (**A**) Imaris renderings from the confocal images of neutrophil infiltration into tissue at day 1 and day 3. (**B** to **E**) Quantification of Imaris renderings for total CD49d$^+$ neutrophils and distance to CD31$^+$ vessel at days 1 and 3. (**F**) Quantification of FPR-2 receptor expression on CD49d$^-$ and CD49d$^+$ neutrophils. Statistical analyses were conducted using two-tailed Mann-Whitney test and two-tailed *t* test; $^*P < 0.05$ and $^{***}P < 0.001$; $n > 100$ cells, across three to four animals per group. Scale bars, 30 μm for Imaris.

this subset of neutrophils specifically localizes closer to vessels when treated with AT-RvD1 compared with a vehicle control (Fig. 10C and E). The finding that AT-RvD1 has targeted, direct effects on this pro-angiogenic subset of neutrophils is supported by the higher expression of its receptor—FPR-2 (formyl peptide receptor 2)—on CD49d$^+$ neutrophils compared with CD49d$^-$ neutrophils (Fig. 10F).

3.2.3 Locally delivered AT-RvD1 enhances microvascular remodelling.

To assess the functional significance of the accumulation of pro-angiogenic neutrophils after AT-RvD1 treatment, we analyzed the vessel remodeling after injury through whole mount immunohistochemistry (Fig. 11A). Representative images of crops around the implant for different time points and treatments show that AT-RvD1 treatment has a vessel remodeling effect (Fig. 11B). We quantified the metrics of vessel remodeling by taking intravital bright-field images of the vascular bed at the time of surgery and 3 days after surgery (Fig. 11C - E). In accordance with qualitative observations in the confocal images (Fig. 11A and B), the quantitative vascular metrics show a significant increase in vessel tortuosity and arteriolar diameter because of AT-RvD1 treatment (Fig. 11D and E). We performed a multiplex cytokine analysis to further investigate possible pathways AT-RvD1 treatment could be activating en route to a pro-angiogenic outcome (Fig. 11F-I). At both day 1 and day 3, the AT-RvD1–treated and vehicle control samples separate along component 1 (Fig. 11F and H). Variable correlation plots show a sweep in the cytokines that strongly correlates these cytokines with the separation of the samples on component 1 (Fig. 11G and I). Furthermore, at both time points, VEGF, SDF-1α (stromal cell–derived factor 1α), and MCP-1 (monocyte chemoattractant protein-1) heavily contribute to principal component 1 and, thus, are key components contributing to the vascular remodeling observed with AT-RvD1 treatment (Fig. 11I).

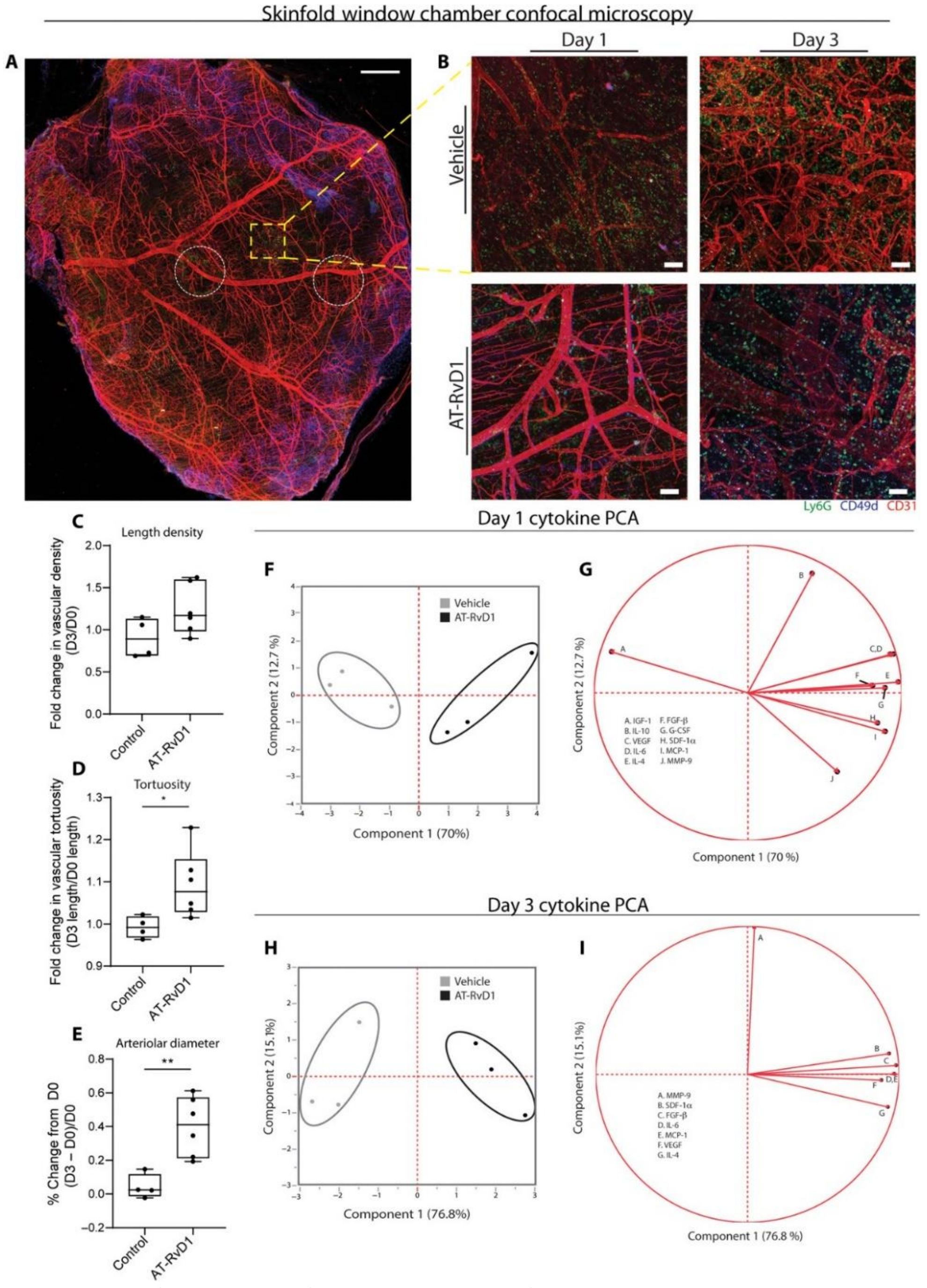

Figure 11 Delivery of AT-RvD1 from PLGA thin film promotes vascular remodeling. (**A**) Image (×10) of the whole mount dorsal skin tissue. CD49d was the marker chosen to extrapolate pro-angiogenic neutrophil functionality in response to AT-RvD1 treatment. (**B**) Representative confocal images of neutrophil infiltration and remodeling vasculature (white circles indicate biomaterial implantation location). (**E**) Quantification of the vascular metric length density (**C**), tortuosity (**D**), and arteriolar diameter. PCA (principal components analysis) on cytokine concentration at day 1 (**F** and **G**) and day 3 (**H** and **I**) after surgery. Statistical analyses were performed using two-tailed *t* tests; $*P < 0.05$ and $**P < 0.01$; $n = 4$ to 6 animals per group. Scale bars, 500 μm for 10× confocal

3.2.4 *AT-RvD1 delivery from PEG-4MAL hydrogels promotes a pro-regenerative shift in mononuclear phagocytes.*

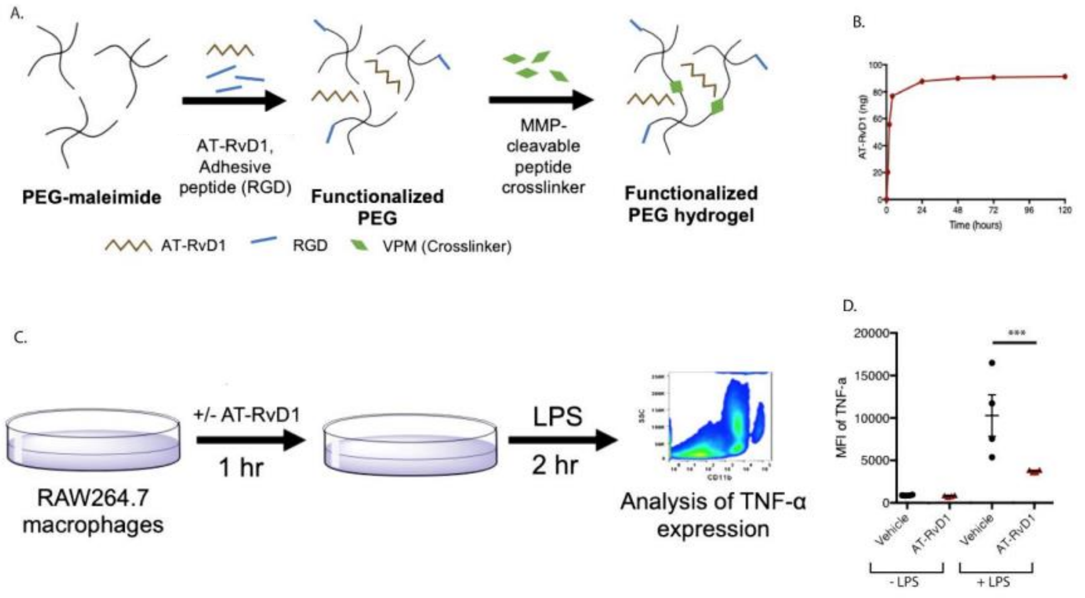

Figure 12. Hydrogel schematics, release profiles, and bioactivity.
Hydrogel fabrication method (A) HPLC measurements of AT-RvD1 release from PEG-MAL hydrogels (B). Bioactivity assay schematic (C). Bioactivity of AT-RvD1 (D). Statistical analysis was performed using one-way ANOVA with Tukey's post-hoc test, ***p

We developed PEG-4MAL hydrogels capable of locally delivering therapeutic and bioactive doses of AT-RvD1 in the first 24 hours (Fig. 12). These designed PEG-4MAL hydrogels incorporate the RGD adhesive peptide in order to facilitate cell infiltration into the hydrogel and thus foster cellular interactions. RGD (Fig. 13B) or RDG (inactive scrambled peptide) (Fig. 13C) functionalized PEG gels were implanted on the exposed dermal layer of the dorsal skinfold of mice that express GFP under the CX3CR1 promoter (CX3CR1$^{GFP/+}$) on day 1 after injury (Fig. 13A). At day 3, we performed intravital laser scanning confocal microscopy and acquired 25-30-

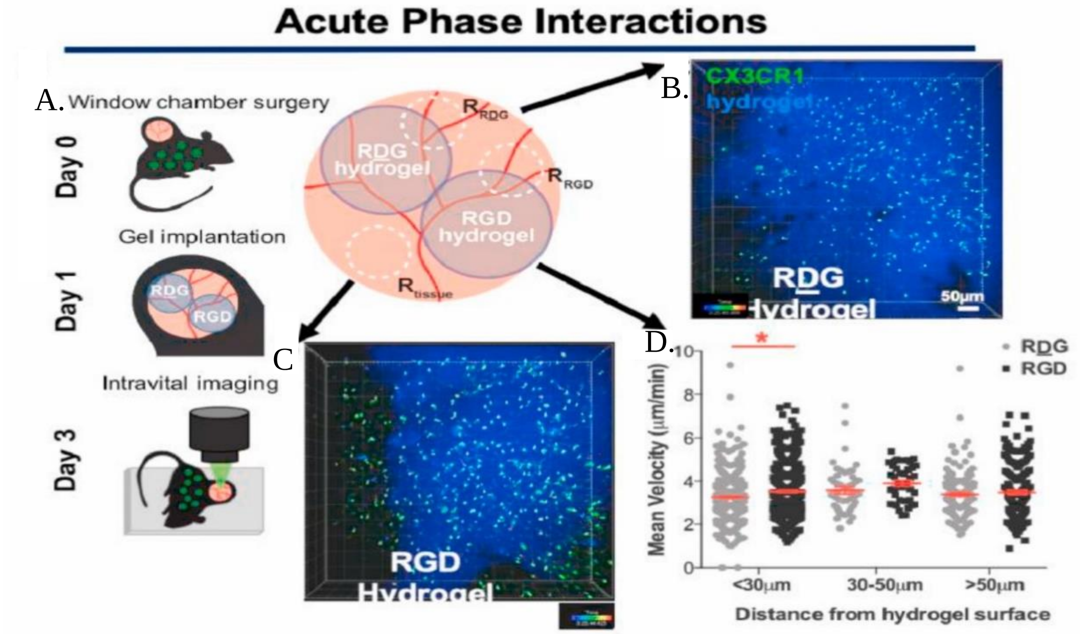

Figure 13. Protease-degradable PEG hydrogels functionalized with RGD recruit immune cells.

(A) Dorsal skinfold window chambers were performed in in CX3CR1$^{gfp/+}$ mice. One RDG- (B) and one RGD-functionalized (C) hydrogel were placed on the exposed layer at day 1. At day 3, intravital confocal microscopy was performed. Z-stacks were acquired in each region. CX3CR1+ cells are shown in green, fluorescently tagged hydrogel is shown in blue. Scale bar, 100 μm. (D) Mean velocity of CX3CR1+ cells, classified by their minimum distance from the hydrogel surface. $*p < 0.05$ compared to RDG hydrogel by Kruskal-Wallis. n = 3 mice.

min videos to visualize cells interacting with the hydrogel implants. We tracked the mean and maximum velocity of CX3CR1+ cells around each hydrogel and found that the mean velocity was greater around RGD hydrogels compared to RDG hydrogels only if the cells were within 30 μm of the hydrogel surface (Fig. 13D). This indicates that on average, hydrogels functionalized with RGD, aid in cell adherence, therefore encouraging cell interactions within the hydrogel as compared to the control RDG-functionalized hydrogel.

Having established the targeted effects of AT-RvD1 released from a PLGA thin film biomaterial on pro-angiogenic neutrophils and the concomitant improvement of microvascular remodeling, we implanted our engineered hydrogel platform into the same dorsal skinfold window chamber model to validate our results. Our results show similar results to those reported earlier in this chapter. Specifically, local AT-RvD1 released from EG-4MAL hydrogels into the dorsal skinfold window chamber model significantly improved the vascular length density a day 7 post injury and the arteriolar diameter at both days 3 and 7 post injury (Fig. 14A-E). We used single-cell flow cytometry analysis to explore the effects of our pro-resolving hydrogel on infiltrating immune cells and their subsets (Fig. 14F-K). Similar to our previous analysis of the effect of local AT-RvD1 on neutrophils, we saw a significant reduction in the infiltration of pro-inflammatory neutrophils to the site of injury at days 1, 3 and 7 post injury (Fig. 14F). Furthermore, when exploring the effects of AT-RvD1 on mononuclear phagocytes, our results show a broad pro-regenerative shift with local AT-RvD1 characterized by a decrease in Ly6C^{High} monocytes and M1 macrophages along with an increase in Ly6C^{Low} monocytes, M2 macrophages and tolerogenic dendritic cells (Fig. 14G-K). These results are important in showing that delivering AT-RvD1 from PEG-4MAL hydrogels is still able to shift the cellular milieu away from persistent inflammation and towards resolution and wound healing.

We used a genetically identical donor-to-host tail skin tissue graft model to establish the rigor of our approach and assess whether the pro-regenerative, AT-RvD1–mediated shift in the infiltrating immune cell population is able to improve wound healing and transplant tolerance. We leveraged these PEG-4MAL hydrogels capable of locally delivering therapeutic doses of AT-RvD1 in the first 24 hours (Fig 12) and injected the hydrogel into the wound immediately after skin transplantation. We collected tissue samples at 3, 7, and 14 days after injury from both vehicle control and AT-RvD1–treated groups for single-cell analysis. Using manual gating techniques, we selected CD11b^{+}CD64^{+}Mertk^{+} macrophages to analyze using SPADE. We pooled all the tissue samples (across all days and treatments) and constructed a macrophage-specific SPADE dendrogram. Using SPADE, we are able to identify a CD206^{lo}Ly6C^{hi} M1 macrophage group, a

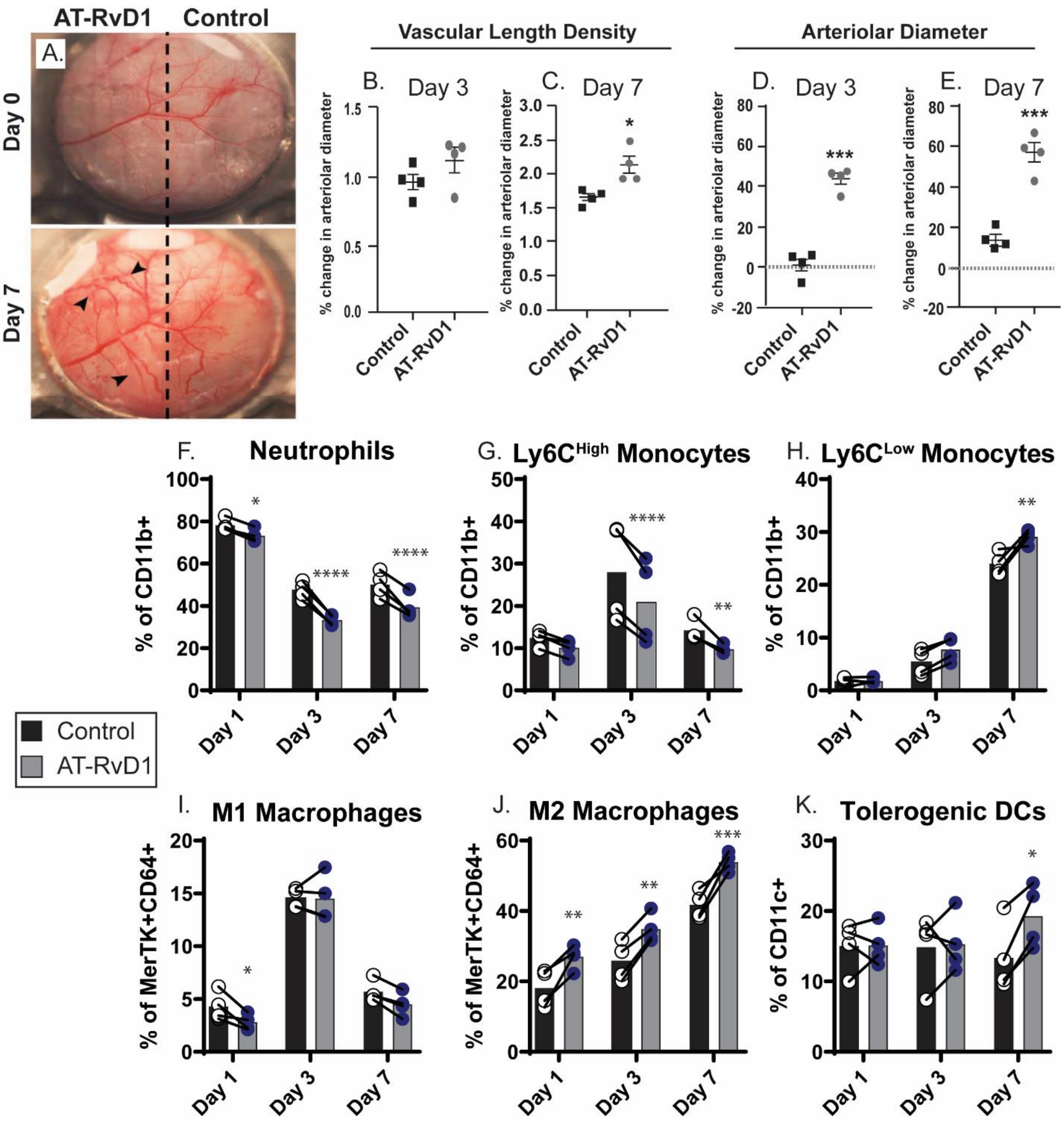

Figure 14. AT-RvD1 released from PEG-MAL hydrogels improves microvasculature remodeling via pro-regenerative immune cell polarization.

(A) Representative brightfield images of the dorsal skinfold window chamber depicting the internal control strategy. Arrows indicated new vessel branches near the AT-RvD1 hydrogel implantation site. Quantification of the vascular length density (B and C) and arteriolar diameter (D and E) at days 3 and 7 post injury showing improved microvasculature remodeling with AT-RvD1 hydrogel. Quantification of different pro-inflammatory and pro-regenerative immune cell subsets (F-K) exhibiting a reduction in pro-inflammatory and accumulation of pro-regenerative cell subsets. (B-E) Statistical analyses were performed using two-tailed t-tests (F-K) Statistical analyses were performed using a two-way analysis of variance (ANOVA) with Sidak's multiple comparisons and the Geisser-Greenhouse correction to account for the differences in variability amongst groups; *P < 0.05, **P < 0.01, ***P<0.001, ****P<0.0001

CD206^{hi}Ly6c^{lo} M2 macrophage group, and a CD206^{hi}Ly6c^{hi} M1/M2 hybrid macrophage group (Fig. 15A). With this SPADE dendrogram, we are able to isolate specific tissue samples and identify how AT-RvD1 treatment shifts the frequency of macrophages over time (Fig. 15B - G). At day 3, both vehicle control and AT-RvD1–treated macrophage populations show a similar composition of macrophage subpopulations (Fig. 15B and C). However, from day 3 to day 7, we see that while in the vehicle control case, the macrophages shift further toward an M1 phenotype, and in the AT-RvD1 treatment case, the macrophages shift toward an M2 phenotype (Fig. 15D and E). This shift continues from day 7 to day 14 as the vehicle control macrophages settle into the profibrotic hybrid phenotype, while the AT-RvD1–treated macrophages have a predominant M2 phenotype (Fig. 15F and G). By quantifying these shifts in the macrophage population visualized in SPADE, we confirm that there is a decrease in M1 macrophages at day 7 and an increase in M2 macrophages at day 14 with AT-RvD1 treatment (Fig. 15H - J).

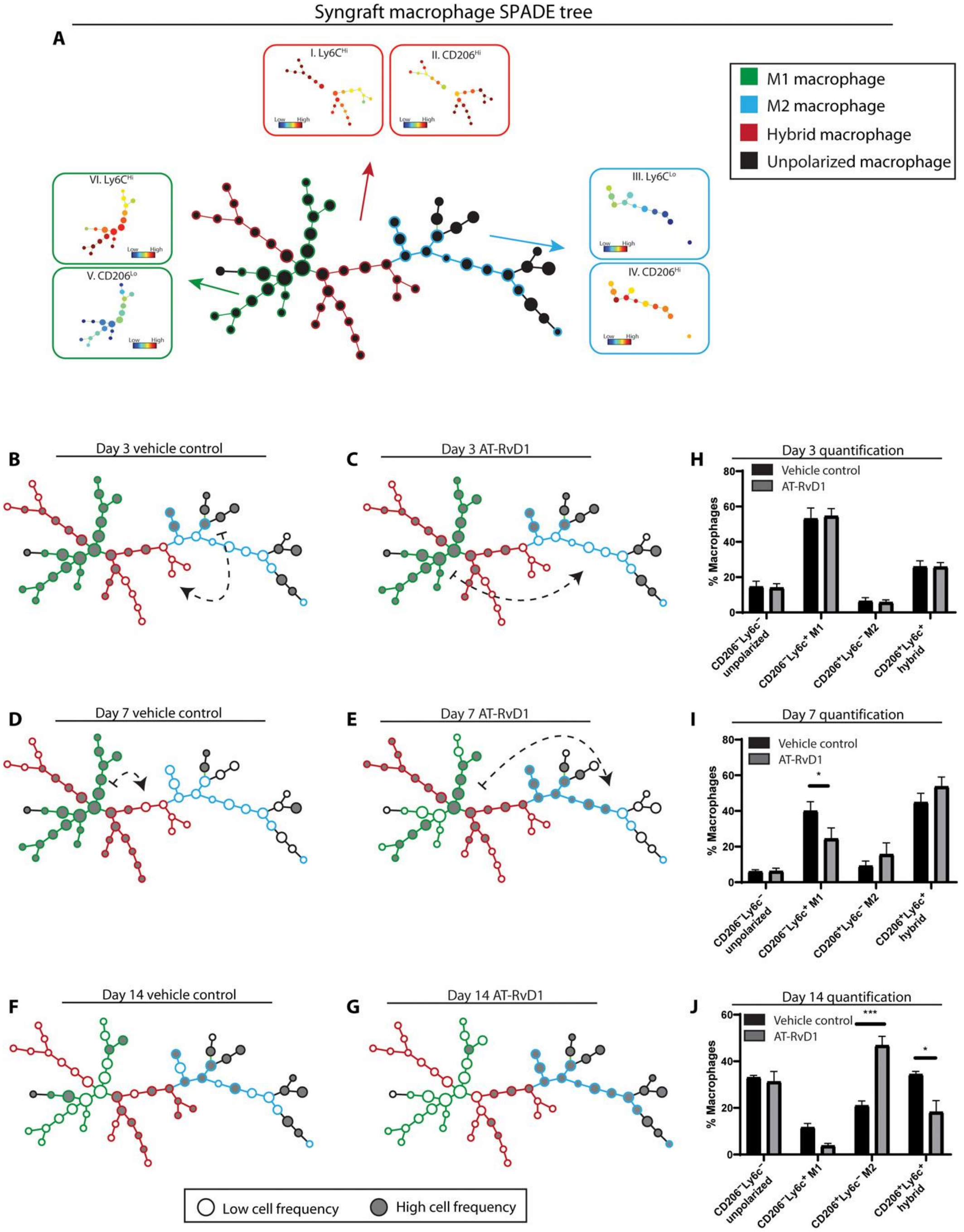

Figure 15 AT-RvD1 promotes a pro-regenerative shift of the macrophage population.
(A) CD64$^+$MERTK$^+$ macrophages pooled from all samples from both treatments and three time points (days 3, 7, and 14) were used to construct a SPADE dendrogram. The red annotation corresponds to a hybrid phenotype with high expression of both Ly6C and CD206 (I and II), the blue annotation corresponds to an M2 phenotype with low expression of Ly6C and high expression of CD206 (III and IV), and the green annotation corresponds to an M1 phenotype with high expression of Ly6C and low expression of CD206 (V and VI). (B to G) cells are highly populated (gray nodes) and they are less densely populated (white nodes). The movement of these cells across time is depicted with dashed arrows that show where the cells are visualized to move (B to E). (H to J) The visualization method shows an AT-RvD1–mediated shift in cell frequency toward an M2 phenotype that can also be seen in the corresponding quantifications. Statistical analyses were performed using a two-way ANOVA with Tukey's multiple comparisons; $^{*}P < 0.05$ and $^{***}P < 0.001$; $n = 4$.

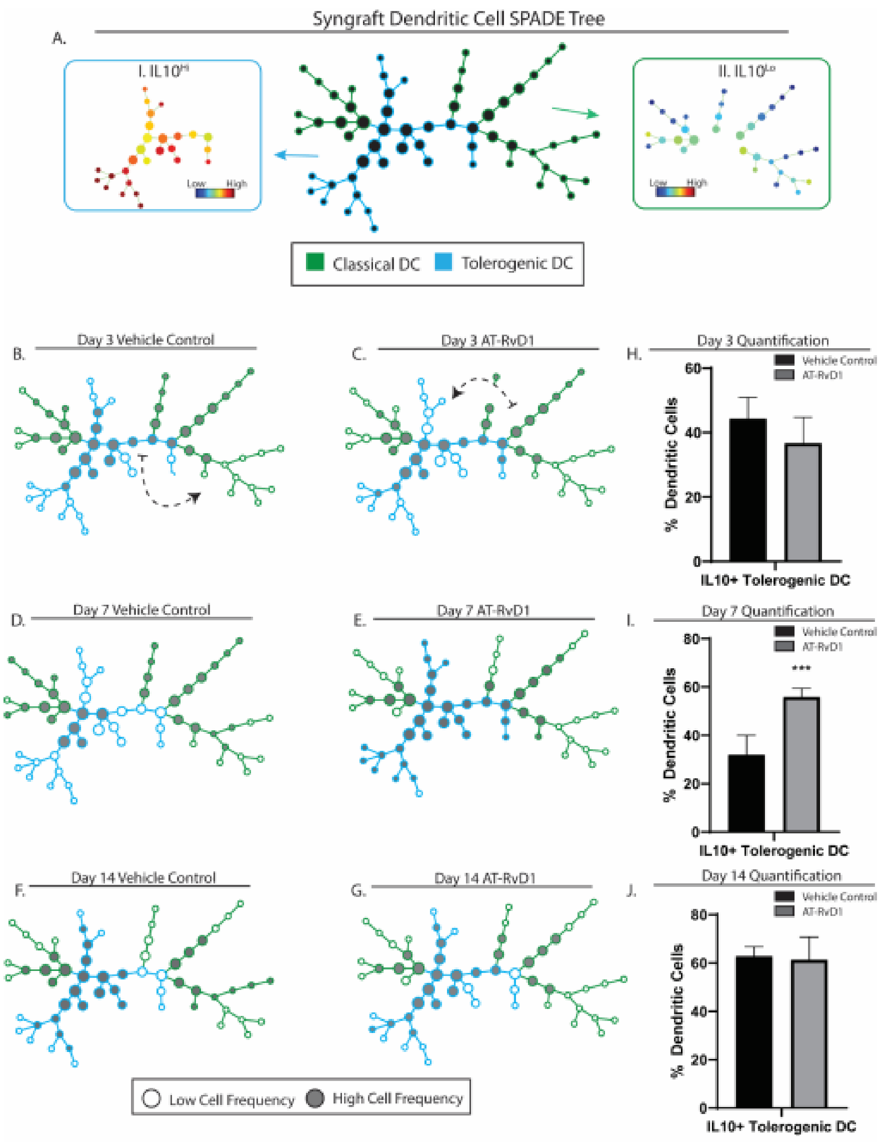

Figure 16. AT-RvD1 promotes a pro-regenerative shift of the dendritic cell population. CD11c+ dendritic cells pooled from all samples from both treatments and three timepoints (day 3, 7, and 14) were used to construct a SPADE dendrogram (A). This SPADE dendrogram is annotated according to il10 surface marker expression. The blue annotation corresponds to a tolerogenic phenotype with high Il10 expression (I) and the green annotation corresponds to a classical phenotype with low il10 expression (II). Cells corresponding to a specific timepoint, and treatment combination are isolated and mapped out on the SPADE dendrogram to analyze where these cells are highly populated (grey nodes) and where they are less densely populated (white nodes) (B-G). The movement of these cells across time is depicted with dashed arrows that show where the cells are visualized to move (B and C). The visualization method shows an AT-RvD1 mediated shift in cell frequency towards a tolerogenic phenotype that can also be seen in the corresponding quantifications (H-J). Data presented as mean ± S.E.M. Statistical analyses were performed using two-tailed t-tests ***$p < 0.001$ n = 4 animals per group.

Using an identical approach, we manually selected CD11b$^+$CD11c$^+$ dendritic cells to analyze using SPADE. We pooled all the tissue samples (across all days and treatments) and constructed a dendritic cell–specific SPADE dendrogram. Using SPADE, we are able to identify a $IL10^{hi}$ tolerogenic dendritic cell group and a $IL10^{lo}$ classical dendritic cell group (Fig. 16A). With this SPADE dendrogram, we are able to isolate specific tissue samples and identify how AT-RvD1 treatment shifts the frequency of dendritic cells over time (Fig. 16B-G). From day 3 to day 7, we see a shift in dendritic cells toward an $IL10^{hi}$ phenotype with the AT-RvD1 treatment but see an opposite shift in the vehicle control case (Fig. 16B-E). By quantifying this shift in the dendritic cell population visualized in SPADE, we confirm that there is an increase in $IL10^{hi}$ tolerogenic dendritic cells at day 7 with AT-RvD1 treatment. Combined, these results establish the utility of SPADE and indicate that there is a lasting pro-regenerative effect on macrophages and dendritic cells after AT-RvD1 treatment.

To further demonstrate the effectiveness of biomaterial-mediated AT-RvD1 treatment as a regenerative immunotherapy, we performed a multiplex cytokine analysis and investigated the wound healing and integration of skin tissue grafts using macroscopic gross images of the grafted syngraft over time. As expected, both control and AT-RvD1 groups show no signs of transplant rejection. However, at day 10, the AT-RvD1 hydrogel treatment group appears to be closer to full wound closure than the vehicle control (Fig 17G). After the principal components analysis of the multiplex cytokine panel, at days 3, 7, and 10, AT-RvD1–treated and vehicle control samples separate along component 1 (Fig 17A, C and E). Similar to the cytokine analysis performed in the dorsal skinfold window chamber model (Fig. 11), VEGF and SDF-1α heavily contribute to the separation (Fig. 17B, D and F). These cytokines also have a significantly higher concentration with AT-RvD1 treatment compared with control (Fig 18E and P).

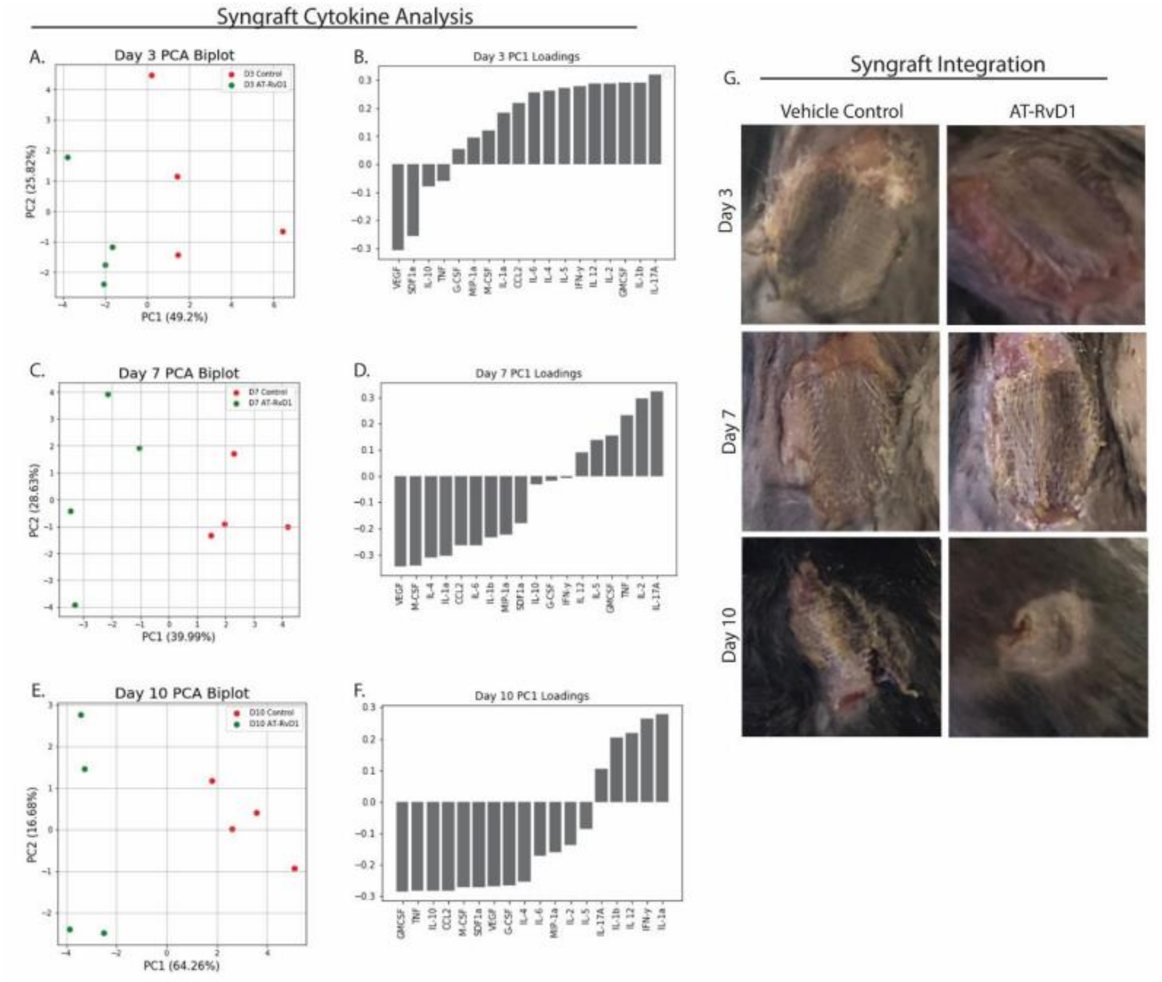

Figure 17. Multiplex cytokine analysis and macroscopic image analysis of AT-RvD1 treatment compared to vehicle control.
Principal components analysis was performed at days 3, 7 and 10 on a multiplex cytokine panel (A-F). At all three timepoints AT-RvD1 treated samples are shown to separate along component 1 (A, C and E). The loadings plots shows the cytokines that contribute the most to this separation (B, D and F). Macroscopic images of graft integration show increased wound closure with AT-RvD1 treatment.

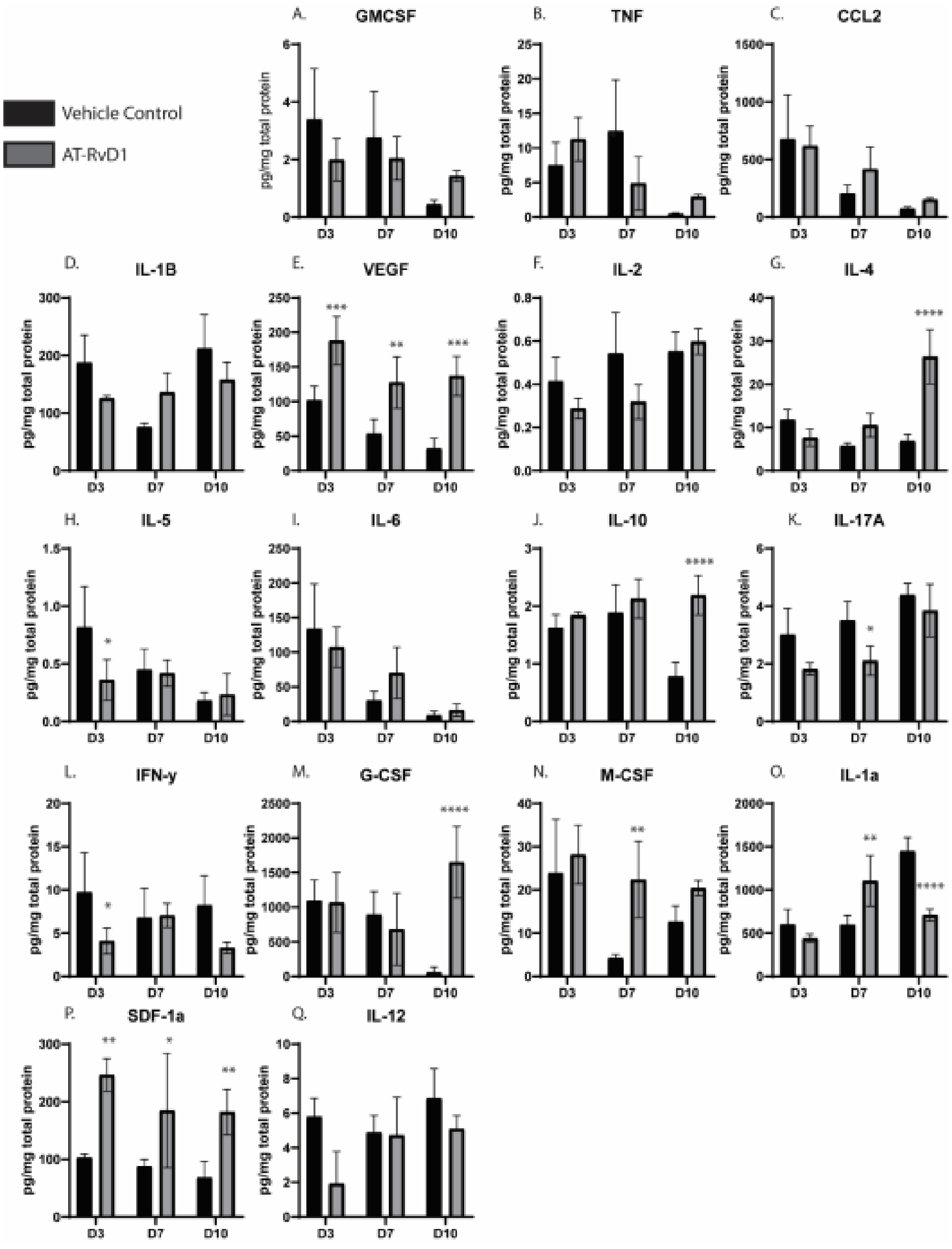

Figure 18. AT-RvD1 increases concentration of anti-inflammatory cytokines in the peri-implant environment.

A comparison of various cytokine levels between AT-RvD1 treatment and vehicle control at days 3, 7 and 10 (A-Q). Data presented as mean ± S.E.M. Statistical analysis were preformed using two-way ANOVA with Tukey’s post-hoc test $*p < 0.05$. n = 4 animals per group.

3.3 Discussion

The immune system is able to achieve a wide range of responses in health and disease due to the variety and heterogeneity of specialized immune cells. However, classical analytical techniques greatly underestimate the functional diversity of the immune system by providing an imperfect systems-level view of bulk immune cell populations. This is a major hurdle in the regenerative medicine field, where there is an increasing focus on the recruitment or polarization of specific immune cell subsets toward a therapeutic outcome [82-84]. Recently, new analytical and visualization techniques have been developed that allow scientists to gain new insights into immune system diversity [85]. As these techniques are applied in the field of regenerative medicine, significant mechanistic discoveries can be made that aid in developing the most effective therapeutic strategies. However, there are complex environmental cues and timing factors that contribute to high cell-to-cell variation in the expression of surface markers, which presents a unique challenge. Such high variation complicates the analysis of these experiments since a population of cells captured at the same time includes many distinct intermediate differentiation states, and considering only their average properties masks trends occurring across individual cells [86, 87]. We overcome this challenge using SPADE, a dimensionality reduction and pseudotime analysis technique that allows us to explore neutrophil heterogeneity in response to a chronic inflammatory environment in an in vivo dorsal skin wound model and explore macrophage and dendritic cell response in a skin transplant model to the sustained delivery of AT-RvD1, a proresolving lipid mediator.

Neutrophils, until recently, were considered to be a relatively homogeneous cell population with a set of conserved functions—phagocytosis, degranulation, and release of nuclear material. However, current research in the field of neutrophil biology has revealed that neutrophils have a much more diverse repertoire of functional responses [88]. This emergence of functional neutrophil phenotypes opens up the possibility to harness the therapeutic potential of neutrophil subsets. Using UMAP and SPADE to investigate neutrophil heterogeneity, we found that in the presence of an inflammatory injury, there is a much larger degree of neutrophil heterogeneity in the injured tissue than in circulation. This result speaks to the long-standing question of whether defined phenotypes are programmed in the bone marrow or whether mature neutrophils in circulation can be reprogrammed by local external stimuli [64]. Thus, our results show that the local inflammatory microenvironment provides cues that induce the neutrophils to acquire specialized functions, which is depicted as different subpopulations spread across distinct islands on the UMAP and among different trajectories and nodes on the SPADE dendrograms. We locally deliver AT-RvD1 into this microenvironment to skew this neutrophil reprogramming to a more pro-regenerative state. More specifically, because we and others have shown the pro-angiogenic effects of AT-RvD1, we sought to use AT-RvD1 to locally induce the pro-angiogenic polarization of neutrophils [72].

Pro-angiogenic neutrophils are a distinct neutrophil subset recently found to display tropism for angiogenic foci and contribute to rapid and early vascular growth [71]. Impaired tissue vascularization is associated with chronic inflammation, and early angiogenesis helps restore appropriate tissue structure and function. Resolvins, a class of specialized pro-resolving lipid mediators, have been extensively characterized in their ability to inhibit neutrophil infiltration and promote their timely apoptosis [34]. However, the use of such lipid signalling pathways to target specific neutrophil subsets for regenerative immunotherapy has yet to be explored. We use SPADE to track the tissue neutrophil lineage in pseudotime, which allows us to look at the progression of pro-angiogenic marker expressions that results in transitioning neutrophil subsets that culminate in a pro-angiogenic neutrophil subpopulation. With this, we are able to analyse the effects that sustained AT-RvD1 delivery on each subpopulation. We found that by day 3 after AT-RvD1 delivery, there is an overwhelming increase in the pro-angiogenic subset of neutrophils, while there is no effect on the transitioning nonclassical neutrophils identified. SPADE identifies a separate trajectory for aged neutrophils at day 1 that is not present at day 3 after injury. This could be explained by the idea that some neutrophil subtypes may derive from aging neutrophils migrating into tissues given their activated and highly reactive state [89]. The specific accumulation of pro-angiogenic neutrophils is a novel mechanism of action for this pro-resolving lipid mediator and is the first small-molecule approach that is able to selectively target a therapeutically functional neutrophil subpopulation. Our results suggest that the local delivery of AT-RvD1 results in the local reprogramming of neutrophils that have migrated into the tissue; however, the mechanism behind this reprogramming by an alteration of lipid signalling pathways requires further studies.

Furthermore, using whole mount immunohistochemistry of the injured dorsal skin tissue, we see an increase in Ly6G+CD49d+ cells. We are able to use this simplified marker staining to imply the function and behavior of the pro-angiogenic subset of neutrophils since we show in our previous results that the pro-angiogenic neutrophil subset is the overwhelming driving force behind any changes in this CD49d+ parent neutrophil population. Not only does this accumulation of Ly6G+CD49d+ cells validate our cytometry results, but it also allows us to gain unique insights into the functional changes that AT-RvD1 delivery is having on pro-angiogenic neutrophils. Our results show that these cells are positioned in closer proximity to the remodelling vasculature of the tissue in response to AT-RvD1. This accumulation and activation of pro-angiogenic neutrophils with sustained AT-RvD1 delivery coincide with an increase in arteriolar diameter and vessel tortuosity obtained from intravital bright-field imaging. Since the AT-RvD1 receptor FPR-2 is shown to be enriched on CD49d+ neutrophils, the delivery of this small molecule could be acting directly on this neutrophil subset. Linking the vessel remodelling that occurs with AT-RvD1 delivery directly to this neutrophil subset is still in need of further studies and is an exciting avenue for the field.

Evidence suggests that the early stages, right after the onset of inflammation, initiate an active, controlled process of inflammation resolution [57]. We use an AT-RvD1–loaded PEG-MAL hydrogel in a syngeneic skin graft model not only to further establish the rigor of our approach but also to show that modulating the early neutrophil response, as shown in the dorsal skinfold model, leads to a cascade of pro-regenerative immune cell accumulation. Specifically, our results show that sustained AT-RvD1 delivery in the first 24 hours after skin transplant is able to increase the accumulation of M2 macrophages and IL10+ tolerogenic dendritic cells at day 7 after transplantation. Recent studies have established a connection between neutrophil activity and macrophage or dendritic cell reprogramming [90, 91]. Thus, a strategy in which modulating the neutrophil response to injury leads to a pro-regenerative shift in downstream immune cell populations is an exciting avenue to explore. Whether AT-RvD1 delivery causes a change in the production of pro-resolving lipid mediators to have this downstream effect is also in need of further studies. Overall, the ability for AT-RvD1 delivered with a hydrogel to increase the wound closure after skin transplant further exhibits the therapeutic potential of this approach.

This study uses a novel method in which a nonlinear dimensionality reduction technique, UMAP, is used to visualize neutrophil heterogeneity on a two-dimensional map, and SPADE is used to make cellular hierarchy inferences among subpopulations of similar neutrophils. This method allowed us to uncover a previously unknown mechanism in which the sustained delivery of the pro-resolving lipid mediator AT-RvD1 leads to a targeted accumulation of pro-angiogenic neutrophils, increased early vessel remodelling, and enhanced wound closure after a skin transplant. Furthermore, as the targeting of key immune subsets becomes vital to regenerative immunotherapies, our studies can be used as a model to explore the subtle responses of different cellular populations to various therapeutic perturbations.

3.4 Conclusion

Taken together, our results demonstrate that localized delivery of AT-RvD1 allows for dual targeting of unique pro-resolving and pro-regenerative cell subsets involved in inflammation and wound healing. Specifically, modulation of initial neutrophil infiltration and subsequent polarization allows for reduced overall tissue damage and primes the tissue for early vascularization and regeneration. The local delivery of AT-RvD1 using PEG-4MAL hydrogels results in enhanced accumulation of pro-regenerative mononuclear phagocyte populations that further promote resolution and promote early wound healing. These results establish localized delivery of AT-RvD1 as a promising approach to promote resolution of inflammation in injury models with excessive and persistent inflammation towards the goal of functional tissue regeneration.

3.5 Materials and Methods

3.5.1 Fabrication of polymeric thin films

PLGA thin films were made, as previously described. Briefly, PLGA (50:50; DLG 5E, Evonik Industries) was solubilized in dichloromethane using a sonicator at 37°C until dissolved. Ten micrograms (100 µl) of AT-RvD1 (Cayman Chemical; solution in ethanol) was added to make

AT-RvD1–loaded films. Solutions were cast in Teflon molds and stored at −20°C until full organic solvent evaporation was observed. Films were then lyophilized for 24 hours. A 1-mm biopsy punch was used to produce films used in studies.

3.5.2 *Hydrogel fabrication*

Four-arm PEG (10-kDa molecular weight) end functionalized with maleimide (>95% purity; Laysan Bio) at 4.5% (w/v) was used for all hydrogel formulations. PEG macromers were functionalized with RGD peptide (GRGDSPC), cross-linked with the cysteine-flanked peptide VPM (GCRDVPMSMRGGDRCG) (AAPPTec) in 0.5 M MES buffer (pH 5.5). The final concentration of RGD (or RDG) was 1.0 mM. Gels were also loaded with AT-RvD1 (4 μg/ml) (Cayman Chemical). The cross-linker concentration was based on the concentration of nonreacted maleimide groups remaining on PEG macromers. For hydrogels used in animal studies, all components were filtered through a spin column after pH measurements and kept under sterile conditions until injection into the animals.

3.5.3 *Intravital confocal microscopy*

CX3CR1-GFP mice were anesthetized with vaporized isoflurane at 5% concentration for induction and maintained under anesthesia at 1–3%. The glass cover slip was removed, and sterile saline was administered to the exposed dorsal tissue to prevent desiccation. The anesthetized mouse was secured to the microscope stage in a custom adapter placed on top of a heating block to maintain body temperature. Intravital confocal microscopy was performed using a 20× water immersion objective (NA = 1.0) fixed to an inverter on a Zeiss LSM710 NLO microscope. Time-lapse z-stack images were acquired at each hydrogel edge. A step size of 5 μm was used in the z-direction.

Videos of 25–30 min were acquired at each location, with a time step of 30 s and a total of 2–3 videos acquired for each hydrogel, and one video acquired in distal tissue without a hydrogel.

3.5.4 Intravital imaging analysis

For 3D analysis in Imaris (Bitplane), time-lapse images were acquired adjacent to the implant to visualize immune cell distribution in the close surrounding tissue. Cells expressing CX3CR1-GFP were identified in Imaris using the surface tool. CX3CR1+ surfaces were identified by smoothing with a 2.77 µm grain size and a threshold value of 7.71 on absolute intensity. Touching objects were split using a seed points diameter of 10.4 µm with a quality threshold above 3.53. CX3CR1hi versus CX3CR1lo cells were discriminated by assigning half of all cells to each group based on maximum fluorescence intensity in the CX3CR1-GFP channel. The hydrogel surface was identified using the surface tool with a 10 µm grain size and a manually selected threshold value on absolute intensity. To calculate the distance between cells and the hydrogel surface, a distance transformation was applied to the hydrogel surface and the minimum distance of each cell was recorded. To track cell activity over time, cells were identified in Imaris using the spots tool. Estimated diameter was set to 8.00 µm with background subtraction enabled and an automatic threshold on quality. Tracks were selected for analysis if they lasted at least 300 s. Tracks were set to a maximum distance of 10.0 µm and a max gap size of 3 µm. Because statistical comparisons were made on a single-cell basis, an equal number of cells was used for analysis of each video. The minimum number of detected tracks was 73. Therefore, for videos with more than 73 tracks, we randomly selected 73 tracks for analysis.

3.5.5 Dorsal skin fold window chamber surgery

Animal experiments were performed using sterile techniques in accordance with an approved protocol from the Georgia Institute of Technology Institutional Animal Care and Use Committee. Male C57BL/6 mice (the Jackson laboratory) aged 6 to 12 weeks were anesthetized by inhaled isofluorane and surgically fitted with sterile dorsal skinfold window chambers (APJ Trading Co.), as previously described. Briefly, the dorsal skin was shaved, depiliated, and sterilized via three washes with 70% ethanol and chlorhexidine. The dorsal skin was drawn away from the back of the mouse, and one side of the titanium frame was attached to the underside of the skin. Sterile surgical microscissors were then used to expose the microvasculature through the removal of the epidermis and dermis in a 12-mm-diameter circle. Mice were implanted with two of the same films (either empty PLGA vehicle film or AT-RvD1–loaded PLGA film) placed on opposite sides of the window chamber. Before implantation, the films were washed in 70% ethanol for 30 s, followed by washing with sterile Ringer's solution for 30 s. Exposed tissue was then sealed with a sterile glass coverslip. Mice were administered with sustained-released buprenorphine intraperitoneally (0.1 to 0.2 mg/kg) and allowed to recover in heated cages. All mice received standard laboratory diet and water ad libitum throughout the course of the experiment.

3.5.6 Skin transplant graft experiment

Female C57BL/6 mice aged 5 to 7 weeks (Charles River) were transplanted with full-thickness tail skin grafts from age- and sex-matched Balb/c or C57BL/6 mice. Briefly, donor mice were euthanized under terminal anesthesia via cervical dislocation. Donors were placed tail first into a sterile decapicone with the tail exposed. The tail skin was sterilized via three washes with 70% ethanol and chlorhexidine. The tail skin was removed with surgical scissors and kept in ice-cold sterile saline until use. Recipient mice were anesthetized with 50 μl of ketamine-xylazine-saline cocktail (ratio of 5:1:4) and shaved and sterilized via three washes with 70% ethanol and chlorhexidine. A full-thickness defect was cut into the dorsal skin of the recipient mouse. Hydrogels were mixed and loaded into a syringe and injected in depots in the defect area. Skin grafts were cut from donor tails to fit into the defect area. Wounds were bandaged, and mice were administered with sustained-released buprenorphine intraperitoneally (0.1 to 0.2 mg/kg) and allowed to recover in heated cages. Bandages covering grafts were removed 7 days after graft placement. All mice received standard laboratory diet and water ad libitum throughout the course of the experiment.

3.5.7 Tissue harvest and flow cytometry

To collect samples for flow cytometry analysis, mice were euthanized via CO2 asphyxiation. The dorsal tissue was excised and digested with collagenase type 1A (1 mg/ml; Sigma-Aldrich) at 37°C for 30 min and further separated with a cell strainer to create a single-cell suspension. Single-cell suspensions were stained for flow cytometry analysis using standard methods and analyzed on a FACSAria III flow cytometer (BD Biosciences). Dead cells were identified using the Zombie Green fixable viability stain (BioLegend). The antibodies used for identifying neutrophils and neutrophil subsets were as follows: BV421-conjugated anti-CD11b (BioLegend), BV510-conjugated anti-Ly6C (BioLegend), APC-Cy7–conjugated anti-Ly6G (BioLegend), PE-conjugated anti-CD49d (BioLegend), PerCP-Cy5.5–conjugated anti-CXCR4 (BioLegend), APC-conjugated anti-VEGFR1 (BioLegend), and PE-Cy7–conjugated anti-VEGFR2 (BioLegend). Staining using BV (Brilliant Violet) dyes was performed in the presence of Brilliant Stain Buffer (BD Biosciences). Positivity was determined by gating on fluorescence minus one controls.

3.5.8 High-dimensional analysis of flow cytometry data

UMAP is a nonlinear dimensionality reduction algorithm. UMAP is able to embed high-dimensional data into a space of two or three dimensions. Cells are visualized in a scatter plot, where points that are closer together can be considered more similar. Before UMAP dimensional reduction, each flow cytometry sample was manually pregated to select live, single, CD11b+ myeloid cells. The gated FCS (fluorescence correlation spectroscopy) files were imported into Python 3.7 using fcsparser (https://github.com/eyurtsev/fcsparser) and Pandas 2.5. Each channel except for FSC (forward scatter) and SSC (side scatter) was normalized by applying arcsinh transformation with a cofactor of 150 to transform fluorescence data into a fold-channel scale. A composite UMAP plot that used data points from all samples (eight total samples: four vehicle and four AT-RvD1) was performed on MATLAB (https://github.com/lmcinnes/umap). Composite UMAPs were generated for day 1 and day 3. Each cell was then identified as a neutrophil by overlaying the manually pregated live, single-cell, CD11b+, Ly6G+ neutrophils onto the UMAP projection using MATLAB.

SPADE is a visualization tool that was designed to map heterogeneous single-cell populations into two dimensions on the basis of similarities across defined markers. SPADE creates a tree where nodes represent clusters of cells with similar marker expression. The size and color of each node are relative to the number of cells present and the median marker expression. SPADE was performed through MATLAB, and the source code is available at http://pengqiu.gatech.edu/software/SPADE/. SPADE automatically constructs the tree by performing density-dependent downsampling, agglomerative clustering, linking clusters with a minimum spanning-tree algorithm, and upsampling based on user input. The SPADE tree was generated by exporting uncompensated pregated live, single-cell, CD11b+ myeloid cells or pregated live, single-cell, CD11b+, Ly6G+ neutrophils. The markers used to build the SPADE tree were SSC, FSC, CD11b, Ly6G, CD49d, CXCR4, VEGFR1, and VEGFR2. The following SPADE parameters were used: apply compensation matrix in FCS header, Arcsinh transformation with cofactor of 150, neighborhood size of 5, local density approximation factor of 1.5, maximum allowable cells in pooled downsampled data of 50,000, target density of 20,000 cells remaining, and number of desired clusters of 100.

3.5.9 Tissue whole mount immunohistochemistry and confocal imaging

Following euthanasia, mouse vasculature was perfused with warm saline and then with 4% paraformaldehyde until tissues were fixed. The dorsal tissue was excised and permeabilized overnight at 4°C with 0.2% saponin. The tissues were blocked overnight in 10% mouse serum at 4°C. Tissues were incubated at 4°C overnight in a staining solution containing 0.1% saponin, 5% mouse serum, 0.5% fatty acid–free bovine serum albumin, and the following fluorescently conjugated antibodies: Alexa Fluor 594 anti-CD31 antibody (1:100 dilution; BioLegend) for blood vessel visualization, Alexa Fluor 488 anti-Ly6G (1:200 dilution; BioLegend) for visualization of neutrophils, and Alexa Fluor 647 anti-CD49d (1:200 dilution; BioLegend) for visualization of pro-angiogenic neutrophils. Tissues were washed four times for 30 min with 0.2% saponin and once with PBS (phosphate-buffered saline) and then mounted in 50/50 glycerol/PBS. Mounted samples were imaged on a Zeiss LSM 710 NLO confocal microscope. Crops of 332 × 332 µm at ×20 magnification in the peri-implant area were taken for image analysis in Imaris (Bitplane). Images were then blinded and rendered in Imaris by a third party. Cells expressing Ly6G or double positive for Ly6G and CD49d were identified in Imaris using the surface tool. Surfaces were identified by smoothing with a 1-µm grain size and automatic thresholding on absolute intensity. Touching objects were split using a seed points diameter of 10 µm. CD31+ vasculature was identified in Imaris using the same surface method as described above, also applying a 1-µm grain size, but instead manually selecting the threshold value optimized for each image and manually applying the volume filter to remove small debris. Distance to vasculature calculations between cells and CD31+ vasculature was made by applying a distance transformation to the CD31+ surface and recording the median position of each cell surface relative to CD31+ vessels.

3.5.10 Vascular metrics

Vascular metrics were analyzed, as described previously (13). Briefly, the mouse was mounted on a microscope stage and imaged noninvasively at ×5 magnification on a Zeiss imager D2 microscope with AxioCam MRC 5 color digital camera (Zeiss). Images were acquired on day 0 immediately following film implantation and again on day 3. Regions of interest (ROI) measuring 2000 × 2000 pixel2 were traced around the implant for further analysis. Vessels within these ROI measurements were traced, and the total vessel length per unit area was quantified via ImageJ. Arteriolar diameter measurements were measured via ImageJ, and day 3 diameters were normalized to day 0. Vascular tortuosity measurements were made within the ROIs by measuring the distance metric—the path length of a meandering curve divided by the linear distance between end points in ImageJ.

3.5.11 Cytokine measurements

For cytokine measurements, 4-mm biopsy punches of tissue centered on each biomaterial implant were harvested after euthanasia. Tissue biopsy punches were combined for each animal, digested for 30 min at 37°C in collagenase type 1A (1 mg/ml), and disaggregated through a cell strainer. Protein was isolated from the single-cell suspension in RIPA (radioimmunoprecipitation assay) buffer containing Halt Protease and Phosphatase Inhibitor Cocktail (diluted to 1×; Thermo Fisher Scientific) for 45 min on ice. Following cell lysis, total protein was obtained by centrifugation for

15 min at 14,000g and 4°C. To determine the total protein concentration in each sample, a bicinchoninic acid assay (BCA assay) was carried out using a Pierce BCA protein assay kit (Thermo Fisher Scientific) according to kit instructions. Cytokine measurements were made using the Mouse Magnetic Luminex Screening Assay (catalog number LXSAMSM, R&D Systems) according to kit instructions. Kit analytes included CXCL12/SDF-1α, FGF-β, MMP-9, and VEGF. Cytokine results were normalized to average vehicle expression at day 1 and visualized via heatmap.

3.5.12 Statistical analysis

All statistical analyses were performed using GraphPad Prism version 7.0 (La Jolla, CA). Results are presented as means ± SEM. For pairwise comparisons, unpaired two-tailed t tests with Welch's correction, if variance was significantly different, were used. For multiple comparisons, one-way analysis of variance (ANOVA) was used with Tukey's multiple comparisons when relevant. For analysis of cellular distance to vasculature, data reflect cells counted from three ROIs acquired across three to four animals per group, and statistical comparisons were made using a two-tailed Mann-Whitney test.

CHAPTER 4. CRITICAL VML INJURY IS CHARACTERIZED BY A DEFICIENCY IN PRO-RESOLVING LIPID MEDIATOR BIOSYNTHESIS THAT IS IMPROVED WITH LOCAL AT-RVD1 DELIVERY.

4.1 Introduction

Volumetric muscle loss (VML) is the partial ablation of skeletal muscle, usually on the extremities, sustained through traumatic or surgical means, such as motor vehicle accidents, military combat, or surgical resection [92]. The frank loss of musculature characteristic of VML sufficiently disrupts or eliminates the wound's endogenous repair mechanisms, such that healing becomes very difficult usually resulting in substantial scar tissue formation; these injuries subsequently result in permanent functional impairments and chronic pain [93]. Given the lack of treatment options, many groups have investigated various regenerative medicine approaches, including implantation of cellular/acellular scaffolds formed by *in situ* bioprinting, direct injection, or implantation of pre-fabricated scaffolds that serve as immunomodulators of the injury milieu [2, 94-96]. However, comparably, there is a lack of targeted immunomodulation of the VML environment; heightened by the fact that the quality of tissue healing is strongly linked to the immune cell recruitment dynamics and functions in the hours, days, and weeks post-injury [97]. VML results in persistent inflammation characterized by the inability to resolve, excessive fibrosis, fatty infiltration and healing delay [98]. Skeletal muscle is not well adapted to chronic injury stimulus and host mechanisms of inflammation resolution fail to trigger the shift in local immune cells from a transient pro-inflammatory state to anti-inflammatory, pro-regenerative state [99]. VML and other traumatic injuries can lead to chronic inflammation in the wound, characterized by dysregulation of macrophage recruitment and polarization, persistence of CD4$^+$ T cells and CD8$^+$ T cells [100]. Moreover, dysregulated immune cell signaling can also drive muscle resident cells such as fibro/adipogenic progenitor cells (FAPs) towards a pro-fibrotic, rather than myogenic state [101]. Limiting the extent of inflammation at onset and by antagonizing common initiators of inflammation directly (e.g., cytokines), can also cause unwanted side effects, including immunosuppression, poor vascularization, and delayed wound repair [102, 103]. Therefore, in contrast to conventional ‘anti-inflammatory’ strategies, resolution-pharmacology strategies that harness endogenous resolution mechanisms to limit tissue destruction and fibrosis, while also maintaining pro-regenerative functions hold significant therapeutic promise [102-104].

Recent studies suggest a novel role for specialized pro-resolving lipid mediators (SPMs) to enhance muscle regeneration [49, 52, 72, 105, 106]. After tissue injury or trauma, pro-inflammatory eicosanoids (prostaglandins and leukotrienes) are crucial in initiating the first stages of inflammation. These mediators, along with many cytokines, chemokines and complement components, stimulate the migration of neutrophils to the tissue [107]. SPMs are a family of bioactive lipids produced during inflammation and actively reprogram the immune response to resolve inflammation and re-establish tissue function [24, 108]. As part of the neutrophil-monocyte temporal transition, accumulated prostaglandins, among other mechanisms, induce a lipid mediator class switch by switching on the transcription of enzymes required for the biosynthesis of multiple SPM families derived from the conversion of omega-3 fatty acids – Lipoxins, Resolvins, Protectins and Maresins [109]. Generally, the Lipoxins and Resolvins act to stop leukotriene-stimulated neutrophil influx and regulate nonphlogistic recruitment of monocytes. Resolvins, along with the other SPMs - Protectins and Maresins - stimulate efferocytosis of apoptotic neutrophils and cellular debris by macrophages [24, 110]. Increased efferocytosis also induces a phenotypic switch in macrophages from a pro-inflammatory M1 to a pro-regenerative M2 phenotype [24]. As macrophages shift from an M1 to an M2 phenotype, they also alter their metabolism from biosynthesis of pro-inflammatory eicosanoids to pro-resolving SPMs [111, 112], producing a powerful feedback loop that further enhances inflammation resolution that eventually leads to a restoration of normal structure and homeostasis. Moreover, stereoisomers of many of these SPMs are preferentially produced in the presence of aspirin – referred often as 'Aspirin Triggered' species. For instance, AT-RvD1 is the stereoisomer of 17S-Resolvin D1 derived from DHA in the presence of aspirin [113]. Specifically, 17-R isomers of RvDs are produced when aspirin acetylates COX-2 to produce 17R-alcohol-containing intermediates that are then converted by 5-LOX [32]. In addition to aspirin, N-acetyl sphingosine, generated via a sphingosine kinase 1-dependent pathway, also acetylates COX2 to produce the 17R-RvDs [33]. The 17R epimer has a conformation that is resistant to rapid enzymatic degradation, while maintaining the biological function as an agonist of ALX/FPR2, a receptor implicated in inflammation resolution via various mechanisms [114, 115].

Imbalances in bioactive lipid mediators can lead to failed resolution that may underlie the persistent inflammation and fibrosis associated with many diseases or trauma, and there is growing appreciation for the potential to exploit the biology of resolution by systemic administration of SPMs to enhance healing and regeneration [49, 52, 72, 105, 106, 116]. However, systemic delivery may result in suboptimal drug concentration at the site of injury and the potency of SPMs in the trauma microenvironments, such as VML, may rely upon close-range interactions and signaling due to the short-lived nature of these bioactive lipid mediators. With this in mind, our group has developed different biomaterial-based local delivery strategies of SPMs to maximize their therapeutic efficacy [117, 118]. In this study, we show that the local and early presentation of AT-RvD1 via synthetic hydrogels significantly increases *in vivo* biosynthesis of multiple other SPMs and initiates a pro-regenerative shift in the immune cell composition in the muscle injury niche that leads to an increase in the concentration of muscle progenitor cells (Fig. 19).

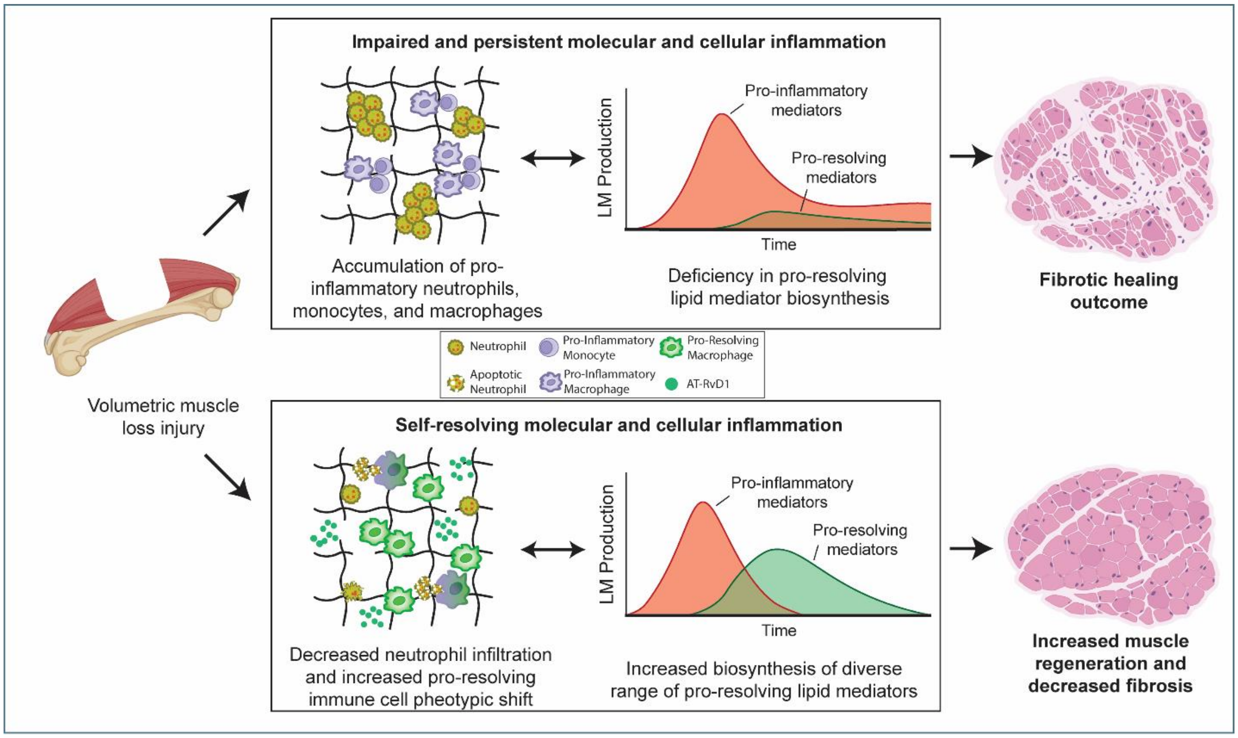

Figure 19. Chapter 4 graphical abstract.

4.2 Results

4.2.1 The pro-inflammatory to pro-resolving lipid mediator class switch is dysregulated after VML injury

To our knowledge, SPM metabolism after a volumetric muscle loss injury has not been characterized. Thus, we performed targeted mass-spectrometry to target pro-inflammatory eicosanoids and SPMs using a quadricep murine VML injury that we have previously characterized. This characterization defined an injury size threshold below of which the injury is sub-critical and above of which it is a critical, non-healing injury (37, 38) (Fig. 20A). We performed both extents of injury and compared the sub-critical to a critically sized VML injury at both 3 days and 7 days post injury. The data is represented as a fold change heatmap between critical and sub-critical VML injury (Fig 1B-I). When overlayed onto the Arachidonic Acid (AA), Eicosapentaenoic acid (EPA), and Docosahexaenoic acid (DHA) metabolic pathways, we see that at 3 days post injury that, regardless of injury severity, many SPMs were not detected in VML injury, with the exception of RvE1 and PDx (10S, 17S-dihydroxydocosahexaenoic acid). Rather, the response is characterized by predominance of pro-inflammatory eicosanoids, such as LTB4 (Fig. 20C-E). This is further highlighted by the accumulation of monohydroxy intermediates (e.g. 17-HDHA, 14-HDHA)in SPM pathways rather than their downstream SPM products (Fig. 20E). Furthermore, the severity of injury exacerbated this phenomenon as seen by the increase in the concentration of LTB4 and monohydroxy intermediates with no net change in RvE1 (Fig. 20B). A similar outcome of mediator metabolism is observed at day 7 post-VML, where prostanoids and LTB4 were the predominant products, which further suggests that the lipid mediator class switch from pro-inflammatory to pro-resolving lipid mediators, that other studies in acute muscle injuries show occurs early in the inflammatory cascade (17), is dysregulated after a VML injury (Fig. 20F-

I). These initial results led us to investigate the lipid mediator response to critical VML at multiple timepoints to measure the concentration of lipid mediators at different stages of inflammation.

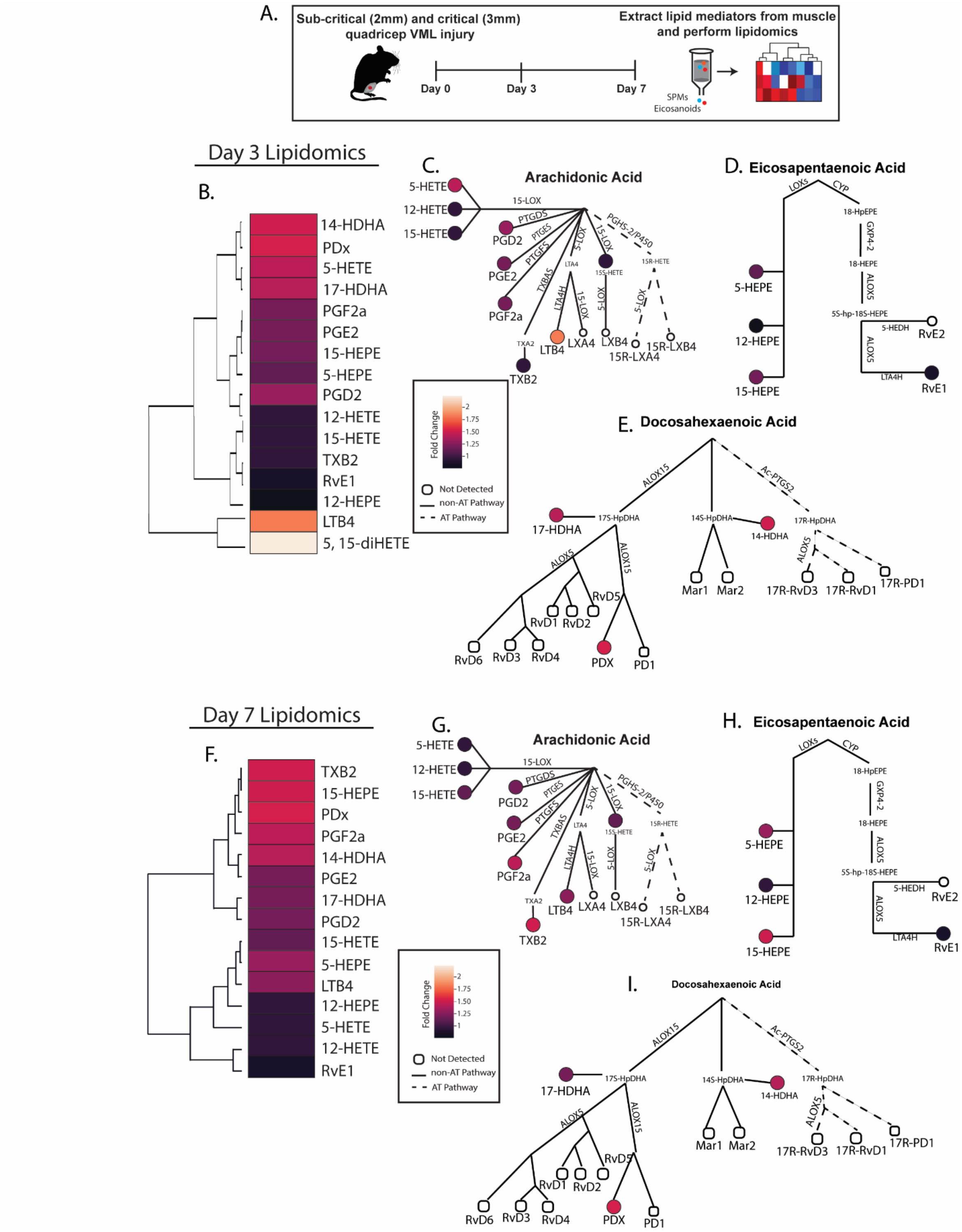

Figure 20. Targeted LC-MS/MS after VML injury reveals impaired production of specialized pro-resolving mediators.
(A) Schematic illustrating the experimental design.(B) Heatmap illustrating the fold change (critical/sub-critical VML) of lipid mediators between crucial and sub-critical injuries at 3 days post VML. (C-E) The day 3 fold change heatmap is overlayed onto the AA, EPA, and DHA metabolic pathways. (F) Heatmap illustrating the fold change (critical/sub-critical VML) of lipid mediators between crucial and sub-critical injuries at 7 days post VML. (G-H) The day 7 fold change heatmap is overlayed onto the AA, EPA, and DHA metabolic pathways. Heatmaps were created from the average concentration from n=5 animals per group.

4.2.2 *Local AT-RvD1 delivery via PEG-4MAL hydrogels after VML increases the biosynthesis of a broad spectrum of SPMs.*

We leveraged the engineered hydrogel that we tested in the dorsal skinfold window chamber model in chapter 3 as a therapeutic for VML injuries. This hydrogel was designed to activate local pathways of inflammation resolution using a synthetic hydrogel platform based on a four-arm poly(ethylene glycol) (PEG) macromer functionalized with maleimide groups for local, controlled delivery of SPMs [119, 120]. In this synthetic design, the maleimide in PEG-4MAL macromers were functionalized with thiol-containing cell-adhesive peptide via Michael-type addition. These functionalized macromers are then crosslinked through the reaction of the remaining maleimides with cysteine-flanked protease-degradable peptides to yield a crosslinked hydrogel that is enzymatically degraded in vivo [121]. This crosslinking reaction is performed in the presence of AT-RvD1 (17R-Resolvin D1) to encapsulate this SPM; this process generates a hydrogel that will locally releases the pro-resolving molecule and activate the resolution of inflammation (Fig 21A). This synthetic hydrogel construct was characterized in previous studies and bioactive AT-RvD1 was found to be released within the first 24 hours making it bioavailable to the infiltrating pro-inflammatory cells early in the inflammatory cascade [119] (Fig 21B). We posit that the early presentation of AT-RvD1 will push the inflammatory response towards a pro-resolving cascade rather than a persistent and chronic one (Fig 21B). The model we used to characterize the pro-resolving hydrogel is a VML pre-clinical murine model in which we induce a full-thickness defect in the spinotrapezius muscle (Fig 21C). The hydrogel was injected for in situ gelation directly into the muscle void (Fig 21D). This model allows us to investigate the effects of the therapeutic platform on the cellular environment and lipid-mediator biosynthesis while also allowing for whole-mount microscopy to easily observe muscle fibre regeneration.

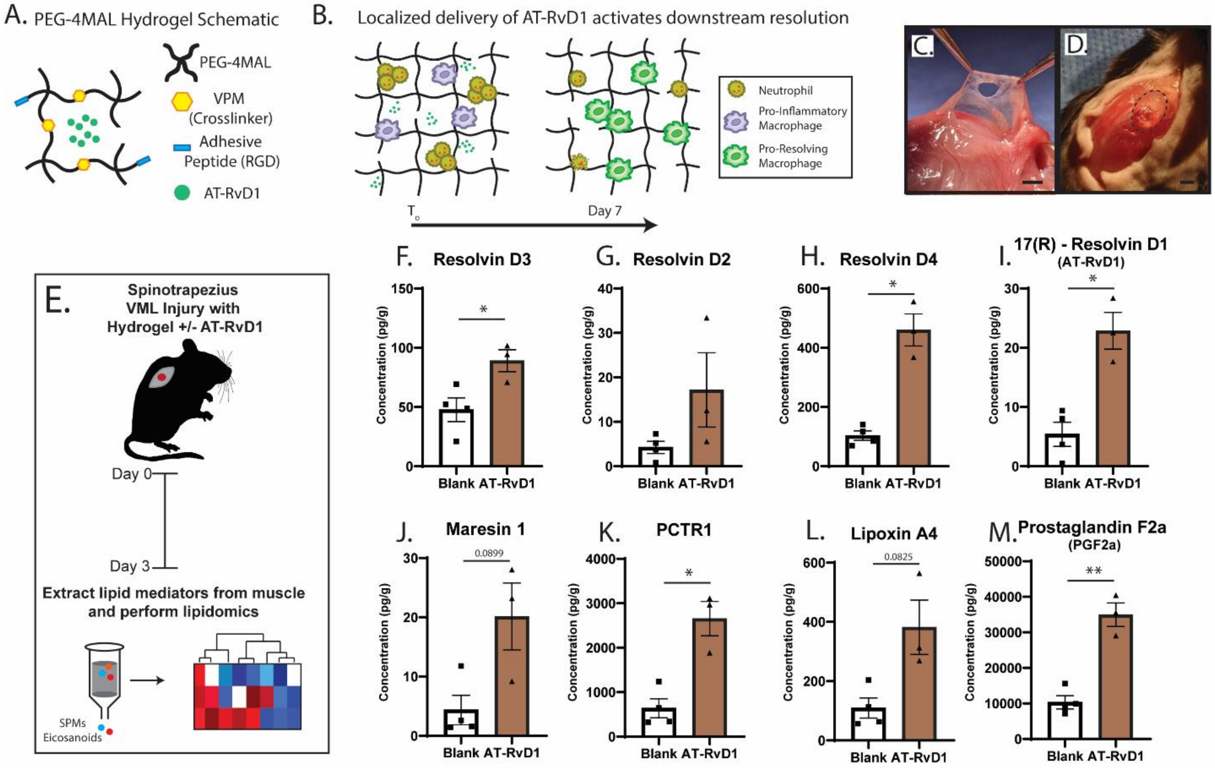

Figure 21. Local delivery of AT-RvD1 via PEG-4MAL hydrogel increases the concentration of specialized pro-resolving mediators.

Protease degradable hydrogels were designed to locally deliver AT-RvD1 by functionalizing PEG-4MAL with an adhesive peptide (RGD) and crosslinking it with an MMP-cleavable crosslinker (VPM) in the presence of AT-RvD1. (B) The downstream inflammatory cascade is reprogrammed towards resolution via the early and local presentation of AT-Rvd1. (C and D) A volumetric muscle loss injury is induced in the spinotrapezius muscle and the hydrogel injected to fill the injury void. (E) Modulation of the pro-inflammatory Eicosanoid and Specialized pro-resolving lipid mediator landscape was analyzed via LC/MS-MS three days post VML. (F-Q) Concentration of lipid mediators were quantified and select lipids shown are elevated after AT-RvD1 delivery compared to a blank hydrogel control. Statistical analyses were performed using two-tailed t tests; $*P < 0.05$; n = 3 to 4 animals per group. (C

We compared the ability of local hydrogel-mediated AT-RvD1 delivery to a control hydrogel (without AT-RvD1) to influence downstream production of key SPMs in muscle tissue using mass-spectrometry based lipidomics 3 days post VML injury (Fig 21E). With this method, we detected significant differences in the concentration of not only AT-RvD1 (AKA 17R-RvD1), but also a range of other D-series resolvins when compared to a control (no AT-RvD1) PEG-4MAL hydrogel (Fig. 21F-J). Additionally, the hydrogel delivery of AT-RvD1 increased the production of specific lipids on other metabolic pathways, such as, Protectin Conjugates in Tissue Regeneration 1 (PCTR1), Lipoxin A4 (LXA4) and Maresin 1 (MaR1) (Fig 21L,N).

To visualize the effect of the pro-resolving hydrogel on the greater metabolic network from which pro-inflammatory eicosanoids and SPMs are derived, we overlayed a fold change (AT-RvD1 versus control) heatmap onto the DHA, EPA and AA metabolic networks (Fig 22A-C). This visualization shows that many metabolic pathways are activated with AT-RvD1 delivery as compared to a control hydrogel. In the DHA pathway the most upregulated lipid mediators, Resolvin D4 (RvD4), MaR1, and AT-RvD1, are from different pathways within the metabolic network (Fig 22C). These broad effects are represented by the significant increase in total SPMs and D-series Resolvins along with the trending increase in total Maresins and total Lipoxins (Fig 22D-H). These differences are seen at 3 days post VML in the AT-RvD1 loaded hydrogel treated group, indicating that the initial presentation of an SPM is able to exert significant pro-resolving effects at a stage when the environment is no longer being supplied with external AT-RvD1.

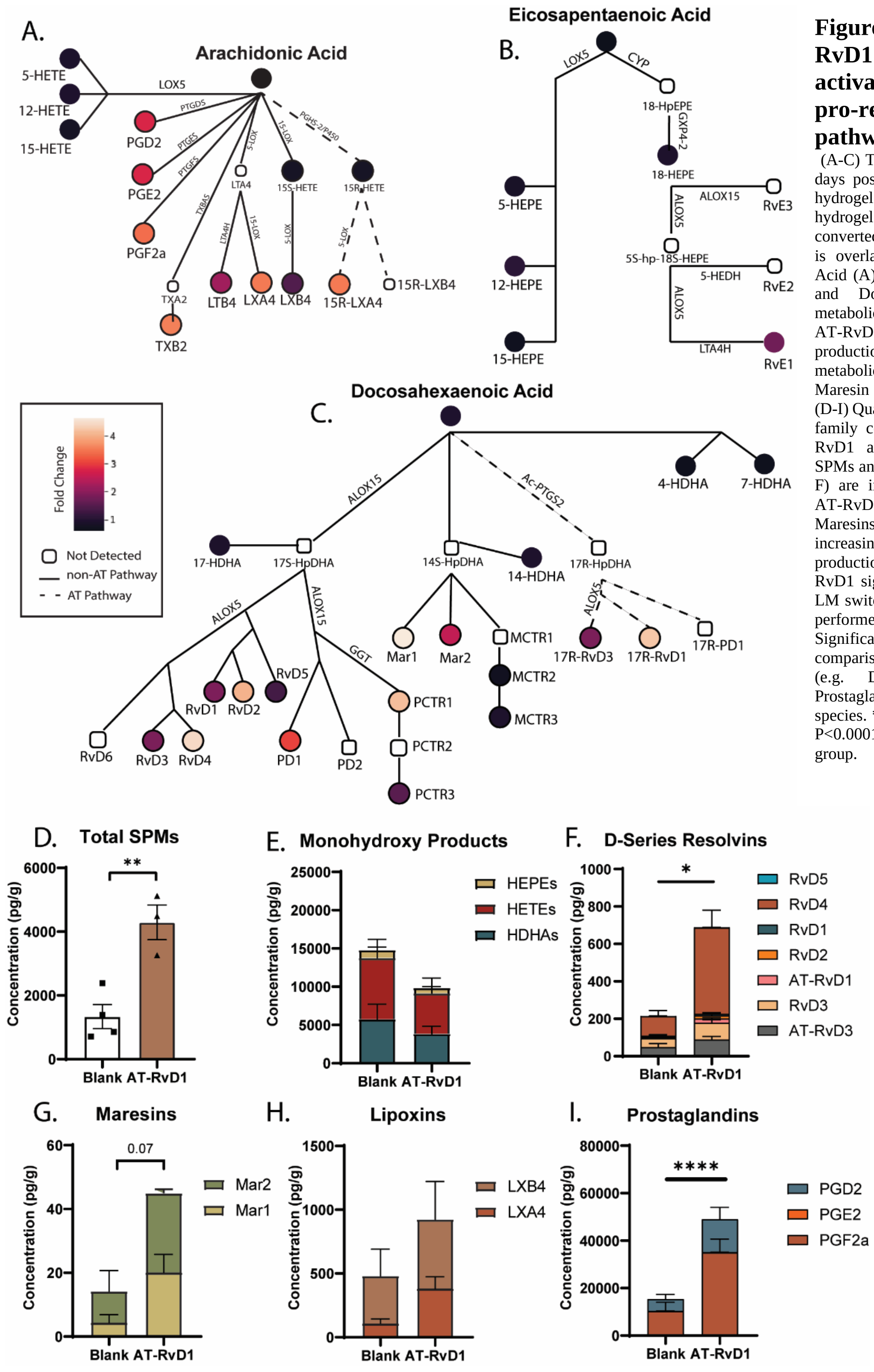

Figure 22. Local AT-RvD1 presentation activated a diverse set of pro-resolving metabolic pathways.
(A-C) The fold change difference 3 days post VML between AT-RvD1 hydrogel treatment and blank hydrogel controls was calculated and converted to a heatmap. This heatmap is overlayed onto the Arachidonic Acid (A), Eicosapentaenoic Acid (B) and Docosahexanoic Acid (C) metabolic pathways and shows that AT-RvD1 delivery promotes the production of SPMs on distinct metabolic pathways; such as, Maresin 1, Resolvin D4 and PCTR1. (D-I) Quantification of lipid mediator family concentrations between AT-RvD1 and blank hydrogel. Total SPMs and D-series Resolvins (D and F) are increased significantly with AT-RvD1 while total Lipoxins and Maresins (G and H) show an increasing trend. (I) Prostaglandin production is promoted with AT-RvD1 signaling the initiation of the LM switch. Statistical analyses were performed using two-tailed t tests; Significance values are for the comparison between total groups (e.g. D-Series Resolvins and Prostaglandins) not individual sub-species. *P < 0.05, **P < 0.01, **** P<0.0001; n = 3 to 4 animals per group.

4.2.3 SPADE analysis of immune response to VML identifies an "aged" neutrophil subpopulation decreased with AT-RvD1 delivery

To examine the impact of modulating SPM metabolism in the local VML injury niche on the cellular niche, we performed flow cytometry and unsupervised trajectory analysis of VML injuries in the spinotrapezius muscle using the Spanning Tree Progression of Density Normalized Events (SPADE) algorithm. We first looked at the neutrophil cell compartment because it is essential in priming the inflammatory response towards either resolution or persistence [122, 123]. In the case of persistent inflammation produced by critical VML, neutrophils can exhibit an aged phenotype prone to develop neutrophil extracellular traps (NET) that promote further inflammation and activate fibrotic pathways [124] (Fig 23A). To identify rare neutrophil subsets we have previously leveraged the dimensionality reduction and clustering technique SPADE [122, 125].

Visualization of CD11b+Ly6G+ tree revealed a cluster of neutrophils consistent with “aged” phenotype (Fig 23B). This aged phenotype was characterized by low expression of CD62L and high expression of CD49D and CXCR4. Additionally, this subset also has a high expression of

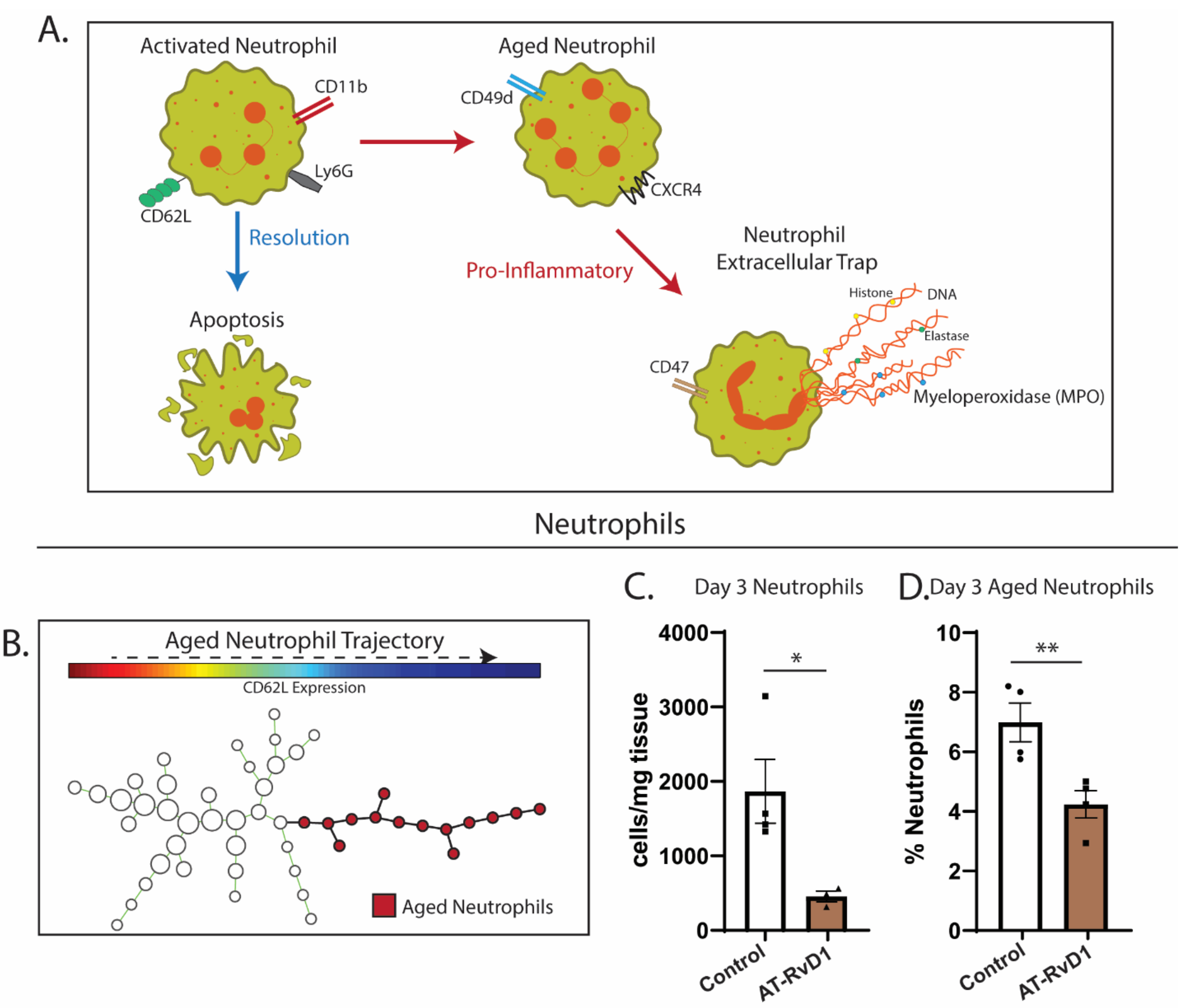

Figure 23. AT-RvD1 loaded hydrogels delivered to a VML injury limits neutrophil accumulation and pro-inflammatory polarization. (A) Activated neutrophils (CD11b+LY6G+CD62L+) accumulate in the initial stages of inflammation and are cleared via apoptosis and efferocytosis during active resolution. However, in the case of persistent inflammation neutrophils accumulate and polarize towards an aged phenotype (CD11b+Ly6G+CD49d+CD62L-CXCR4+) that can evade phagocytosis (CD47+) and are prone to generate neutrophil extracellular traps (MPOhigh). (B) Traditionally gated CD11b+Ly6G+ neutrophils were analyzed via SPADE to identify an aged neutrophil trajectory. (C and D) This analysis shows that AT-RvD1 was able to reduce the total concentration of neutrophils in the tissue (C) and was also able to limit the polarization of neutrophils to the aged phenotype (D). Statistical analyses were performed using two-tailed t tests; $*P < 0.05$, $**P < 0.01$; n = 3 to 4 animals per group.

CD47, a marker that allows cells to evade phagocytosis, and MPO, a key component of NETs. This neutrophil subset was identified via the multiple comparison SPADE algorithm that detects rare cell subsets that is most sensitive to a given perturbation, in this case AT-RvD1 treatment (Fig 23B). With the local delivery of AT-RvD1, the total concentration of neutrophils in the muscle tissue at 3 days post VML was significantly decreased compared to hydrogel controls (Fig 23C). Furthermore, the pro-resolving hydrogel reduced the polarization of activated neutrophils toward a pro-inflammatory aged phenotype (Fig 23D). This modulation of neutrophil infiltration and phenotype indicated that local AT-RvD1 is promoting cellular resolution of inflammation.

4.2.4 Local AT-RvD1 presentation induces a pro-regenerative mononuclear phagocyte phenotype polarization after VML.

The timely resolution of inflammation is driven by the shift from pro-inflammatory (M1) macrophages to pro-resolving or pro-regenerative (M2) macrophages [28]. This shift involves the recruitment of either inflammatory or "classical" monocytes that differentiate into M1 macrophages or recruitment of anti-inflammatory or "non-classical" monocytes that differentiate into M2 macrophages. Additionally, M1 macrophages can polarize in situ to M2 macrophages that produce large amounts of SPMs that further promote inflammation resolution [28] (Fig. 24A). The effect of local AT-RvD1 delivery on this pro-resolving shift was quantified in the spinotrapezius muscle after VML injury via SPADE analysis. A monocyte SPADE tree was constructed using CD11b+CD64+Mertk- monocytes and clustering identified a separation between Ly6C-high inflammatory and Ly6C-low anti-inflammatory monocytes (Fig. 24B). Quantifying these monocyte cell subsets, AT-RvD1 treatment was found to significantly increase the concentration of anti-inflammatory monocytes at day 7 post VML (Fig. 24C and D). Similarly, a macrophage SPADE tree of CD11b+CD64+Mertk+ macrophages revealed a shift in the proportion of CD206-

Ly6C-high M1 and CD206+Ly6C-low M2 macrophages (Fig. 24E). AT-RvD1 promotes the M1 to M2 macrophage switch resulting in the significant decrease in M1 macrophages at day 3 and the significant increase in M2 macrophages at day 7 post VML (Fig 24F and G). Taken together, these data indicate that local AT-RvD1 presentation shifts the distribution of mononuclear phagocytes towards a pro-regenerative phenotype.

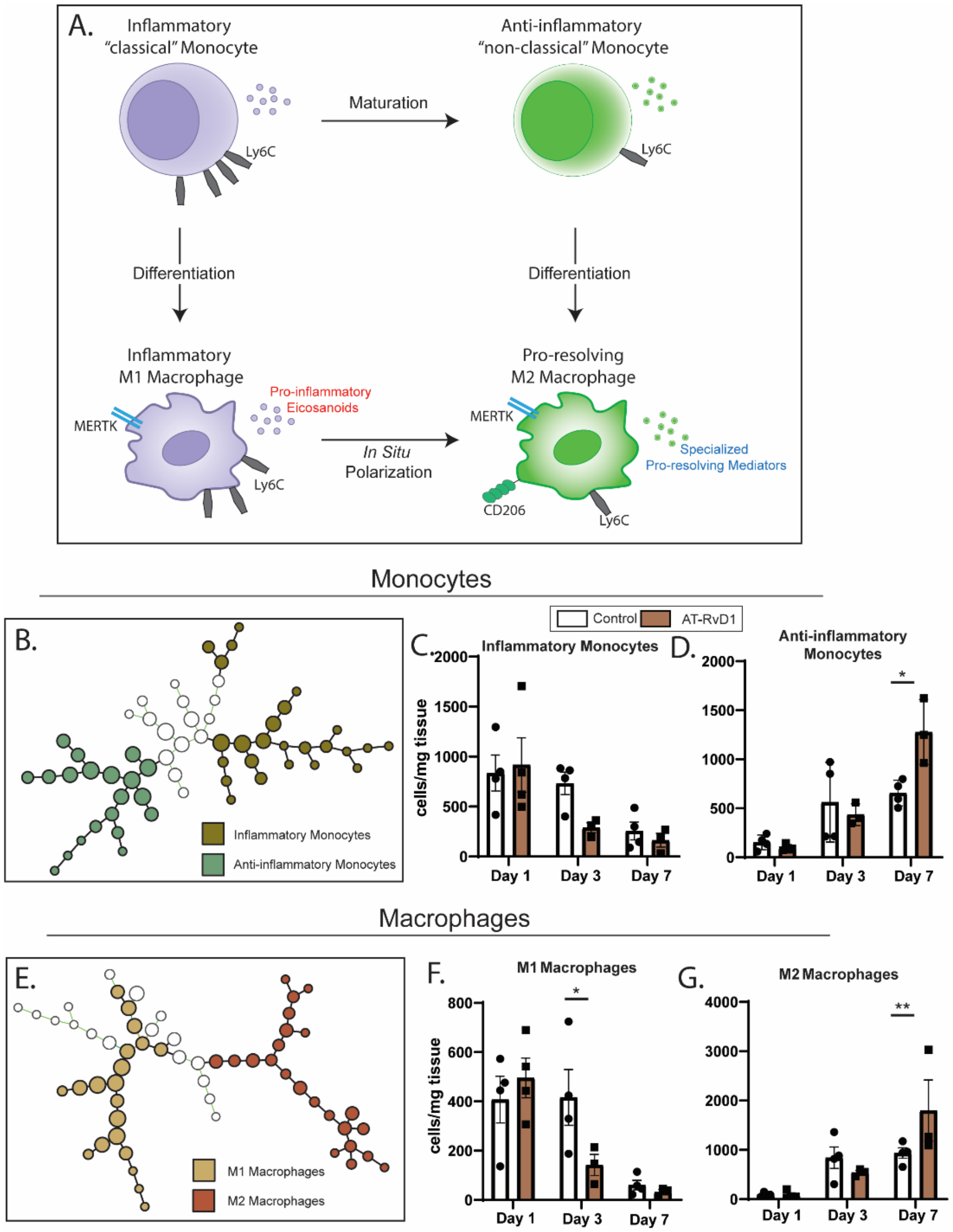

Figure 24. Early At-RvD1 delivery induces a downstream pro-regenerative cellular niche. (A) Inflammatory “classical” monocytes (CD11b+Cd64+Mertk-Ly6chigh) and anti-inflammatory “non-classical” monocytes (CD11b+CD64+Mertk-Ly6clow) are recruited from circulation and differentiate into inflammatory M1 macrophages (CD11b+CD64+Mertk+CD206-Ly6chigh) or pro-resolving M2 macrophages (Cd11b+CD64+Mertk+CD206+Ly6clow), respectively. M1 macrophages can also go through *in situ* polarization into M2 macrophages that produce high levels of SPMs. (B) traditionally gated CD11b+CD64+Mertk- Monocytes were analyzed via SPADE to identify the inflammatory and anti-inflammatory phenotypes. (C and D) The concentration of these monocyte subsets was quantified in the muscle tissue, with AT-RvD1 delivery significantly increasing AMs at day 7 post VML. (E) Traditionally gated CD11b+CD64+Mertk+ macrophages were analyzed via SPADE to identify M1 and M2 macrophages. (F and G) The concentration of these macrophage subsets were quantified in the muscle tissue, with M1 macrophages significantly lower at day 3 with AT-RvD1 and M2 macrophages significantly higher at day 7 with AT-RvD1. Statistical analyses were performed using a two-way analysis of variance (ANOVA) with Sidak’s multiple comparisons and the Geisser-Greenhouse correction to account for the differences in variability amongst groups; *$P < 0.05$, **$P < 0.01$; n = 3 to 4 animals per group.

4.2.5 *Local AT-RvD1 acts on muscle progenitor cells to increase the skeletal muscle regenerative capacity post VML.*

To analyse the effect of local AT-RvD1 delivery on the local pool of the two main muscle progenitor cells – MuSCs and FAPs, we quantified the concentration of these cells at days 1, 3 and 7 post VML in the spinotrapezius muscle (Fig 25). A SPADE tree of all lineage- cells was constructed and clustering identified distinct trajectories comprised of FAPs (CD31-SCA1+) and comprised of MuSCs (CD31-SCA1-CD29+CXCR4+). FAPs and MuSCs work in concert to provide the necessary extracellular matrix structure and muscle fiber formation for ideal regeneration to take place [7]. When quantifying the SPADE-identified population of MuSCs and FAPs, AT-RvD1 hydrogel treatment was able to significantly increase both populations when compared to control hydrogel at 7 days post VML (Fig 25A and B).

Previous studies have shown that resolvins can have a direct effect on MuSCs to both proliferate and differentiate these cells to increase myotube formation [51, 52, 72]. However, the effect that resolvins have on FAPs has yet to be explored. Thus, we FACS sorted FAPs from muscle tissue and cultured them for downstream analysis (Fig 25C-E). We stained FAPs with DAPI (blue) and F-actin (white) to visualize the cells along with a-SMA (red) and B1-int (green) to quantify their fibrotic differentiation (Fig 25C). We then treated the cells with AT-RvD1 with or without TGF-B stimulation and quantified the fluorescence intensity of a-SMA and B1-int. As expected, TFG-B stimulation increased the fluorescent intensity of both a-SMA and B1-int. When treated with AT-RvD1, the expression of a-SMA became similar to that of non TGF-B stimulated FAPs (Fig 25D). Additionally, the expression of B1-int of TGF-B stimulated FAPs was significantly decreased when treated with AT-RvD1 (Fig 25E). This indicates that in addition to acting on immune cells to promote resolution, AT-RvD1 is able to act not only on MuSCs to promote their proliferation and differentiation but also on FAPs to limit their fibrotic differentiation.

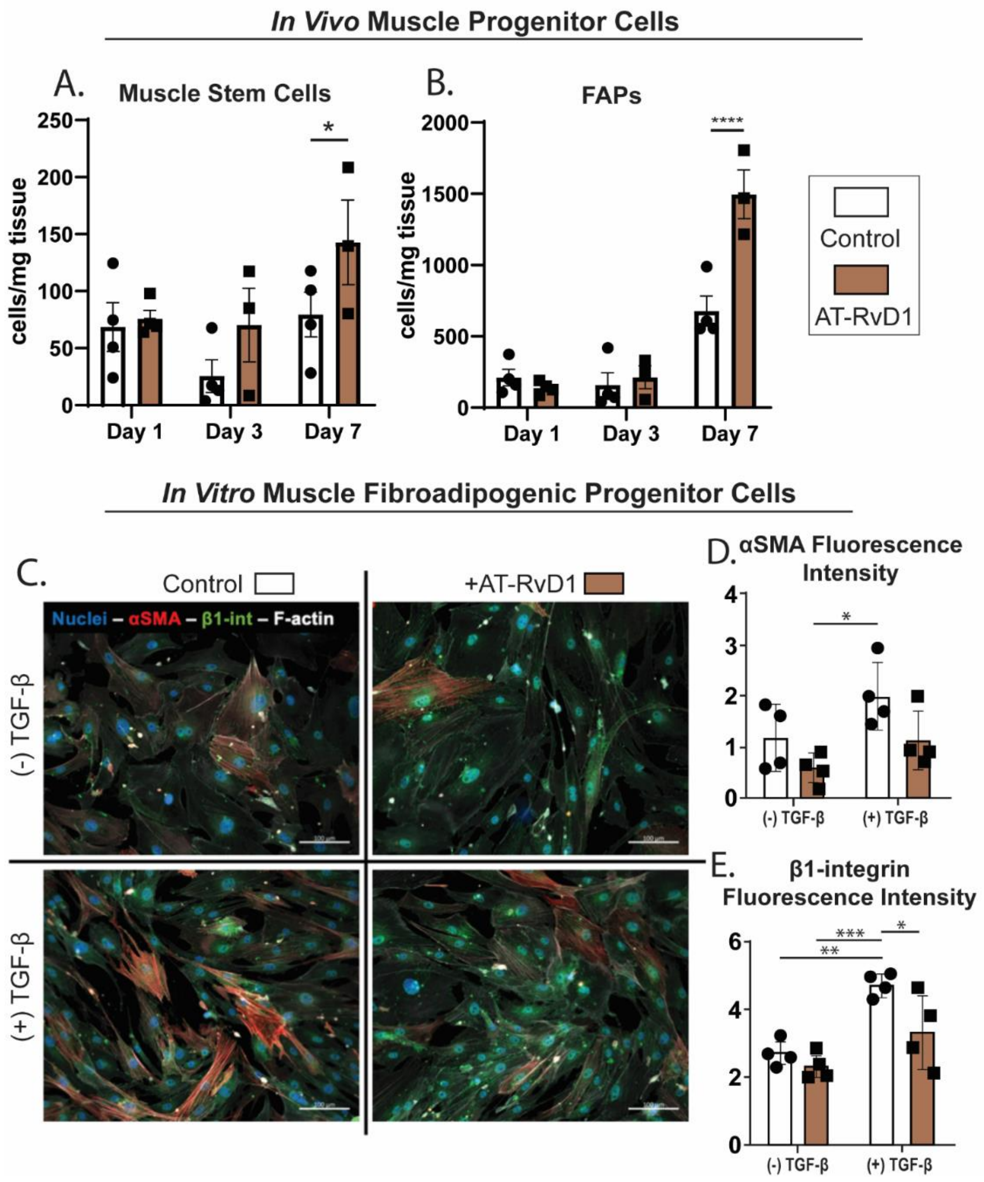

Figure 25. The pro-resolving tissue microenvironment induced via AT-RvD1 delivery increases skeletal muscle regenerative capacity.

(A) Traditionally gated Lineage- cells were analyzed via SPADE to identify MuSCs (Lin-CD31-SCA1-CD29+CXCR4+) and FAPs (Lin-CD31-SCA1+). (B and C) The concentration of MuSCs and FAPs were quantified in the muscle tissue and seen to be higher with AT-RvD1 delivery at day 7 post VML. (D) FACS-sorted FAPs from muscle tissue were stained with aSMA and B1-int to track their fibrotic differentiation in the presence of AT-RvD1 with or without TGF-B stimulation. (E and F) Fluorescence intensity of aSMA (E) and B1-int (F) show that AT-RvD1 directly interacts with FAPs to decrease their fibrotic differentiation. Statistical analyses were performed using a two-way analysis of variance (ANOVA) with Sidak’s multiple comparisons and the Geisser-Greenhouse correction to account for the differences in variability amongst groups; *P < 0.05 and **P < 0.01; n = 3 to 4 animals per group (A-C); n=4 (D – F)

4.2.6 *Whole mount spinotrapezius muscle IHC and SHG reveals that pro-resolving hydrogel treatment after VML results in near complete closure of VML defect with improved muscle fiber and collagen organization.*

The spinotrapezius pre-clinical VML model has the unique advantage of having the ability to be whole mounted for full thickness confocal microscopy. This allows us to analyze the extent of VML defect closure with and without AT-RvD1 hydrogel treatment. At 14 days post VML injury we stained the spinotrapezius muscle with desmin (cyan; muscle fibers), CD68 (blue; macrophages) and CD206 (green, M2 surface marker) (Fig 26A-C). When quantifying the defect area size, both the control hydrogel and AT-RvD1 hydrogel had a significantly smaller defect area when compared to the untreated VML injury (Fig 26D). Furthermore, AT-RvD1 loaded hydrogels has a defect area that was significantly smaller than control hydrogels with near complete closure (Fig 26D). The CD68 and CD206 staining also shows that M2 macrophages (showing expression of both surface markers) tend to cluster around newly generated fibers. Qualitatively, we observe that these cells are constrained to the outer edges of the defect without much infiltration into the centre of the defect with a control hydrogel (Fig 26B). With AT-RvD1 loaded hydrogels M2 macrophages can be seen spread throughout the defect area (Fig 26C)

Additionally, second harmonic generation imaging was leveraged to produce data within one mean-free-path from the surface of untreated, control hydrogel, AT-RvD1 hydrogel and healthy mouse spinotrapezius whole mount slides. Angular Fourier filter (AFF) was used for the polarimetric analysis of muscle structures [126]. Representative polarization-encoded presentation of the polarimetric data at 14 days post spinotrapezius VML of the four experimental groups is shown (Fig 26E-L). Qualitatively, the AT-RvD1 treated VML injury is seen to have a more developed and well-defined collagen and muscle fiber structures similar to that of the healthy

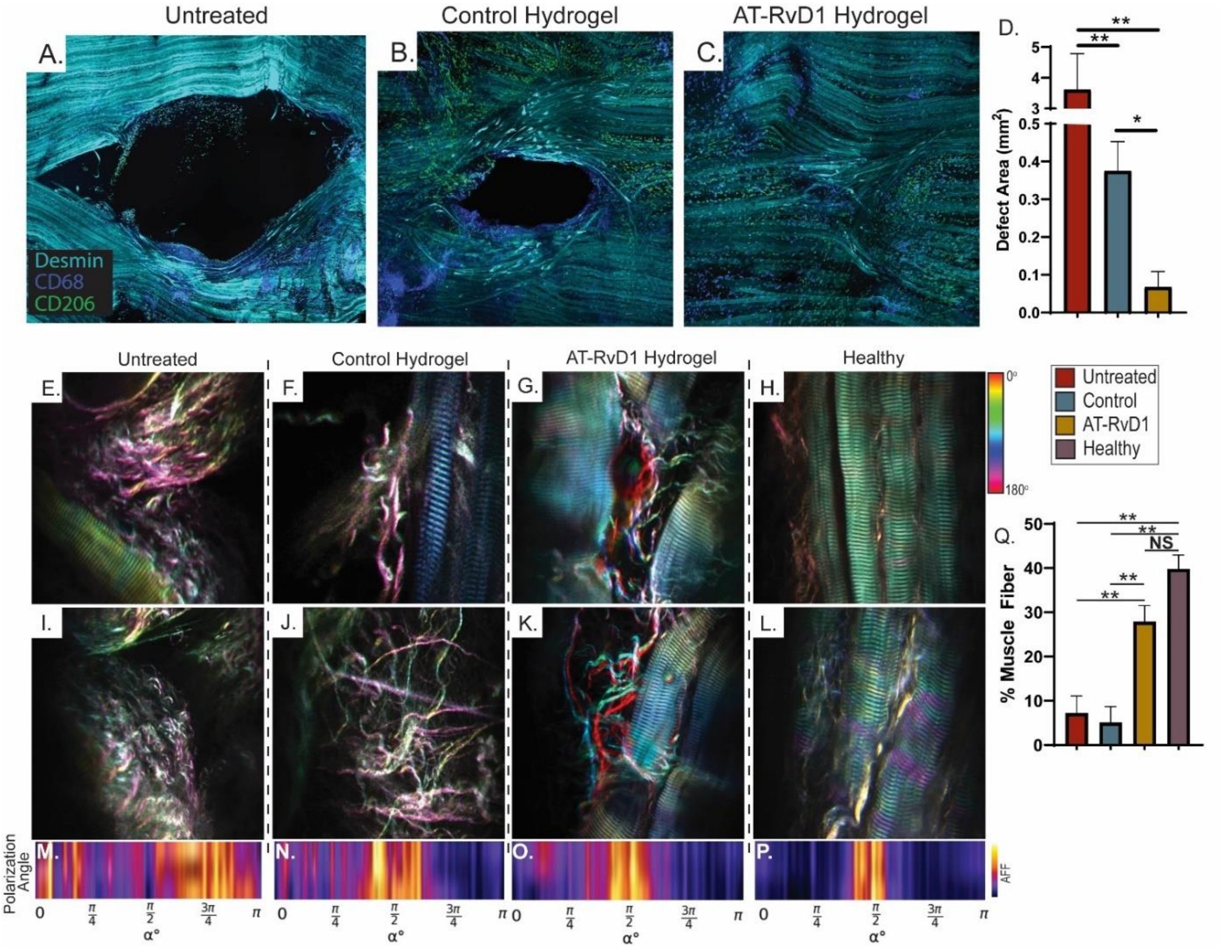

Figure 26. AT-RvD1 loaded hydrogel treatment improves muscle regeneration and recovers collagen organization 14 days post VML injury.

(A-C) Representative images of whole-mount spinotrapezius confocal miscroscopy 14 days post VML injury. Desmin (cyan) stains muscle fibers, CD68 (blue) stains macrophages, CD206 (Green) identifies CD68+ M2 macrophages. (D) Quantification of the defect area (area not covered in Desmin+ muscle fibers) shows a significant decrease in defect size with AT-RvD1 hydrogel treatment as compared to both blank and untreated controls. (E-L) Second harmonic generation data was recorded within one mean-free-path from the surface of untreated, control hydrogel, AT-RvD1 hydrogel and healthy mouse spinotrapezius muscle. (E/I), (F/J), (G/K) and (H/L) show a correspondingly polarization-encoded presentation of representative polarimetric data from areas around the edges of the defect. The angular Fourier filter (AFF) histograms are shown in (M-P). The AFF analysis shows that the muscle with an organized collagen network produces strong peaks suggests the strong organization of the structure. The untreated (M) and control hydrogel (N) muscle produce angularly scattered peaks at all polarimetric status. Therefore, the AFF analysis does not produce any significant peak. AT-RvD1 treated hydrogel (O) and healthy (P) mouse spinotrapezius muscle shows strong peaks that follow a sinusoidal trend with the input polarization. (N) shows the percentage of muscle fiber area over whole image, which represents how compact the muscle fibers are in each condition. Statistical analyses were performed using a one-way analysis of variance (ANOVA) with Tukey's multiple comparisons; *P < 0.05 and **P < 0.01; n = 3 to 4 animals per group.

muscle (Fig 26E-L). AFF is able to detect the presence of a loose and less-organized collagen network versus one that is more defined and mature [126]. A heatmap of the AFF is more clearly able to represent the dominant peaks of an organized collagen and muscle fiber network (Fig 32M-P). In both untreated and control hydrogel samples the AFF analysis does not produce any significant peak but rather shows angularly scattered peaks (Fig 26M and N). Alternatively, healthy and AT-RvD1 hydrogel treated VML muscle shows strong peaks that follow a sinusoidal trend with the input polarization (Fig 26O and P). These results indicate that without treatment and with a control hydrogel collagen network disruption continues at 14 days post VML injury, with little muscle fiber regeneration. When treated with AT-RvD1 hydrogels, the regenerated muscle 14 days post VML injury is able to recover this organization and has well-defined collagen fibers similar to that of healthy muscle along with multiple muscle fibers in the defect region. Furthermore, as a measure of muscle fiber compactness, percent area of muscle fiber was quantified with AT-RvD1 treated muscle seen to be not statistically different from healthy muscle but statistically different than both control hydrogel and untreated VML muscle (Fig 26Q). Taken together, this data suggests that AT-RvD1-loaded hydrogel treatment after VML injury results in significant muscle defect closure characterized by compact muscle fibers with a defined and organized collagen and muscle network.

4.3 Discussion

Volumetric muscle loss (VML) injuries carry significant healthcare burden. In addition to vehicular accidents or penetrating blast wounds, VML can also occur in non-traumatic scenarios including congenital birth defects and tumor resection [92]. Moreover, extremity trauma often results in damage to multiple tissue types. Current clinical strategies for VML treatment include muscle flap autografts and free tissue transfer that, while salvaging the injured limb, are often no better than amputation in terms of functional improvement and patient quality of life [127, 128]. Limited treatment success of bioactive materials, such as decellularized skeletal muscle and porcine small intestine submucosa (SIS-ECM), has been reported in preclinical models but these approaches may also lead to significant fibrosis and fat infiltration [129-131]. Cell-based therapies including delivery of muscle stem cells (MuSC) are also able to promote newly formed aligned functional fibers in thin and partial thickness preclinical VML defect models [132-134]. However, the persistent inflammation of large volume skeletal muscle can overwhelm myogenic cells and often leads to fibrosis. These outcomes highlight the need for a more targeted approach to resolve the inhospitable microenvironment induced by VML injury. Therefore, we are developing therapeutic strategies based on resolution-pharmacology that harnesses endogenous inflammation resolution mechanisms to limit tissue destruction and fibrosis while also stimulating repair and regeneration after VML.

Systemic studies of lipid mediators involved in actively resolving inflammation have uncovered essential signaling pathways that are activated in the initial phase of self-limited inflammation [135]. However, investigations of the metabolism of SPMs and their potential role in the pathogenesis and treatment after a traumatic injury, in this case VML, is unknown. We leveraged mass-spectrometry based lipidomics to measure the abundance of lipid mediators derived from AA, DHA, and EPA in a pre-clinical model of VML. Our findings are among the first liquid chromatography mass-spectrometry based lipidomic profiling analysis of SPMs in an established pre-clinical model of VML. Our results suggest an impairment in the ability of the local injury environment to produce SPMs after a VML injury. Furthermore, our results may indicate that there may be a metabolic difference between different types of skeletal muscle when it comes to abundance of SPMs at homeostasis. While these observed differences are intriguing, both models are consistent in revealing a deficiency in SPM biosynthesis following VML. A similar observation was found in the muscle of aged mice where the local injury environment of aged mice was characterized by the absence of downstream pro-resolving lipid mediators and impaired myofiber regeneration [49]. Conversely, in a model of acute muscle injury and functional regeneration the injury is characterized by a successful lipid mediator class switch that results in the production of downstream SPMs [106]. Taken together, these results motivated us to design a strategy to promote the lipid mediator switch that leads to the production of SPMs during inflammation. This strategy focused on promoting the initial activation of the local pro-resolving signaling pathways that would serve to then program the downstream inflammatory cascade to be self-limited rather than chronic. Our therapeutic platform is based on the hypothesis that releasing AT-RvD1 within the first 24 hours of the inflammatory injury will program the inflammatory cascade to resolve even after the absence of the external mediator. Our data show that we successfully promote the production and accumulation of SPMs at 72 hours post VML with AT-RvD1 treatment, which is beyond the time AT-RvD1 being released from the hydrogel. Our results demonstrate the activation of a broad set of metabolic pathways to promote the generation of different classes of SPM on the

DHA pathway and even on the separate AA and EPA pathways. Furthermore, given that the lipid mediator class switch from pro-inflammatory eicosanoids to SPMs is triggered via the accumulation of prostaglandins [135], the significant increase in total prostaglandins after AT-RvD1 treatment seen at day 3 post VML may be indicative of the initiation of this lipid mediator switch being promoted.

Classical ‘anti-inflammatory’ strategies to reduce chronic inflammation associated with VML have been proposed, but significant concerns persist about the undesired impairment of tissue regeneration [116, 136]. Our studies have shown that synthetic PEG-4MAL hydrogels that are able to encapsulate and locally deliver the SPM Aspirin-triggered (AT-RvD1) to shift the local immune cell milieu towards a pro-regenerative phenotype [118]. This biomaterial platform is uniquely advantageous for translational use in cases of disrupted structural tissue integrity. It can be injected directly into the tissue where it undergoes gelation under physiological conditions and firmly integrates with biological tissues due to the maleimide functional groups reacting with thiol groups present on the tissue [137]. While SPMs have been proposed to treat a wide range of inflammatory diseases [52, 105, 117, 118], there is limited research into using local delivery strategies to enhance the bioavailability and efficacy of SPM therapeutics [58, 59], which may be critical considering the hostile VML microenvironment and short-range interactions of lipid mediators [109]. Our results show that the local delivery of AT-RvD1 using this biomaterial platform has robust pro-resolving effects that are sustained throughout the regenerative process potentially eliminating the need for repeated dosing strategies often used.

We also performed unbiased flow cytometry-based trajectory analysis of VML immune profiles using SPADE, an analysis technique that reconstructs complex cellular hierarchies of immune cell transitions to reveal rare cell states. These results highlight AT-RvD1's ability to limit neutrophil infiltration after local delivery, but also to limit neutrophil polarization to a pro-inflammatory, aged phenotype. This aged neutrophil phenotype is known to have greater propensity to undergo NETosis which may contribute to pro-fibrotic responses after VML [138]. Notably, aged neutrophils in VML defects also displayed elevated expression of MPO, a critical component of NETs. The function of local AT-RvD1 to limit pro-inflammatory and pro-fibrotic cell polarization is also reflected in the shift in the macrophage population towards a pro-resolving and pro-regenerative M2 phenotype. This pro-regenerative shift in macrophage phenotype has been previously observed in acute muscle injuries treated with repeat IP injection of RvD1, with these pro-regenerative cellular phenotypes showing a greater propensity of synthesizing pro-resolving mediators in a muscle injury environment [52, 106]. By analyzing both the molecular and cellular mediators of inflammation, we demonstrate that this therapeutic platform promotes the resolution of inflammation at both the molecular and cellular level.

Our results suggest that molecular reprogramming of the inflammatory cascade with local pro-resolution cues during the onset of inflammation enhances the regenerative capacity of the skeletal muscle after VML injury. Delivery of AT-RvD1 from PEG-4MAL hydrogels specifically increases the pool of muscle progenitor cells – FAPs and MuSCs – that are essential to forming new ECM and muscle fibers, respectively, after a muscle injury. The direct signaling interaction of resolvins with MuSCs has been previously explored [51, 52]; however, their direct signaling interaction on FAPs is underexplored. We show that AT-RvD1 is able to directly influence the fate of FAP differentiation by decreasing their propensity for fibrotic differentiation. This further illustrates the important dual nature of AT-RvD1 to both act on immune cells to promote resolution but to also act on muscle progenitor cells to promote muscle regeneration and limit fibrosis.

The spinotrapezius muscle has the ability to be whole mounted and imaged throughout the full thickness of the muscle, a unique advantage of this pre-clinical VML model. We leveraged this feature of the model and used whole-mount IHC and SHG imaging to demonstrate the ability of our local therapeutic to significantly improve muscle healing after VML. The combination of these two imaging methods shows that AT-RvD1 hydrogels implanted into a VML injury results in near complete closure of the defect after 14 days and a compact muscle fiber structure with a mature and organized collagen network.

The results from this study show that there is a dysregulated lipid mediator response after VML injury that is improved via local AT-RvD1 delivery. This is reflected in the pro-regenerative shift in the immune cell infiltrate and in the significant improvement in muscle regeneration after VML injury with AT-RvD1 hydrogel treatment. However, a limitation in the study is the lack of parallel characterization of the effectiveness of the AT-RvD1 hydrogel treatment in the quadricep pre-clinical VML model that also allows for *in vivo* isometric force testing. Our results lay the groundwork for further characterization of this therapeutic and an analysis of functional muscle recovery after VML with AT-RvD1 hydrogel treatment is the focus of future studies.

4.4 Conclusion

Our work demonstrates the ability of utilizing biomaterial-mediated delivery of AT-RvD1 to locally resolve the persistent inflammation characterizing VML injuries. Specifically, PEG-4MAL hydrogels functionalized with VPM enzymatically degradable cross linker and RGD cell adhesive ligand are highly effective for local delivery of AT-RvD1. We show the local delivery of AT-RvD1 activates a broad range of metabolic pathways to significantly increase endogenous biosynthesis of other polyunsaturated fatty acid-derived specialized pro-resolving lipid mediators. Furthermore, this local pro-resolution strategy modulates the local immune cell environment to foster a pro-regenerative cellular milieu. This then results in a significantly improved muscle healing outcome after VML with near complete defect closure, compact regenerated fibers, and organized collagen fibers. This innovative platform could be further developed to support stem cell therapy for treating skeletal muscle injuries, especially given that it resolves the harsh inflammatory environment that often limits such therapies. These results highlight the translational potential of this platform for traumatic injuries and setup further development and scale-up of the biomaterial therapy for future functional studies.

4.5 Materials and Methods

4.5.1 Hydrogel Synthesis

Four-arm PEG macromer (10-kDa molecular weight) end functionalized with maleimide (>95% purity; Laysan Bio) at a final density of 4.5% (w/v) was used for all hydrogel formulations as described previously [119, 122]. PEG macromers were functionalized with RGD peptide

(GRGDSPC), cross-linked with the protease-degradable cysteine-flanked peptide VPM (GCRDVPMSMRGGDRCG) (AAPPTec) in 0.5 M MES buffer (pH 5.5). The final concentration of RGD was 1.0 mM. Gels were also loaded with 100ng of AT-RvD1 (4 µg/ml) (Cayman Chemical). The cross-linker concentration was adjusted to consume non-reacted maleimide groups remaining on PEG macromers. For hydrogels used in animal studies, all components were filtered through a spin column after pH measurements and kept under sterile conditions until injection into the animals and in situ polymerization.

4.5.2 Quadricep VML surgery

Surgical procedure performed as previously reported [139]. Briefly, the left hindlimb was prepped and sterilized. An incision was made above the quadriceps and either a 2mm (for sub-critical VML analysis) or a 3 mm (for critical VML analysis) biopsy punch (VWR, 21909-136) was used to make a full-thickness muscle defect. The skin was closed and animals (Male C57/BL6 mice) were allowed to heal for either 3 or 7 days before euthanasia by CO2 inhalation.

4.5.3 Spinotrapezius surgery and hydrogel implantation

All animal procedures were conducted according to protocols approved by Georgia Institute of Technology Institutional Animal Care and Use Committee. Male C57BL/6J mice (8-12 weeks old, Jackson Laboratory) were used for all animal studies. A 2 mm-diameter full thickness defect in the spinotrapezius muscle was created as previously described [140]. Briefly, a longitudinal 1-inch incision was made just after the bony prominence of the shoulder blade. The overlying fascia was dissected away and the spinotrapezius muscle was identified. The edge of the spinotrapezius was reflected and positioned against a sterile piece of wood and a full-thickness defect was made through the muscle using a 2mm biopsy punch. Hydrogel components were mixed, loaded into a syringe, and injected in the defect area. The skin incision was closed with wound clips.

4.5.4 Mass spectrometry quantification of pro-inflammatory eicosanoids and SPMs from quadricep muscle tissue.

Samples of muscle tissue (Quadricep) were subjected to solid phase extraction (SPE) followed by a targeted liquid chromatography-tandem mass spectrometry (LC-MS/MS) analysis. Samples were stored at −80°C prior to extraction. Deuterated internal standards including d5-RvD2, d4-LTB4, d8-5-HETE, d4-PGE2, d5-MaR1, and d5-LXA4 (Cayman Chemical) were used to assess extraction recovery and quantification. Mechanically digested samples were centrifuged (3,000 rpm) and supernatants were then subjected to SPE and LC-MS/MS analysis, in part as described previously [49]. In short, acidified water (pH 3.5 with HCl) was added to samples immediately prior to SPE using C18 column chromatography. Lipid mediators were eluted in the methyl formate fractions, the solvent was evaporated under a gentle stream of N2 gas and the samples were then resuspended in methanol:water (50:50). Samples were then injected using a high-performance liquid chromatograph (HPLC, Shimadzu) equipped with a reverse-phase C18 column (100 mm x 4.6 mm x 2.7 mm; Agilent Technologies) held at 50°C and coupled to a QTrap5500 mass spectrometer (AB Sciex) operating in negative ionization mode and using Analyst software (v1.7). A gradient of methanol-water-acetic acid ranging from 50:50:0.01 (v/v/v) to 98:2:0.01 (v/v/v) was used at a constant flow rate of 0.5ml/min. Individual lipid mediators were identified using specific multiple reaction monitoring (MRM) transitions and information-dependent acquisition enhanced product ion scanning. Identification was based on matching retention time with authentic standards (Cayman Chemical) run in parallel using specific MRM transitions, as well matching of MS/MS fragmentation ions in selected samples using Sciex OS-Q (v1.7).

Quantitation of mediators was then carried out for peaks reaching a signal to noise ratio of least 5, followed by accounting for the extraction recovery of the deuterated internal standards and by extrapolation to calibration curves of external standards for each individual mediator. The data were normalized to muscle tissue weight. The limit of quantification was established for each mediator by determining the lowest amount that could be quantified in replicate injections with a coefficient of variation of less than 20%.

4.5.5 Mass spectrometry quantification of pro-inflammatory eicosanoids and SPMs from spinotrapezius muscle tissue.

Excised spinotrapezius muscle was homogenized using a glass homogenizer with ice cold PBS using a bead homogenizer. Eicosanoids and SPMs were selectively extracted from the homogenized samples by SPE to account for their low concentrations in comparison to lipid species of higher abundance. For this, samples were extracted using an automated C18 SPE manifold (Biotage Extrahera, Uppsala, Sweden). Samples were prepared by depositing homogenized samples on the SPE plate, the sample was rinsed with 800 µL water, followed by 800 µl hexane. The oxylipins were then eluted off from the SPE column with 400 µL methyl formate. The recovered oxylipin fraction was then dried under N2 and subsequently reconstituted in methanol to be analyzed by LC/MS. Extracted lipids were resolved using an Agilent Infinity II/6495c LC-MS/MS system. To quantify the SPMs in extract, 10 µl sample was injected onto an Accucore C18 column (100 x 4.6, Thermo, Waltham, MA) and resolved on a 16-minute gradient using water as Solvent A and acetonitrile as Solvent B, both contain 0.1% formic acid. The column was heated to 50°C in a temperature-controlled column chamber and 0.5mL/min flow rate was used for analysis. Eluted oxylipins were analyzed by Agilent 6495c triple quadrupole mass spectrometer. Instrument parameters (reported below) were optimized using external analytical grade standards and were held consistent over the course of analysis. Oxylipins were analyzed in the negative ion mode using a multiple reaction monitored (MRM) based method. For this, the mass of the target lipid and a characteristic fragment were targeted for detection. Oxylipins were quantified using MassHunter software, where the area under the curve of each identified lipid is calibrated against an external calibration curve. To create the curve, analytical grade standards in the linear range of 0.1nM-10nM are created for each standard. The lower limits of detection and upper limits of detection are determined, plotting concentration versus area under the curve. The slope of the linear regression equation is used for calibration of the corresponding analyte. Instrumental parameters were optimized this lipid class using internal standards and were held constant during the course of the experiment. For each standard, serial dilutions were prepared that cover a broad range of concentrations, typically in the range of 0.01 µM to 1.0 mM, to determine the upper and lower limits of detection (LLOD). It should be noted that the LLOD is at least 10 times the noise level.

4.5.6 Tissue Harvest and Flow Cytometry

To collect tissue for flow cytometry analysis, mice were euthanized via CO_2 asphyxiation. For analysis of cell composition in spinotrapezius muscles, a 6 mm biopsy punch of muscle tissue centered on the defect was taken, weighed, and digested with 5,500 U/mL collagenase II and 2.5 U/mL Dispase II for 1.5 h in a shaking 37°C water bath. The digested muscles were filtered through a cell strainer to obtain a single cell suspension. Single-cell suspensions were stained for live cells using either Zombie Green or Zombie Violet (BioLegend) dyes in cell-culture grade PBS per manufacturer instructions. Cells were then stained with cell phenotyping antibodies in a 1:1 volume ratio of 3% FBS and Brilliant Stain Buffer (BD Biosciences) according to standard procedures and analyzed on a FACS Aria III flow cytometer (BD Biosciences). The following antibodies were used for cell phenotyping: PE-Cy5-conjugated anti-CD29 (BioLegend), APC-conjugated anti-CD31 (BioLegend), BV800-conjugated Sca-1 (BioLegend), PerCP-Cy5.5-conjugated anti-CXCR4 (BioLegend), BV510-conjugated anti-Ly6C (BioLegend), PE-Cy7-conjugated anti-CD206, PE-conjugated anti-MerTK (eBioscience), BV711-conjugated anti-CD64 (BioLegend), BV421-conjugated anti-CD11b (BioLegend), APC-Cy7 conjugated anti-Ly6G (BioLegend), PE-Cy5-conjugated anti-CD11b (BioLegend), PE-conjugated anti-CD49d (BioLegend), APC-conjugated anti-VEGFR1 (BioLegend), BV605-conjugated anti-CXCR4 (BioLegend), BV711-conjugated anti-CD62L (BioLegend), PE-Cy5 conjugated anti-CD29 (BioLegend), PerCP-Cy5.5-conjugated anti-CXCR4 (BioLegend), and APC-conjugated Lineage antibody cocktail containing antibodies for mouse CD3e, CD11b, CD45R/B220, Ly-76, Ly6G, and Ly6C (BD Pharmingen), PE-Cy7-ocnjugated anti-CXCR2 (BioLegend), PerCP-Cy5.5-conjugated anti-CD47 (BioLegend), FITC-conjugated anti-MPO (BioLegend). Additionally, 30 μL of AccuCheck Counting Beads (Invitrogen) were added per sample for absolute quantification of cell populations. Single, live cells were selected in FlowJo software for subsequent analysis. Myeloid cells were gated as CD11b^{+}. Unless indicated otherwise, Neutrophils were gated as CD11b^{+} Ly6G^{+} cells Macrophages were gated as CD11b^{+} CD64^{+} MerTK^{+} cells. Monocytes were gated as CD11b^{+} CD64+ MerTK^{-} cells.

4.5.7 High Dimensional Analysis of flow cytometry data

SPADE is an unsupervised trajectory analysis tool that was designed to map heterogeneous single-cell populations into two dimensions on the basis of similarities across defined markers [141]. SPADE creates a tree structure where nodes represent clusters of cells with similar marker expression. The size and color of each node are relative to the number of cells present and the median marker expression. SPADE was performed in MATLAB, and the source code is available at http://pengqiu.gatech.edu/software/SPADE/. SPADE automatically constructs the tree by performing density-dependent downsampling, cell clustering, linking clusters with a minimum spanning-tree algorithm, and upsampling based on user input. The SPADE tree was generated by exporting uncompensated pre-gated live, single-cell, CD11b$^+$CD64$^+$MerTK$^+$ macrophages, pre-gated live, single-cell, CD11b$^+$Ly6G$^+$ neutrophils, pre-gated live, single-cell, CD11b$^+$CD64$^+$MerTK$^-$ monocytes, pre-gated live, single-cell, Lin$^-$ cells. The markers and/or features used to build the neutrophil SPADE tree were SSC, FSC, CD11b, Ly6G, CD49d, CXCR4, CD62L, CXCR2, CD47, MPO. With this SPADE tree, clusters consistent with the aged neutrophil phenotype were identified. The markers and/or features used to build the macrophage and monocyte SPADE tree were SSC, FSC, CD11b, CD64, MerTK, CD206, Ly6C. With this SPADE tree, clusters consistent with the inflammatory and anti-inflammatory monocyte and macrophage phenotype were identified. The markers and/or features used to build the Lin- SPADE tree were SSC, FSC, Lineage, CD31, CD29, Sca-1, CXCR4. With this SPADE tree, clusters consistent with the MuSC and FAP phenotype were identified. The multiple comparison tool in SPADE was used to identify significantly different populations between treatment groups. The following SPADE parameters were used: apply compensation matrix in FCS header, arcsinh transformation with cofactor of 150, neighborhood size of 5, local density approximation factor of 1.5, maximum allowable cells in pooled downsampled data of 50,000, target density of 20,000 cells remaining, and number of desired clusters of 60.

4.5.8 Tissue whole mount immunohistochemistry and confocal imaging

Mice were euthanized 7 days after surgery via CO_2 asphyxiation. Post-euthanasia, mouse vasculature was perfused with warm saline followed by 4% PFA until tissues were fixed. The entire spinotrapezius muscle was explanted and permeabilized overnight with 0.2% saponin, then blocked overnight in 10% mouse serum. For immunofluorescence staining, tissues were incubated at 4°C overnight in a solution containing 0.1% saponin, 5% mouse serum, 0.5% bovine serum albumin, and the following conjugated fluorescent antibodies: Alexa Fluor 650 anti-desmin (1:200 dilution, Abcam), Alexa Fluor 650 anti-CD68 (1:200 dilution, Bio-Rad), Alexa Fluor 488 anti-CD206 dye (1:200 dilution, BioLegend). Following immunostaining, tissues were washed four times for 30 min each in 0.2% saponin for the first two washes, 0.1% saponin for the third wash, and PBS for the final wash, and then mounted in 50/50 glycerol/PBS. Mounted samples were imaged on a Zeiss LSM 710 NLO confocal microscope (Objective: 20X / 0.8 NA Plan-Apochromat). Cropped images of 332 × 332 μm at 20X magnification in the injury area were taken for image analysis. Circularity measurements were measured via ImageJ.

4.5.9 Second harmonic generation (SHG) imaging and analysis

Second harmonic generation (SHG) imaging of whole mount spinotrapezius muscles was performed using a home-built multiphoton microscope, with an optical setup similar to what we have reported previously [142]. Briefly, it has a Ti:Sapphire femtosecond pulsed laser tuned to 780 nm, with the power of the beam adjusted by a half wave retarder and polarizing beam splitter, then rapidly modulated by a Pockels cell attenuator and scanned over the specimen. The back-detected emission light is sent to a photon multiplier tube with a bandpass filter of 390/18 to capture SHG images of whole mount spinotrapezius muscle. SHG images (512 x 512 pixels) of spinotrapezius muscle structure were collected with linearly polarized excitation using a half-waveplate sequentially rotated to 0º, 90º, and 180º to enhance contrast for evaluating muscle fiber orientation. For all samples, the edges of each volumetric muscle loss defect area were imaged to create 3 polarized images from similar regions of the defect areas. We used a polarization state analyzer to measure the Stokes parameters for each excitation angle and correct for polarization distortion in the focus. We analyzed SHG images in the Fourier space, which represents the periodicity and angle of structures in the samples. We then used an angular Fourier filter (AFF) developed previously [126] to analyze the image content across different orientation angles, where image content that is spread across multiple angles suggests less organized tissue. Because muscle fibers have very directionally organized structures in their healthy state, this metric can assess the state of the tissue during regenerative processes.

4.5.10 Statistical Analysis

Data is presented as means ± SEM unless otherwise noted. Statistical tests were conducted using GraphPad Prism 8. Two-tailed unpaired *t*-tests were performed for two-group comparisons. For comparison of more than two groups, one-way ANOVA with Tukey's *posthoc test* used for multiple comparisons. For grouped analyses, two-way ANOVA with Sidak's *posthoc* test was used for multiple comparisons. Significance levels were set at *$p<0.05$, **$p<0.01$, ***$p<0.001$, ****$p<0.0001$. Investigators were blinded to the experimental groups when analyzing the data. Differences in sample sizes between groups are due to instrument error causing no detection in cells or metabolites; however, these studies remain adequately powered for statistical analysis.

CHAPTER 5. PRO-RESOLVING HYDROGELS INDUCE A PRO-REGENERATIVE CELLULAR MICROENVIRONMENT AND ENHANCE FUNCTIONAL MUSCLE REGENERATION AFTER VML.

5.1 Introduction

The pre-clinical quadriceps VML model has been extensively characterized to find a critical injury threshold above which the clinical VML hallmarks occur: fibrosis and fatty infiltration, chronic inflammation, lack of myofiber bridging across the defect and impaired contraction [143]. This critical VML injury presents a persistence of collagen fibrosis and fatty infiltrate in the defect environment and between regenerating myofibers [143] characteristic of skeletal muscle trauma [9]. In addition to this fibrotic phenotype, the critically sized defect displayed the persistent inflammation seen after VML injury. Specifically, the sustained macrophage presence sets the VML injury apart from other acute injury types with similarities to chronic muscle disorders [144, 145]. Furthermore, in this critical VML injury there is no evidence of reinnervation of the myofibers in the defect region up to 28 days post injury leading to a significant deficit in force production [143]. One specific advantage of the model, compared to the spinotrapezius VML model, is the ability to test the recovery of *in vivo* muscle function recovery with treatment after VML. This is the ultimate goal of any therapeutic platform in a traumatic muscle injury since the persistent functional deficits are the root cause of the severe clinical burden present with such injuries. Our hypothesis is that the successful resolution of inflammation induced via local AT-RvD1 delivery will lead to an increase in functional muscle regeneration.

In this chapter, we explore the pro-inflammatory and lipid mediator response after critical quadricep VML injury at various timepoints (uninjured, days 1, 3, 5, 7 and 14) post VML. This allows us to establish the dysregulation of the pro-resolving lipid mediator response across two weeks after VML injury. We then analyze the cellular infiltrates after VML injury using single-spectral cell flow cytometry to show a pathological persistence in macrophage subtypes that are decreased with AT-RvD1 delivery. Furthermore, we use H&E and IHC analysis of quadricep cross sections at 14 days post VML to analyze metrics of increased muscle regeneration with AT-RvD1 treatment. This induced pro-regenerative microenvironment and early improvement in muscle regeneration via local AT-RvD1 delivery is able to recover muscle function so as to perform similar to healthy controls in the aggressive quadriceps pre-clinical VML injury model. We test this functional recovery via *in vivo* isometric force testing. This functional result is, to our knowledge, the most robust functional recovery seen after VML injury in this model.

5.2 Results

5.2.1 Liquid chromatography-tandem mass spectrometry analysis at days 1, 3, 7, 10 and 14 post VML reveals a robust pro-inflammatory eicosanoid response without a concomitant pro-resolving lipid response.

5.2.1.1 Analysis of the AA metabolome reveals a robust but transitory inflammatory lipid mediator response after VML injury.

Lipid mediators derived from Arachidonic Acid (AA) constitute most pro-inflammatory lipid mediators (prostaglandins, thromboxane and leukotrienes) involved in initiating and potentiating pro-inflammatory pathways. Additionally, the AA-derived Lipoxin family of SPMs, in addition to DHA-derived SPMS, are important in promoting the initial stages of pro-resolution. In order to investigate the response of these lipid mediators after traumatic injury, we measured the concentration of these species via LC/MS-MS at various timepoints after critical VML injury of the murine quadriceps muscle. Broadly, in the pro-inflammatory mediator compartment, we see a spike in the production and accumulation of these lipids at 1 day post VML that quickly returns to baseline thereafter (Fig 27A-D). Specifically, Prostaglandin E2 (PGE2) and Thromboxane B2 (TXB2) increase significantly compared to uninjured quadriceps muscle at day 1 post VML and

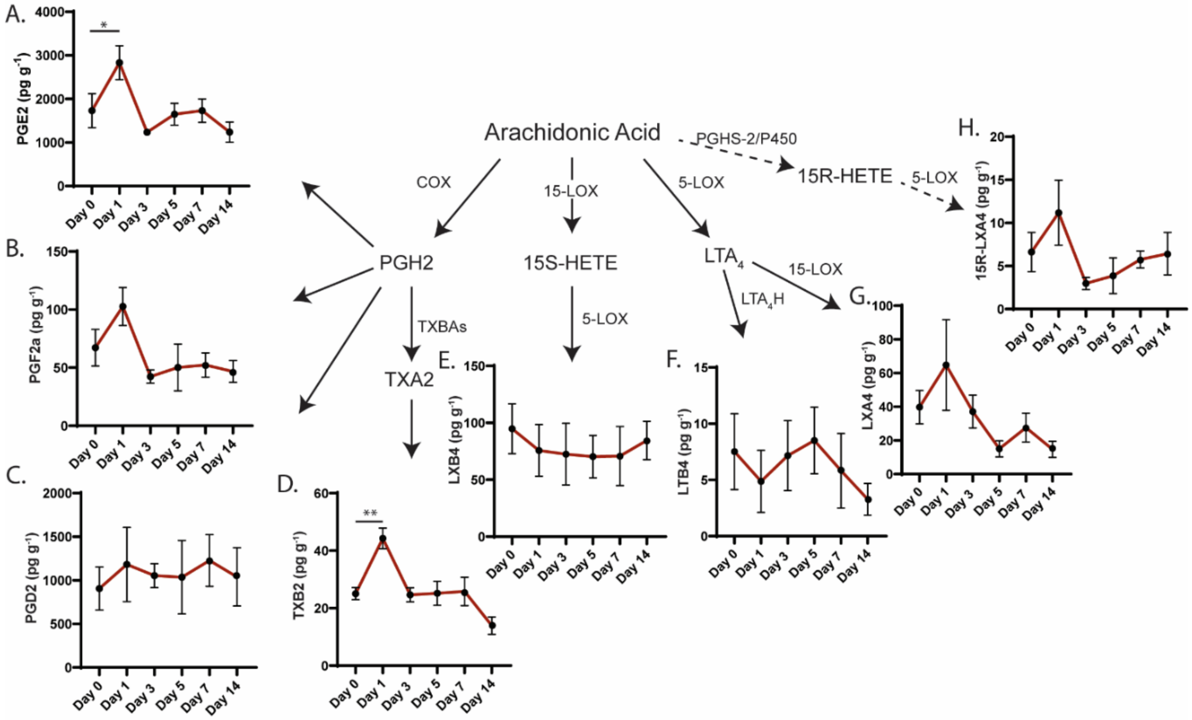

Figure 27. AA-derived lipid mediator analysis.
Quantification via LC-MA/MS of lipid mediators derived from AA of uninjured (day 0) quadriceps and days 1, 3, 5, 7 and 14 post critical VML injury (A-H). Statistical analyses were performed using a one-way analysis of variance (ANOVA) with Dunnet's multiple comparisons; *P < 0.05 and **P < 0.01; n =5 animals per group.

then are returned to baseline, uninjured concentration by 3 days post VML (Fig 27A and D). The three pro-resolving mediators detected that are derived from AA, Lipoxin B4 (LXB4), Lipoxin A4 (LXA4) and 15R-LXA4, show a decreasing trend during the inflammatory cascade after VML (Fig. 27E, G and H).

We also observe at sustained spike in the concentration of AA after critical VML injury (Fig. 28A). This accumulation of AA is sustained and significantly elevated at days 3 and 7 post

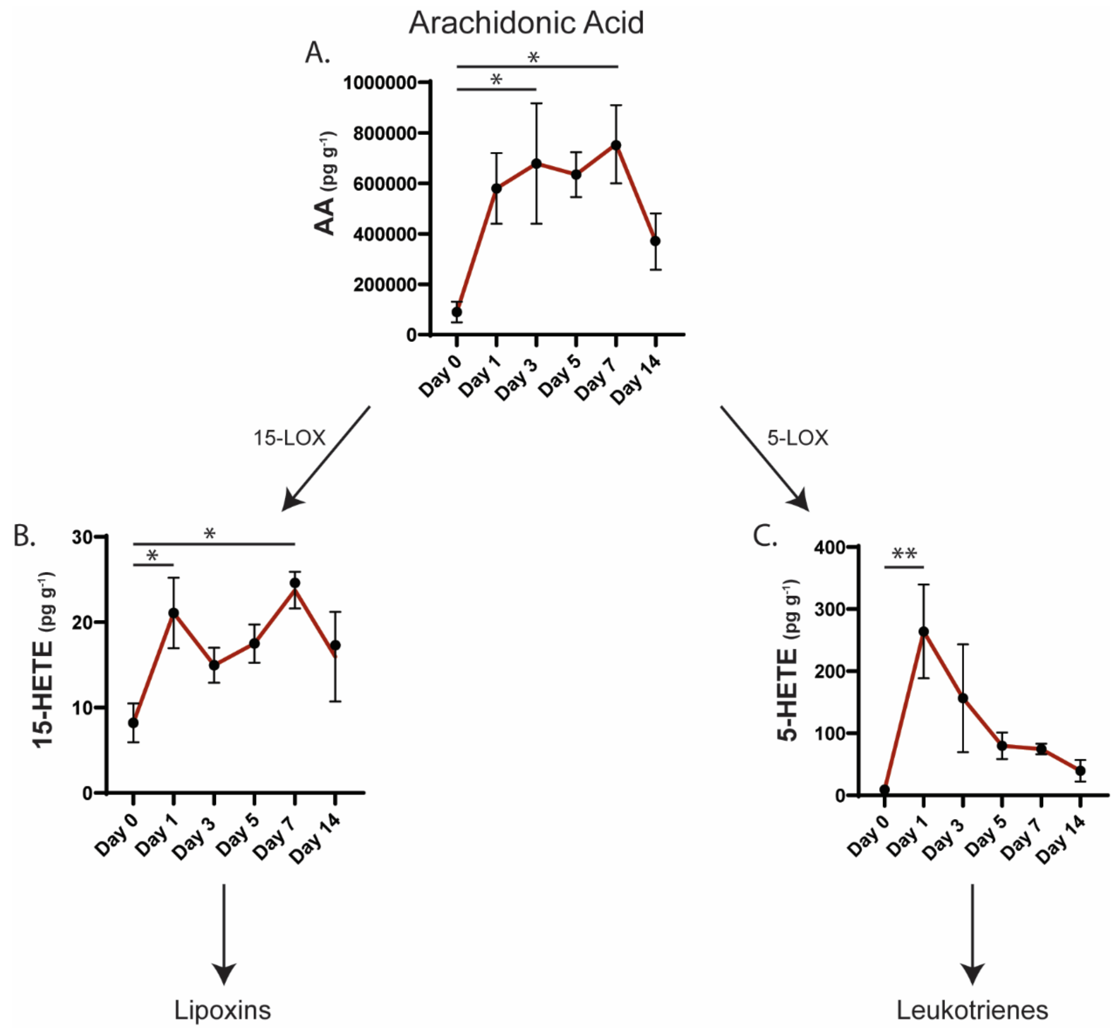

Figure 28. Monohydroxy pathway intermediates of AA metabolism.
The concentration of Arachidonic Acid (A), 15-HETE (B) and 5-HETE (C) are measured via LC-MS/MS. 15-HETE and 5-HETE are monohydroxy intermediates and serve as pathway markers for the pro-resolving lipoxins and pro-inflammatory leukotrienes, respectively. Statistical analyses were performed using a one-way analysis of variance (ANOVA) with Dunnet's multiple comparisons: *$P < 0.05$ and **$P < 0.01$; n =5 animals per group.

VML then trends toward baseline levels at day 14 post VML (Fig 28A). Although the concentration of lipoxins does not increase after VML (Fig. 27), the monohydroxy pathway intermediate in the biosynthesis of lipoxins, 15-HETE, does accumulate and remains significantly elevated at days 1 and 7 post VML compared to uninjured quadricep muscle (Fig. 28B). Like COX-derived prostaglandins, we see a transient increase in the 5-LOX-derived pathway intermediate of pro-inflammatory leukotrienes with a significant increase in concentration at day 1 post VML before returning to baseline levels (Fig 28C). Furthermore, the relative magnitude of the concentrations of the two monohydroxy pathway intermediates suggest a bias of AA conversion toward the pro-inflammatory 5-LOX pathway (Fig 28B and C).

5.2.1.2 Analysis of the DHA and EPA metabolome shows that SPMs fail to accumulate after VML injury.

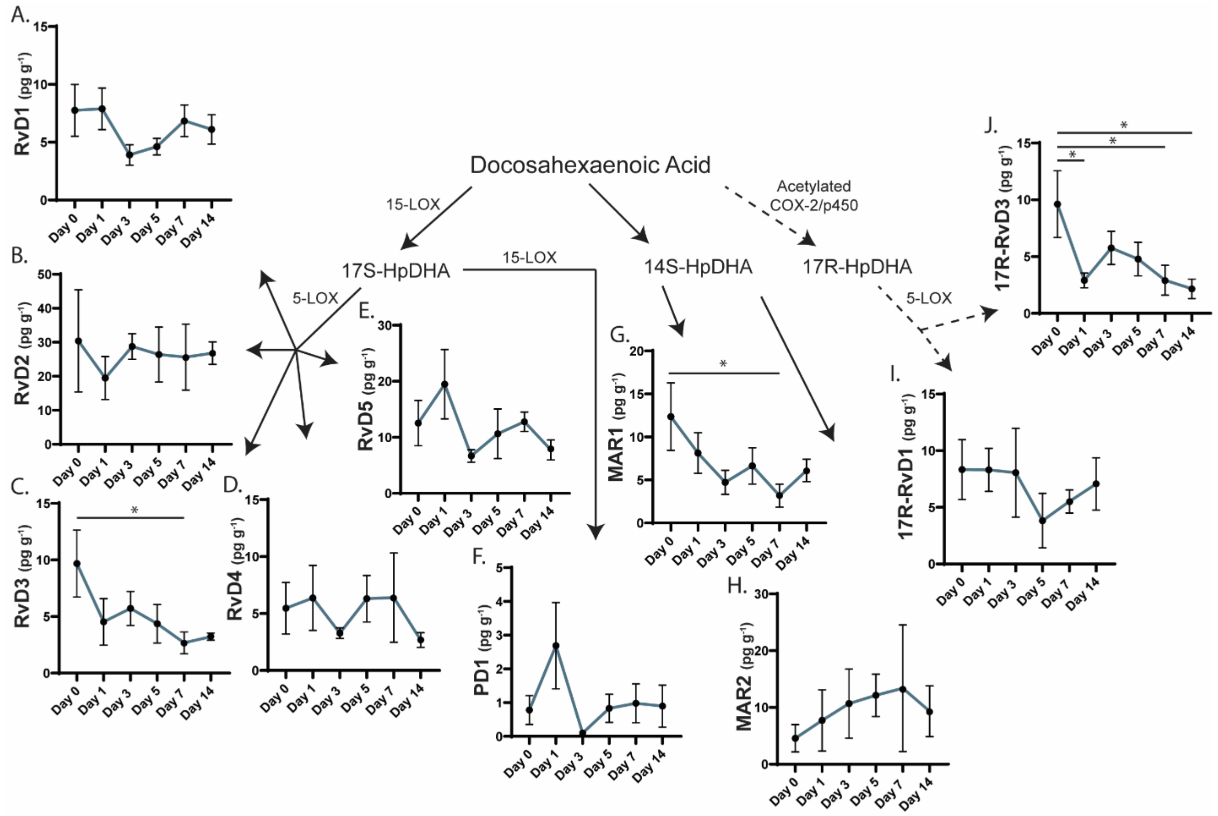

Figure 29. DHA-derived lipid mediator analysis.
Quantification via LC-MA/MS of lipid mediators derived from DHA of uninjured (day 0) quadriceps and days 1, 3, 5, 7 and 14 post critical VML injury (A-H). Statistical analyses were performed using a one-way analysis of variance (ANOVA) with Dunnet's multiple comparisons; *P < 0.05 and **P < 0.01; n =5 animals per group.

Lipid mediators derived from Docosahexaenoic Acid (DHA) constitute the majority of pro-resolving lipid mediators (D-series resolvins, protectins, maresins, 17-R D-series resolvins) that potentiate pro-resolving pathways. Having seen an increased but transitory activation of pro-inflammatory lipid mediators derived from AA (Fig. 27), we investigated whether this is followed by a similar response in SPMs (Fig. 29). Generally, we do not see any appreciable increase in the concentration of SPMs after critical VML injury but rather an overall downward trend in the

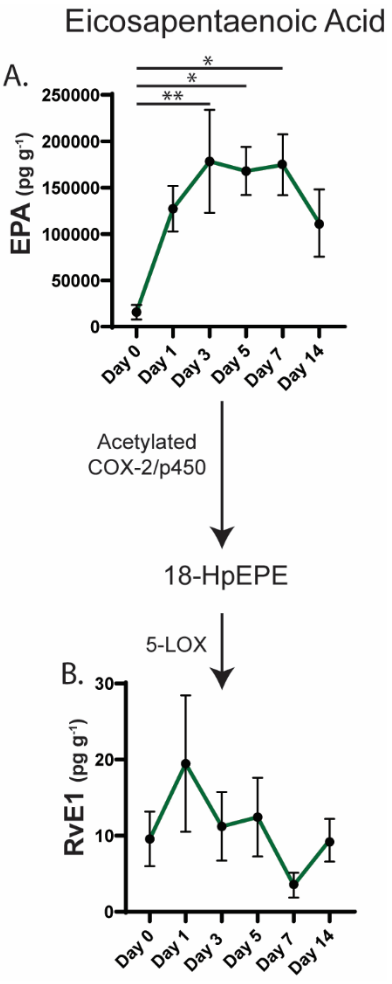

Figure 30. EPA-derived lipid mediator analysis.
Quantification via LC-MA/MS of lipid mediators derived from EPA of uninjured (day 0) quadriceps and days 1, 3, 5, 7 and 14 post critical VML injury (A-B). Statistical analyses were performed using a one-way analysis of variance (ANOVA) with Dunnet's multiple comparisons; $^*P < 0.05$ and $^{**}P < 0.01$; n =5 animals per group.

concentration of SPMs (Fig. 29). The concentration of RvD3 and MAR1 at day 7 post VML and of 17R-RvD3 sustained at days 1-, 7- and 14-days post VML significantly decreases (Fig. 29C, G and J). Furthermore, while we see a significant increase in EPA at days 3 5 and 7 post VML injury, the downstream SPM RvE1 remains unchanged after injury (Fig 30A and B).

We observe an initial spike in the concentration of DHA, the substrate for SPMs, that is sustained at days 1 and 3 post VML injury (Fig. 31A). 17-HDHA, a monohydroxy intermediate marker of 15-LOX acting on DHA, shows a downward trend in concentration throughout the inflammatory cascade after VML injury (Fig. 31B). This is a marker of the first step in the biosynthesis of both resolvins and protectins, the concentration of which also decrease after VML injury (Fig. 29). 14-HDHA is a monohydroxy intermediate pathway marker of 12-LOX acting on DHA, the first step in the biosynthesis of maresins. Maresin concentration was seen to significantly decrease after VML injury (Fig 22G); however, the concentration of 14-HDHA significantly increases at day 1 post VML before returning to baseline levels (Fig. 31C). This may indicate that 12-LOX acting on DHA is not the rate limiting step in the biosynthesis of maresins.

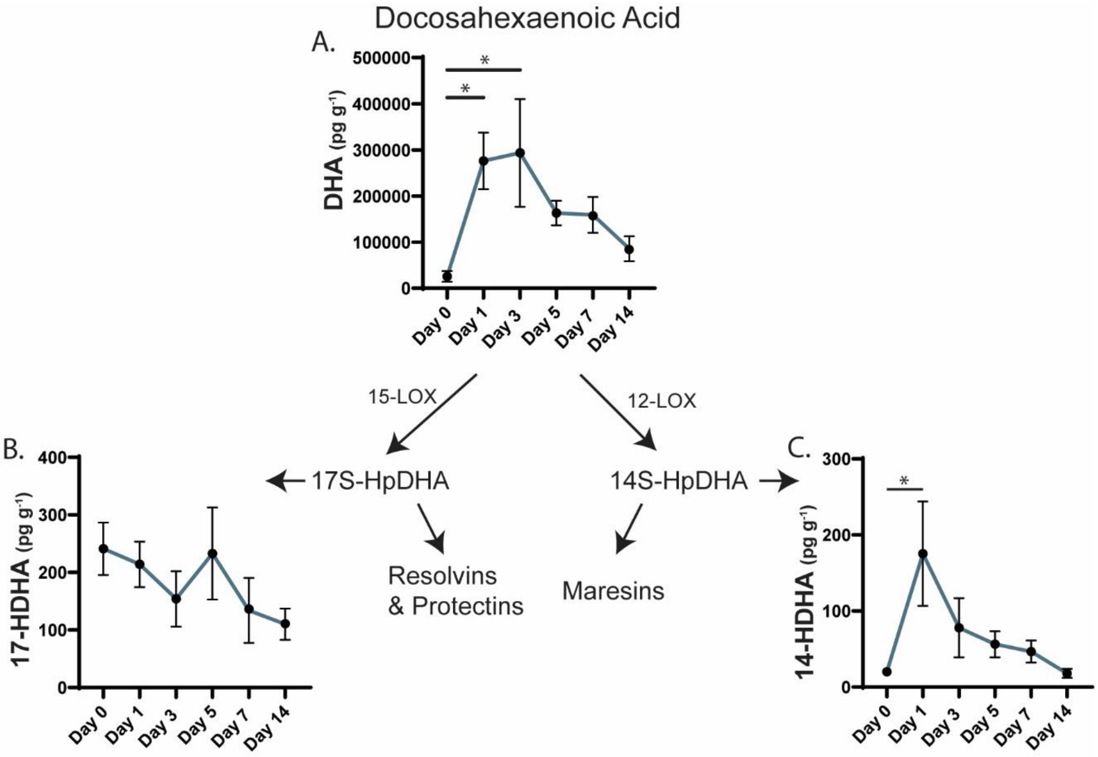

Figure 31. Monohydroxy pathway intermediates of AA metabolism.
The concentration of Arachidonic Acid (A), 15-HETE (B) and 5-HETE (C) are measured via LC-MS/MS. 15-HETE and 5-HETE are monohydroxy intermediates and serve as pathway markers for the pro-resolving lipoxins and pro-inflammatory leukotrienes, respectively. Statistical analyses were performed using a one-way analysis of variance (ANOVA) with Dunnet’s multiple comparisons; *P < 0.05 and **P < 0.01; n =5 animals per group.

5.2.1.3 <u>The overall Lipid mediator response after VML injury is characterized by a production of inflammatory eicosanoids and a consumption of SPMs.</u>

A self-resolving inflammatory response is marked by a switch from a production of pro-inflammatory lipid mediators to SPMs. This switch is termed the lipid mediator switch and is vital in the successful resolution of inflammation. We investigated whether this switch occurs after critical VML injury by looking at the total pro-inflammatory and pro-resolving lipid mediators produced at days 1, 3, 5, 7 and 14 post injury. The pro-inflammatory lipid mediators significantly increase at day 1 post injury and then return to baseline and day 3 post injury and remain there through day 14 post injury (Fig. 32). With this pattern, we would expect an increase in SPMs to begin to occur as the pro-inflammatory mediators decrease. However, after critical VML injury

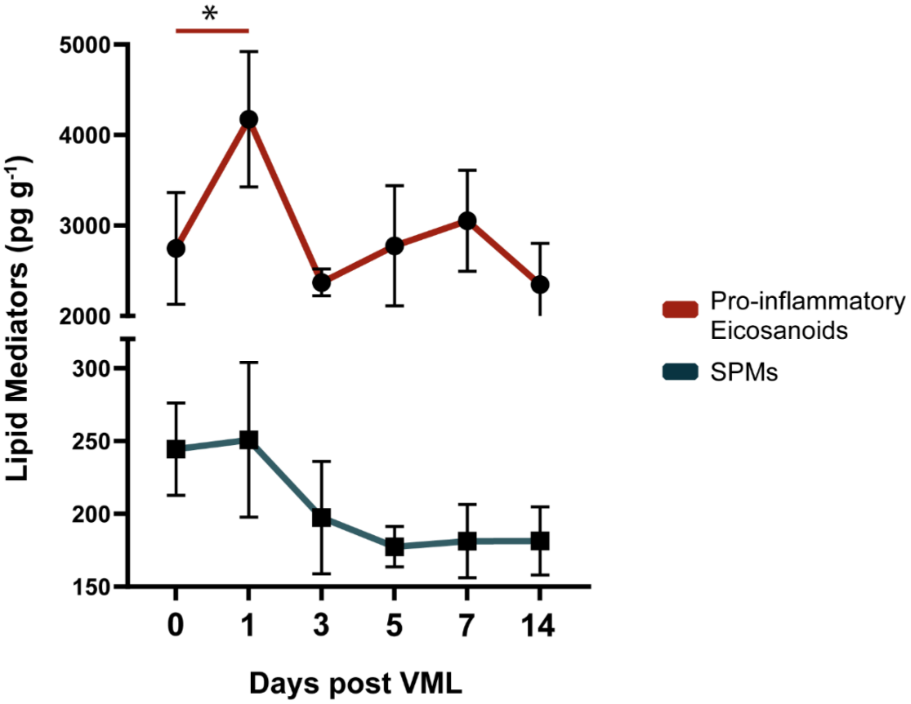

Figure 32. Overall lipid mediator response after critical VML injury.
Total concentration of pro-inflammatory mediators and SPMs are shown for uninjured (day 0) quadriceps muscle and days 1, 3, 5, 7, and 14 post VML. Statistical analyses were performed using a one-way analysis of variance (ANOVA) with Dunnet's multiple comparisons; $^*P < 0.05$ and $^{**}P < 0.01$; n =5 animals per group.

SPMs do not increase as compared to baseline, uninjured levels. Rather, they slowly begin to decrease after injury and remain low through day 14 post VML injury (Fig. 32). Furthermore, by calculating the ratio of pro-inflammatory to pro-resolving lipid mediators one can track the time the lipid mediator switch occurs as that is when this ratio would significantly decrease (owing to the drop in pro-inflammatory mediators and increase in SPMs). After critical VML injury this significant drop in the ratio does not occur up to 14 days post injury but rather stays relatively stable (Fig. 33).

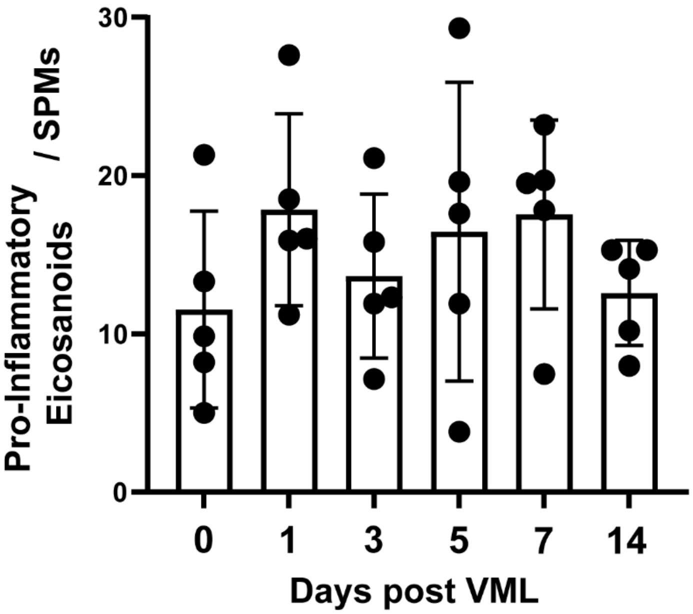

Figure 33. Ratio of pro-inflammatory to pro-resolving lipid mediator switch indicates the absence of a lipid mediator switch.

5.2.2 Pseudotime analysis identifies distinct macrophage subsets that persist and are dysregulated following critical VML injury.

All CD11b$^+$CD64$^+$MerTK$^+$ macrophages, from uninjured and injured quadriceps (at days 1, 3, and 7 post injury) were used to generate a SPADE dendrogram (Figure 34A). SPADE clustered the macrophages into nodes ordered along 4 marked trajectories, each color-coded, characterized by the surface marker expression of each node. Most macrophages present within the injured muscle at day 1 are clustered within nodes of the initial M1-like trajectory, characterized by its Ly6C^{High} CD206^{Low} expression profile. Along the pseudotime trajectory (grey arrows), the ordered nodes split into 3 separate branches: an unpolarized (Ly6C^{Low} CD206^{Low}) trajectory, an M2-like (Ly6C^{Low} CD206^{High}) trajectory, and a 'hybrid' (Ly6C^{High} CD206^{High}) macrophage trajectory (Figure 34A). Quantitative analysis of flow cytometry profiles exported from SPADE reveals increases in the concentrations of M1 and unpolarized macrophages between injury sizes at multiple timepoints. M2 macrophages and hybrid macrophages were significantly elevated at 7 days post injury (Figure 34B). Considering the deficient production of pro-resolving lipid mediators after critical VML, persistent M2-like macrophages are likely sources of pro-fibrotic cytokine production, as has been previously seen in models of tissue and organ fibrosis [20].

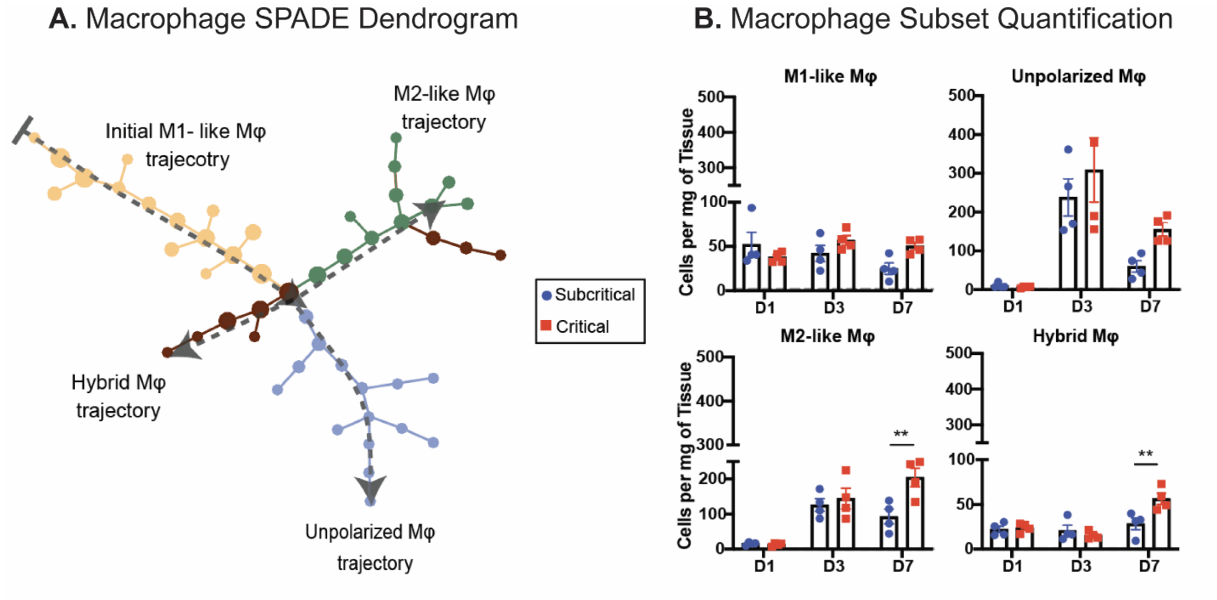

Figure 34. SPADE identifies unique macrophage subsets that persist after non-healing VML injury.

SPADE dendrogram generated from all CD11b+CD64+MerTK+ macrophages isolated from quadriceps muscle of mice which were uninjured or those which received a subcritical or critically sized injury (at days 1, 3, and 7 post injury). (A) Macrophage SPADE dendrogram annotated based on CD206 and Ly6C expression to designate nodes to a M1-like, M2-like, unpolarized, or hybrid macrophage phenotype. Gray arrow indicates general movement over time following injury. (B) Quantification of macrophage subsets (per mg of tissue) within quadriceps muscle at each timepoint post injury. Data presented as mean ± S.E.M. Statistical analyses performed include two-way ANOVA with Sidak test for multiple comparisons between injury sizes at each timepoint. **p<0.01. n=4 animals per experimental group. D1: day 1, D3: day 3, D7: day 7, Mφ: macrophage.

5.2.3 *In a quadriceps critical VML pre-clinical model local AT-RvD1 modulates infiltrating immune cell dynamics.*

5.2.3.1 Design of a high-dimensional spectral flow cytometry panel for immune cell and muscle progenitor cell identification.

Spectral flow cytometry differs from conventional flow cytometry in that it detects the entire spectral signal of fluorophores from multiple lasers [146]. This enables the individual resolution of fluorophores with similar emission spectra and increases the number of distinguishable markers in a multicolor panel. By expanding the number of markers included in the panel a larger number of cell types is able to be identified in a single experiment which is critical to assessing the infiltration of highly heterogenous immune types after severe muscle trauma.

Table 1. List of spectral flow cytometry markers and their conjugated fluorophores.

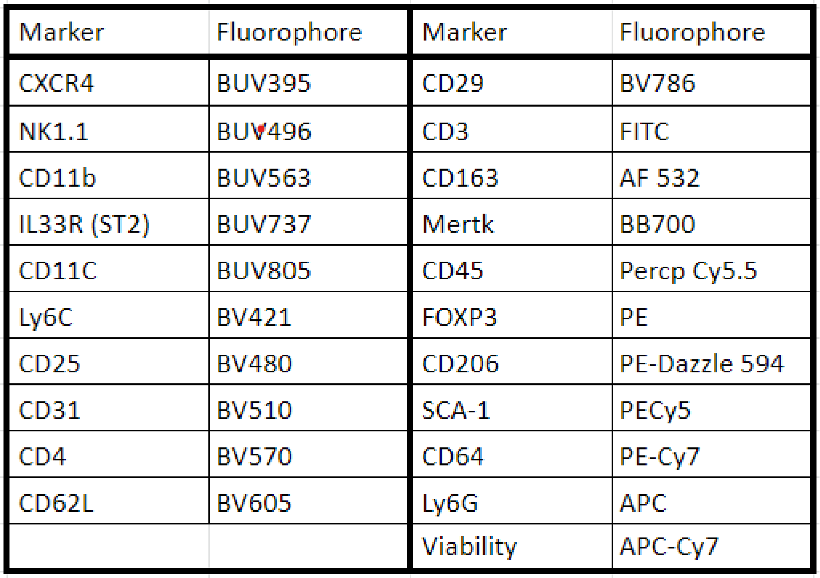

Marker	Fluorophore	Marker	Fluorophore
CXCR4	BUV395	CD29	BV786
NK1.1	BUV496	CD3	FITC
CD11b	BUV563	CD163	AF 532
IL33R (ST2)	BUV737	Mertk	BB700
CD11C	BUV805	CD45	Percp Cy5.5
Ly6C	BV421	FOXP3	PE
CD25	BV480	CD206	PE-Dazzle 594
CD31	BV510	SCA-1	PECy5
CD4	BV570	CD64	PE-Cy7
CD62L	BV605	Ly6G	APC
		Viability	APC-Cy7

While this technology allows for up to 30 (or more) markers in one panel, careful optimization is needed to design a panel of 20+ markers. In order to explore the potential effects of AT-RvD1 on the local muscle cell environment after VML with greater depth and throughput, we optimized a panel with 21 markers (Table 1.). This panel is strategically designed to identify and quantify the main immune cells present after muscle injury: neutrophils, monocytes, macrophages, dendritic cells, natural killer cells, and T-Cells. Furthermore, it identifies subsets within these parent cells: aged neutrophils (CD62L, CXCR4), monocyte polarization (Ly6C), macrophage polarization (Ly6C, CD206, CD163), dendritic cell subsets (CD11b), and T cell subsets (CD4, CD8, CD25, FOXP3). The identification of these cell types can be visualized using UMAP (Fig. 35). This representative UMAP is from VML injured murine quadricep and is characterized by the large cluster of mononuclear phagocytes. With our panel we are able to assign identity to the vast majority of cells, with the presence of a few small clusters that remain unidentified (Fig. 35). The markers used to identify these cell types is shown in Fig. 36. For example, the dark purple cluster of "classical" monocytes on the right side of the UMAP is characterized by a high expression of Ly6C (Fig. 36F). Given that the modulation of muscle progenitor cells after treatment is important, we included surface markers (CD31, CD29, SCA-1, CXCR4) to identify the two main muscle progenitor cells: FAPs and MuSCs. These progenitor

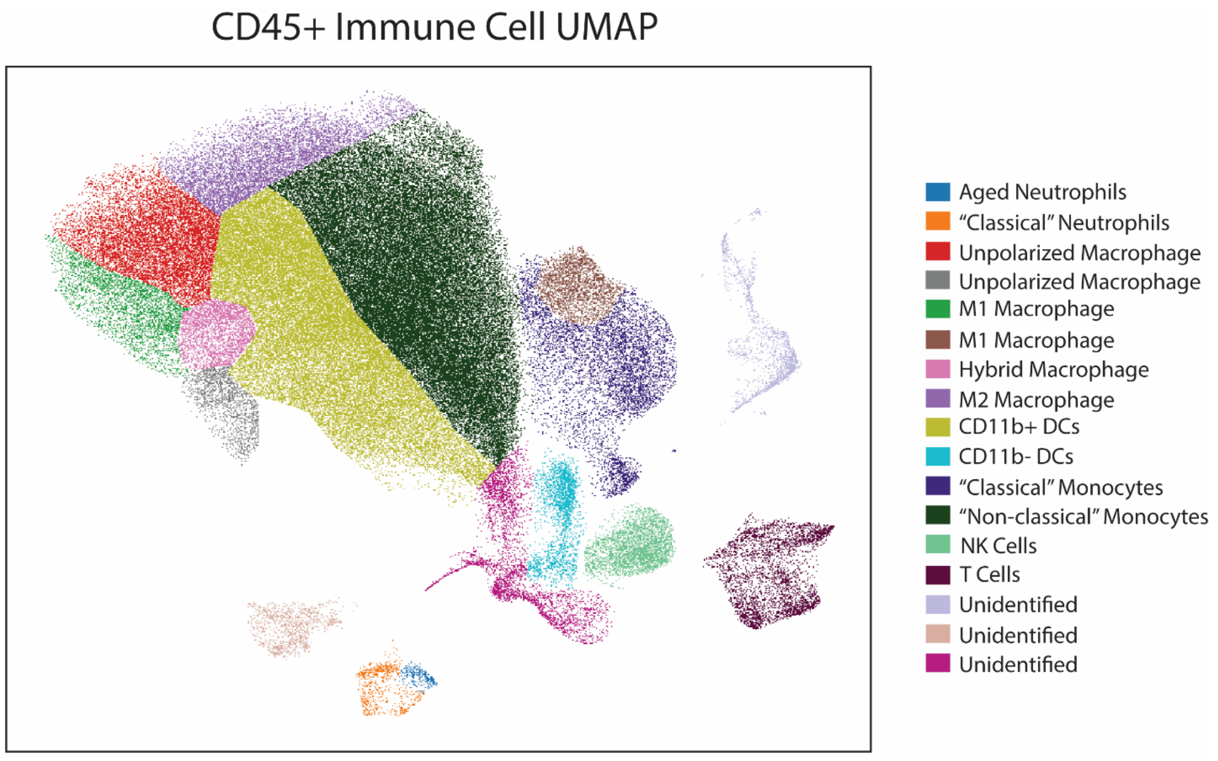

Figure 35. Overlay of immune cell subsets on UMAP of quadricep VML muscle tissue. This UMAP illustrates our ability to not only identify every UMAP "island" but also explore the heterogeneity within the large cell "islands" via spectral flow cytometry.

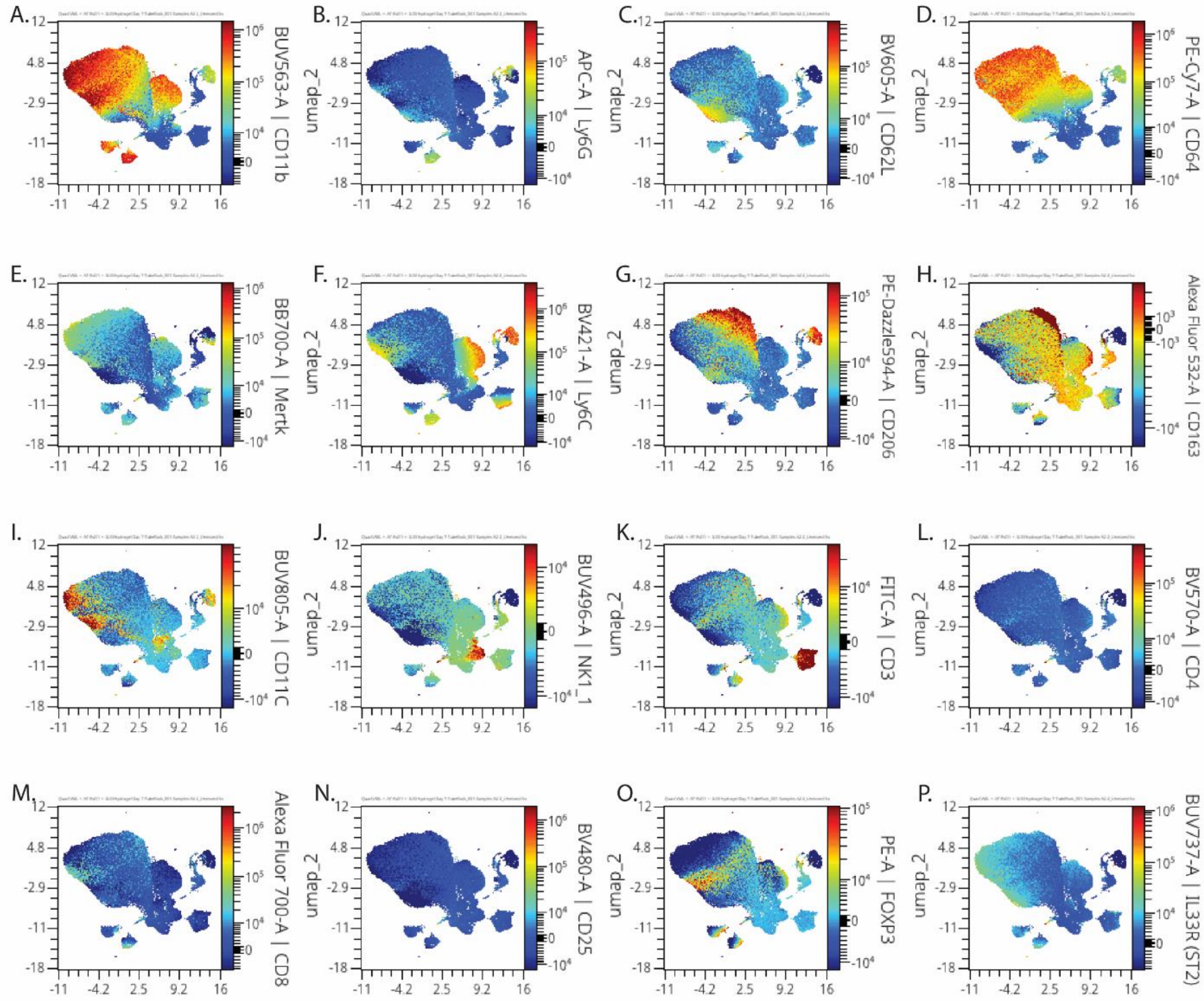

Figure 36. Marker expression overlay on CD45$^+$ cell UMAP.
(A-P) Shows the different marker expression overlayed as a heatmap onto the CD45$^+$ UMAP. The markers shown are the following: (A) CD11b, (B) Ly6G, (C) CD62L, (D) CD64, (E) Mertk, (F) Ly6C, (G) CD206, (H) CD163, (I) CD11C, (J) NK1.1, (K) CD3, (L) CD4, (M) CD8, (N) CD25, (O) FOXP3, (P) ST2.

cells are characterized by the absence of lineage surface markers and so we constructed a UMAP visualization of lineage negative cells using the same flow-cytometry panel (Fig. 37). The expression of markers used to identify FAPs and MuSCs are seen in Fig. 38. Here, we see an area of CD31$^-$SCA-1$^+$ expression (Fig. 38A and B) in the top right corner of the UMAP that is indicative of FAPs (Fig 37). Taken together, this high-dimensional spectral flow cytometry panel is targeted in its goal of identifying inflammatory cell subsets and muscle progenitor cells important in the

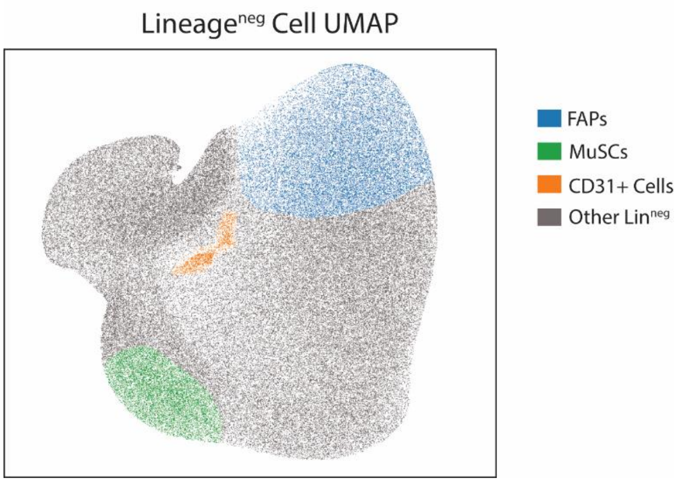

Figure 37. Overlay of identified muscle progenitor cell on Lineage^{neg} UMAP.
This UMAP illustrated our ability to identify the two main muscle progenitor cells of interest to us – FAPs and MuSCs. The large area of unidentified cells presents an opportunity to expand the panel in the future to capture more of these cells.

course of VML inflammation and regeneration. We leveraged this spectral flow cytometry panel and identified cellular subsets described here (Fig. 35 and 37) to quantify the cellular dynamics and modulation after quadriceps VML injury with local AT-RvD1 delivery.

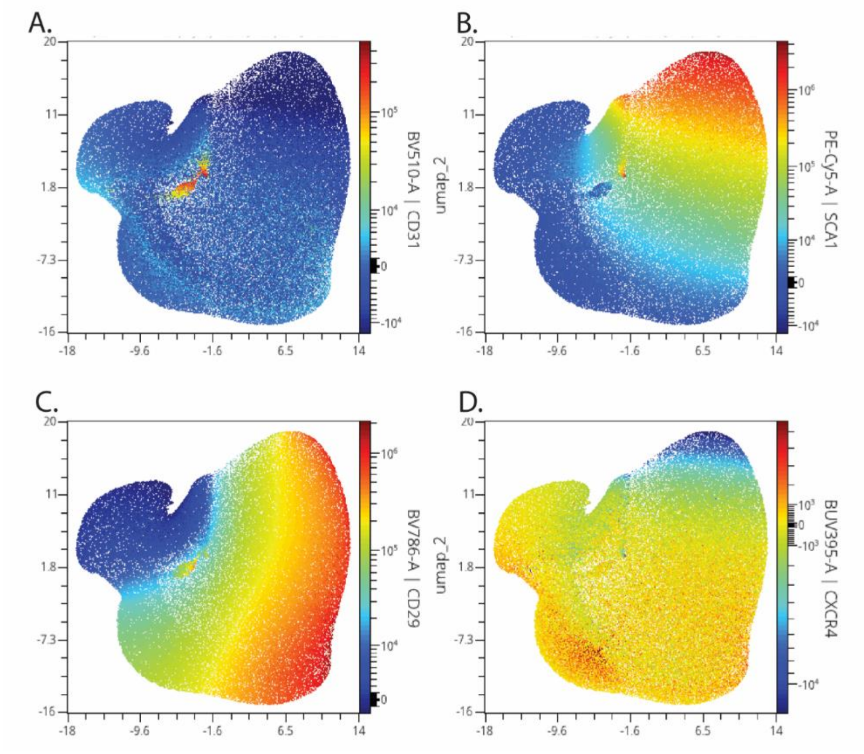

Figure 38. Marker expression overlay on Lineage^{neg} cell UMAP.
(A-D) Shows the different marker expression overlayed as a heatmap onto the Lineage^{neg} UMAP. The markers shown are the following: (A) CD31, (B) SCA-1, (C) CD29, (D) CXCR4.

5.2.3.2 AT-RvD1 delivery limits neutrophil infiltration and promotes pro-resolving monocyte polarization 3 days post VML injury.

We explored whether local AT-RvD1 stimulus modulates the early infiltrate of effector immune cells at 3 days post VML in the critical quadriceps pre-clinical model. Using single-cell spectral flow cytometry, we compared the concentration of total CD45$^+$ leukocytes at 3 days post VML between AT-RvD1-loaded hydrogel and a vehicle control hydrogel (Fig. 39A). The total concentration of these cells shows a decreasing trend with local AT-RvD1 delivery; furthermore, this decrease is driven by the significant decrease in neutrophil infiltration with AT-RvD1 when compared to control hydrogel (Fig. 39B). The mean concentration between control and AT-RvD1

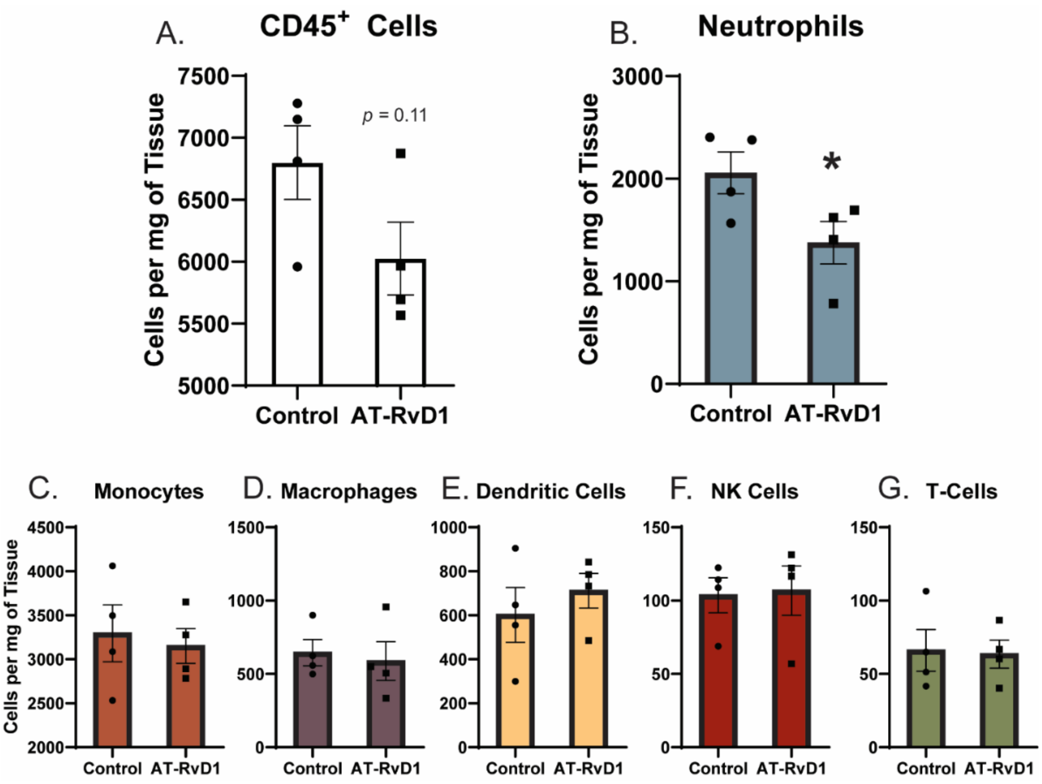

Figure 39. Pro-resolving hydrogel treatment after VML injury limits the infiltration of neutrophils.

The decreasing trend in CD45$^+$ immune cells (A) is driven by the significant decrease in the concentration of neutrophils at 3 days post VML with local AT-RvD1 treatment (B). The concentration of monocytes, macrophages, dendritic cells, NK cells and T-cells remain unchanged regardless of AT-RvD1 treatment (C-G). Statistical analyses were performed using two-tailed t tests; *P < 0.05; n = 4 animals per group.

are not significantly changed and within 10% of each other for monocytes, macrophages, dendritic cells, NK cells and T-cells. This indicated that limiting neutrophil infiltration is the main effect on immune cell infiltration of AT-RvD1 delivery after VML injury (Fig. 39C-G). Additionally, there are no significant differences in the concentration of identified pro-inflammatory or pro-resolving subsets of neutrophils, monocytes, dendritic cells, macrophages or T-cells subsets and muscle progenitor cells with AT-RvD1 treatment at 3 days post VML (Fig. 40A-N).

On average, 75-85% of the local cellular milieu at this early timepoint consists of monocytes and neutrophils (Fig. 39). Thus, the modulation of these populations is vital to push the

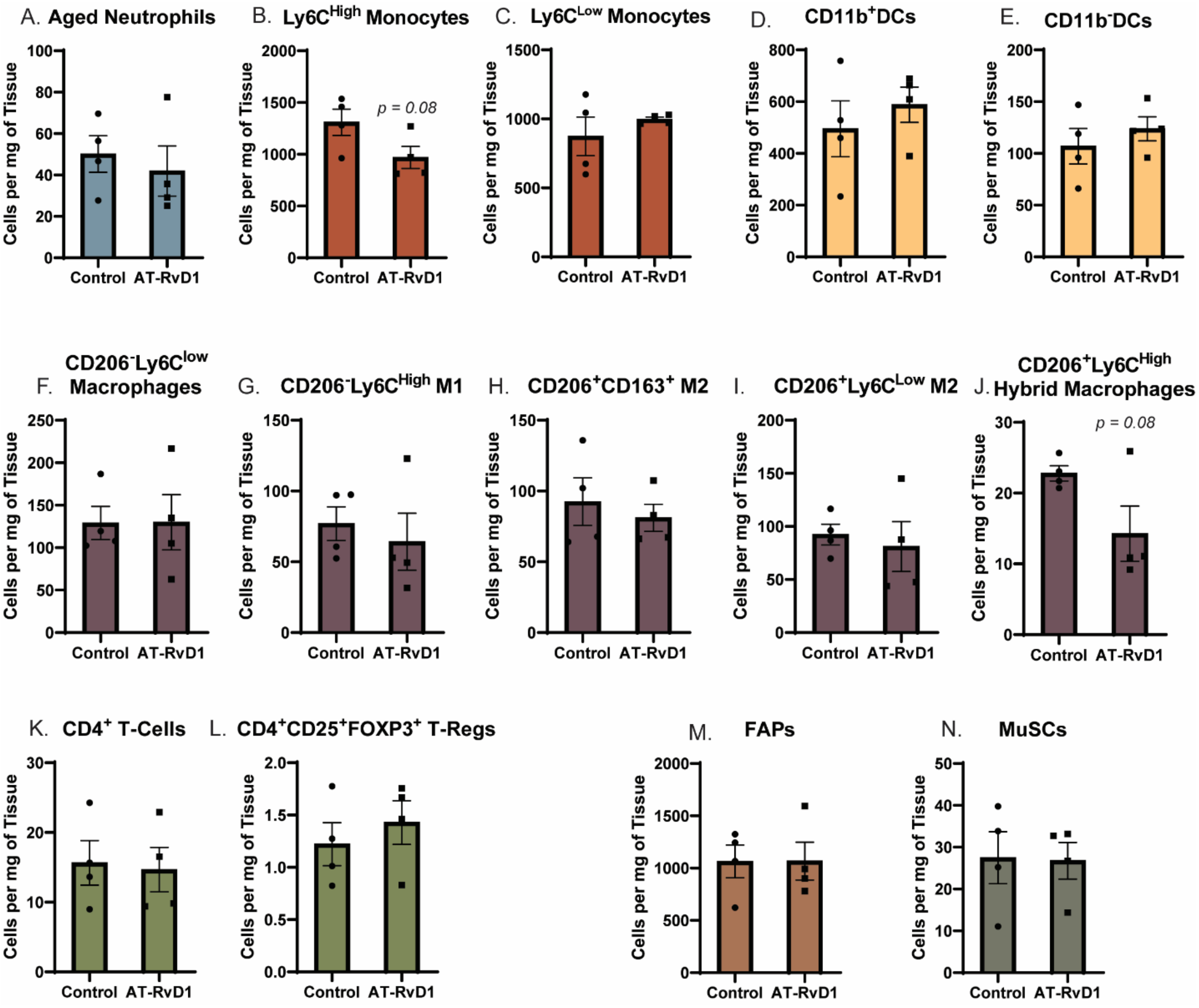

Figure 40. Concentration of identified cell subsets at 3 days post VML in control and pro-resolving hydrogel groups.

Using our spectral flow cytometry panel we are able to quantify the concentration of a variety of cell subsets. The following cells are quantified: (A) Aged neutrophils, (B) Ly6C^{High} monocytes, (C) Ly6C^{Low} monocytes, (D) CD11b^{+} dendritic cells, (E) CD11b^{-} dendritic cells, (F) CD206^{-}Ly6C^{Low} macrophages, (G) CD206^{-}Ly6C^{High} M1, (H) CD206^{+}CD163^{+} M2, (I) CD206^{+}Ly6C^{Low} M2, (J) CD206^{+}Ly6C^{High} hybrid macrophages, (K) CD4^{+} T cells, (L) CD4^{+}CD25^{+}FOXP3^{+} regulatory T cells, (M) FAPs, (N) MuSCs. Statistical analyses were performed using two-tailed t tests; n = 4 animals per group.

downstream inflammatory cascade towards resolution. Within the monocyte population, AT-RvD1 not only significantly decreases the percentage of Ly6c^{High} "classical" monocytes and increases the percentage of Ly6c^{Low} "non-classical" monocytes (Fig. 41A and B). Moreover, we, and others, have identified a pro-fibrotic, hybrid phenotype of macrophages that expresses both M1 and M2 markers (CD206^{+}Ly6c^{High}) that have increased production of both TGF-β and TNF-α) [147].Our results suggest that local AT-RvD1 delivery significantly the infiltration and polarization of pro-fibrotic macrophages in VML (Fig. 41C).

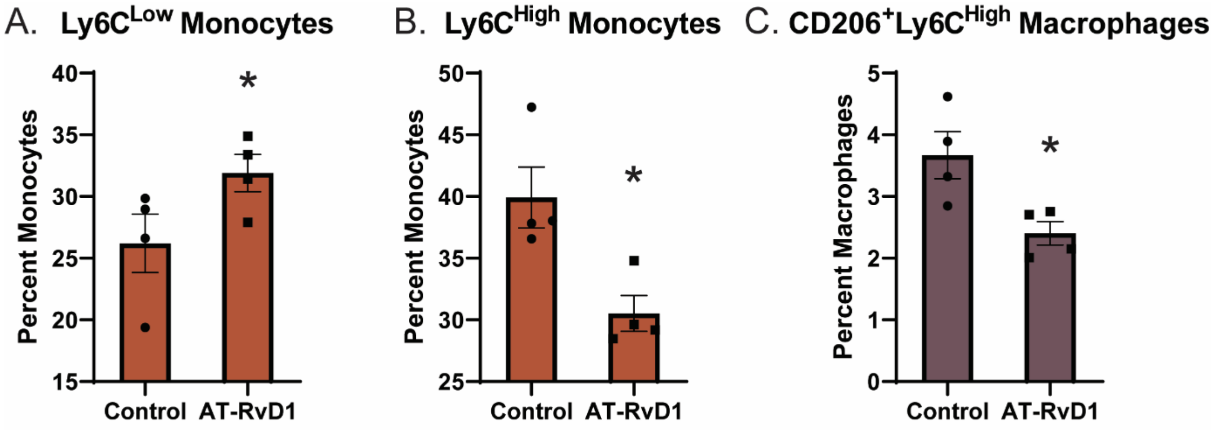

Figure 41. Pro-regenerative modulation of monocytes and macrophages with local AT-RvD1 delivery 3 days post VML.
(A and B) AT-RvD1 delivery to a critical quadriceps VML injury is able to increase the percentage of anti-inflammatory "non-classical" monocytes while decreasing that of inflammatory "classical" monocytes. (C) The presence of a fibrotic "hybrid" macrophage phenotype is limited by AT-RvD1. Statistical analyses were performed using two-tailed t tests; $^{*}P < 0.05$; n = 4 animals per group.

5.2.3.3 Pro-resolving hydrogel delivery results in a broad decrease of infiltrating immune cells at 7 days post VML indicative of inflammation resolution.

The sustained persistence of immune cells after VML injury is one of the main features that sets it apart from many other acute injury types [143]. After 7 days post VML, our pro-resolving hydrogel treatment significantly decreases the concentration of total $CD45^+$ immune cells in the defect area (Fig. 42A). While little to no changes in major immune effectors were detected (Fig. 42B-G), AT-RvD1 does significantly decrease in the accumulation of monocytes and NK cells (Fig. 42C and F). We see decreasing trend in immune cell subsets with AT-RvD1 treatment but not statistically significant differences (Fig. 43). Notably, there is a significant

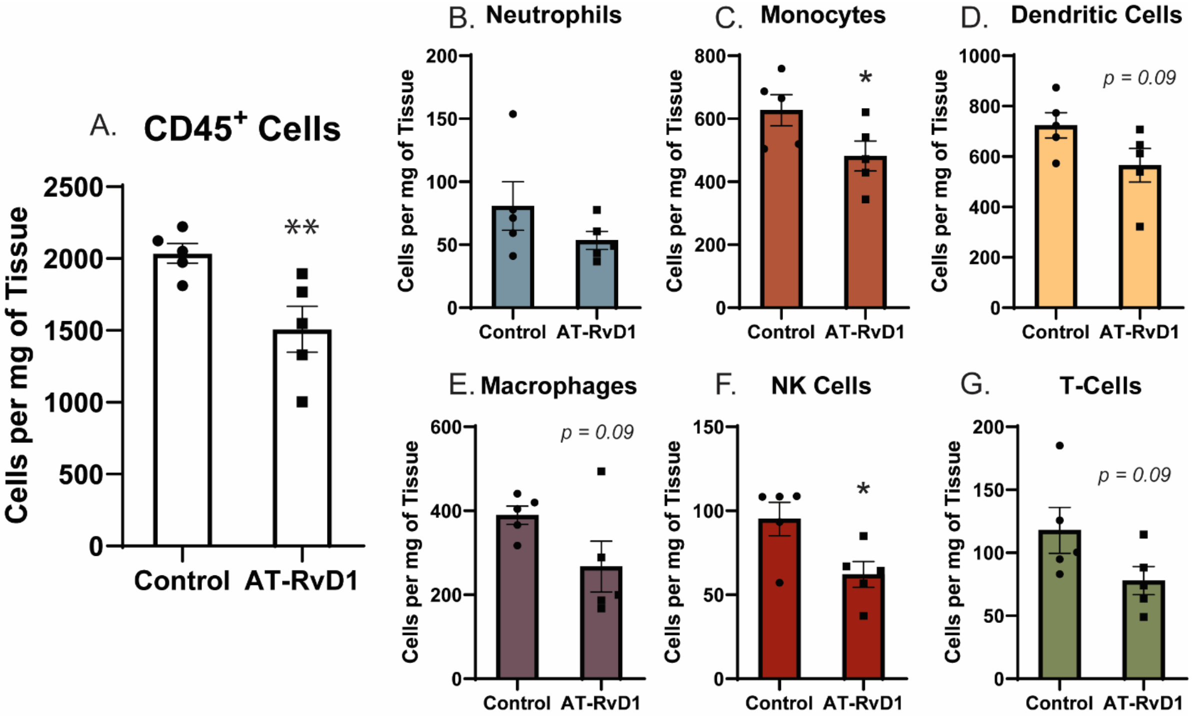

Figure 42. Local AT-RvD1 delivery significantly decreases concentration of immune cells in local defect area at 7 days post VML injury.
The significant decrease in total $CD45^+$ cells (A) with local AT-RvD1 delivery at 7 days post VML is characterized by a broad decreasing trend in neutrophils (B), dendritic cells (D), macrophages (E), and T cells (G) along with a significant decrease in monocytes (C) and NK ells (F). Statistical analyses were performed using two-tailed t tests; $*P < 0.05$; n = 5 animals per group.

reduction in the concentration of Ly6C^{high} "classical" monocytes with local AT-RvD1 treatment (Fig. 43B). Taken together, our analysis confirms that multiple contributors to the persistent inflammatory environment of non-healing VML injuries is resolved by the local delivery of pro-resolving hydrogels.

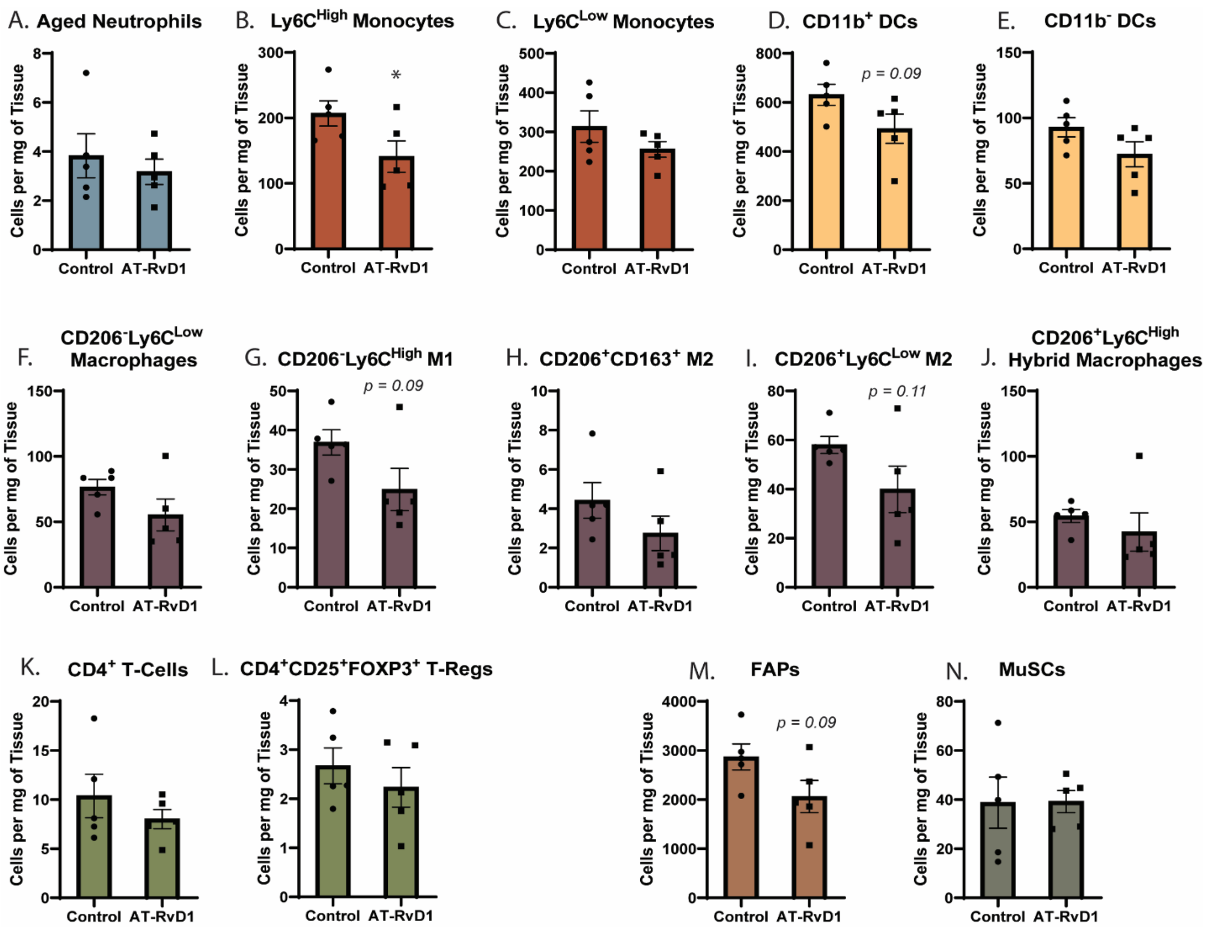

Figure 43. Concentration of identified cell subsets at 7 days post VML in control and pro-resolving hydrogel groups.

Using our spectral flow cytometry panel we are able to quantify the concentration of a variety of cell subsets. The following cells are quantified: (A) Aged neutrophils, (B) Ly6C^{High} monocytes, (C) Ly6C^{Low} monocytes, (D) CD11b^{+} dendritic cells, (E) CD11b^{-} dendritic cells, (F) CD206^{-}Ly6C^{Low} macrophages, (G) CD206^{-}Ly6C^{High} M1, (H) CD206^{+}CD163^{+} M2, (I) CD206^{+}Ly6C^{Low} M2, (J) CD206^{+}Ly6C^{High} hybrid macrophages, (K) CD4^{+} T cells, (L) CD4^{+}CD25^{+}FOXP3^{+} regulatory T cells, (M) FAPs, (N) MuSCs. Statistical analyses were performed using two-tailed t tests; *p<0.05; n = 5 animals per group.

5.2.4 Local AT-RvD1 delivery after preclinical quadriceps VML results in an improvement in muscle regeneration.

Having established via the spinotrapezius model that treatment with our developed pro-resolving hydrogel is able to significantly improve muscle regeneration 14 days post injury, we explored whether this was the case in the larger quadriceps pre-clinical VML model. By 14 days post-VML in the quadriceps model, there remains a large area devoid of myofibers with pockets of fatty infiltration. In addition to the large defect region in critical VML injuries, there is also an increase in highly cellularized areas in between individual myofibers, characteristic of unresolved inflammation [143]. In these studies, we compared vehicle control hydrogel and AT-RvD1-containing hydrogel treated non-healing VML injuries in the murine quadriceps. We evaluated whether the local delivery of AT-RvD1 ameliorates many of the hallmark human clinical features that are recapitulated by our pre-clinical model.

Cross-sections of mouse quadriceps at 14 days post VML were stained with hematoxylin and eosin (H&E) and immunohistochemically stained for dystrophin and DAPI to assess gross muscle healing after local AT-RvD1 treatment compared to vehicle control (Fig. 44). When comparing these two groups, we observe a considerable decrease in the size of the injury area with pro-resolving hydrogel treatment (Fig. 44). In the vehicle control hydrogel images (Fig. 44 A and B), many hallmark VML pathological features are not present in injuries treated with local AT-RvD1, as little to no areas were devoid of myofibers, there was no indication of fatty infiltration, no irregular myofiber organization and no increase in area of non-muscle cell types between myofibers (Fig. 44A and B).

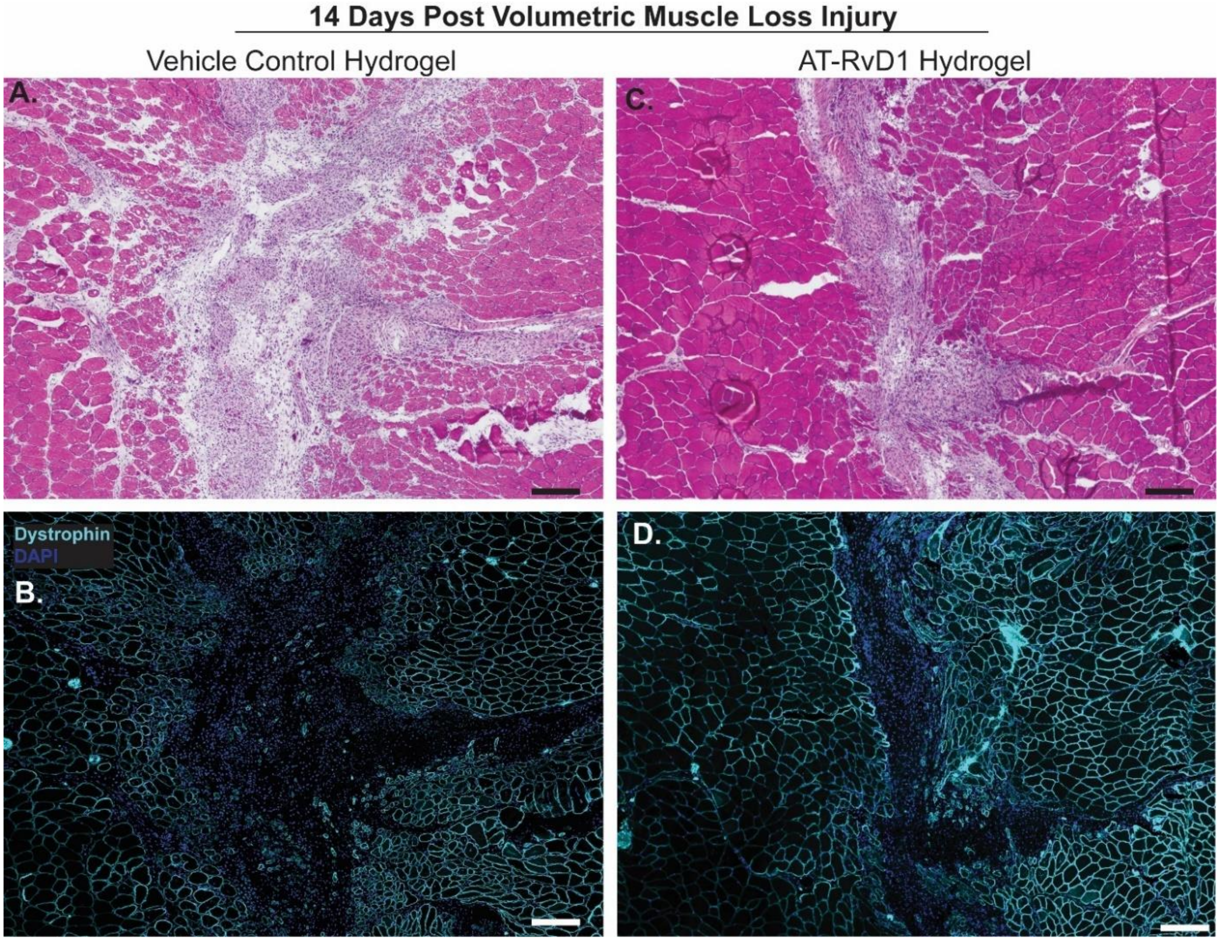

Figure 44. Local AT-RvD1 delivery results in a decreased defect size surrounded by compact myofibers.
Representative H&E stains (A and C) and corresponding IHC stains (B and D) of cross-sections of quadriceps 14 days post VML. Vehicle control treated VML maintains a large defect area devoid of myofibers with fatty infiltration (A and B). AT-RvD1 hydrogel treated VML exhibits a smaller defect area and compact regenerating myofibers (C and D).

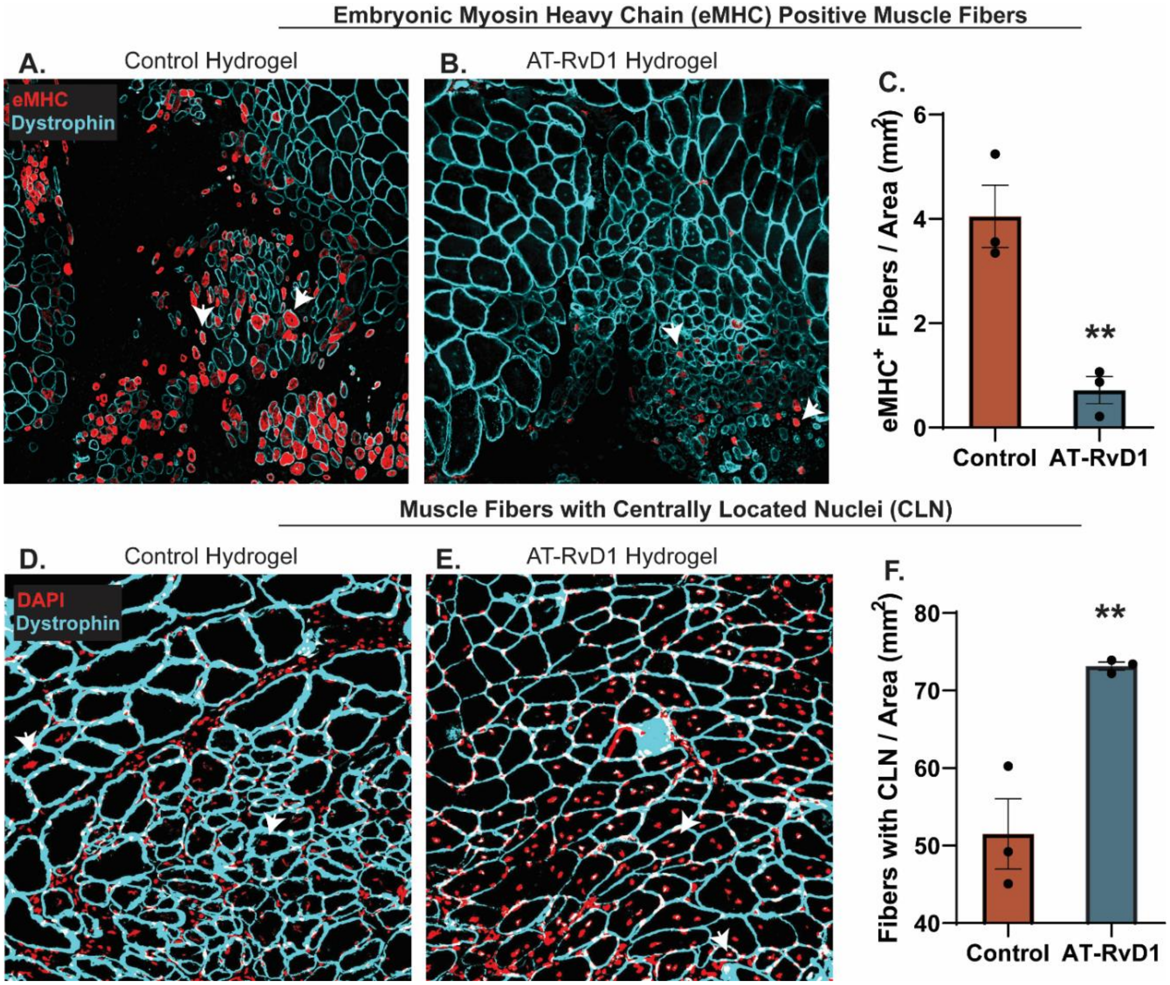

Figure 45. VML with pro-resolving hydrogel exhibits a more mature stage of myofiber regeneration at 14 days post injury.

Representative images of the defect area showing eMHC$^+$ myofibers (white arrows) with eMHC expression (red) and a ring of dystrophin (cyan) in the vehicle control and pro-resolving hydrogel groups (A and B). Quantification of eMHC$^+$ fibers normalized to area (C). Representative images of the defect area showing centrally located nuclei as myofibers (white arrows), seen as a dystrophin$^+$ (cyan) ring with a centrally located nuclei (red) (D and E). Quantification of number of centrally located nuclei between vehicle control and AT-RvD1 groups normalized to area (F). Statistical analyses were performed using two-tailed t tests; *p<0.05; n = 3 animals per group.

At 14 days post-VML, we assessed regeneration in the defects by quantifying myofibers which were eMHC positive or had centrally located nuclei (Fig. 45). eMHC is considered a marker for newly regenerated myofibers as it is transiently expressed during the early stages of myofiber development [148]. While centrally located nuclei are another marker for regenerated myofibers, the presence of centrally located nuclei persists longer than eMHC. Representative images of the defect area between vehicle control and AT-RvD1 hydrogel shows the striking difference in number of $eMHC^+$ myofibers (Fig. 45A and B; white arrows). This is quantified as number of $eMHC^+$ myofibers normalized to area and our results show a significant decrease in the presence of this early marker of regenerating myofibers with AT-RvD1 treatment (Fig. 45C). On the other hand, there is a significant increase in the number of myofibers with centrally located nuclei (Fig. 45D and E; white arrows) in the defect area with local AT-RvD1 delivery at 14 days post VML injury (Fig. 45F). This increase in a marker of myofiber regeneration that is sustained in successful regeneration indicated that local AT-RvD1 delivery is promoting muscle regeneration post VML. We measured the cross-sectional area of myofibers around the defect area and observed a larger number of smaller sized fibres with AT-RvD1 hydrogel (Fig. 46), this may be indicative of this increase in new fibres.

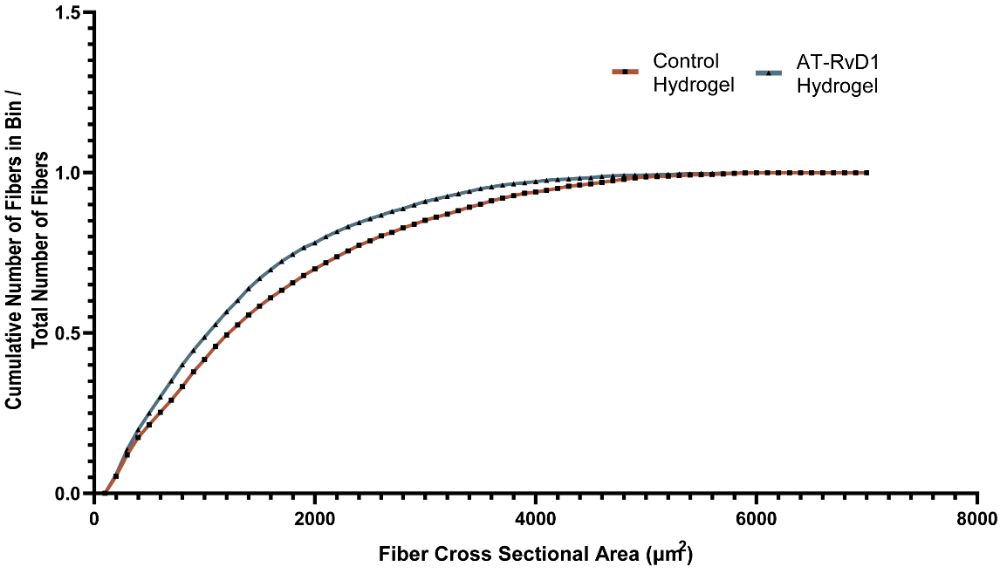

Figure 46. Quantification of fiber cross-sectional area between vehicle control and AT-RvD1 hydrogels 14 days post VML.
Quantification of cross sectional area of myofibers around the defect area at 14 days post VML with control an AT-RvD1 hydrogel.

A key component in successful muscle regeneration is also the successful formation of vessels after injury. Thus, we visualized endothelial cells by staining for Von Willebrand Factor (vWF) and identified vessels within the defect area and around regenerating fibers (Fig. 47). We did not observe a difference in the number of vessels present between control and pro-resolving hydrogel (Fig. 47A and B). However, we quantified the average cross-sectional area of vessels within the defect area and there is a significant increase in the size of newly formed vessels with local AT-RvD1 treatment at 14 days post VML injury (Fig. 47C). This indicates that regenerating muscle with AT-RvD1 treatment 14 days post VML is more vascularized compared to control hydrogel treatment.

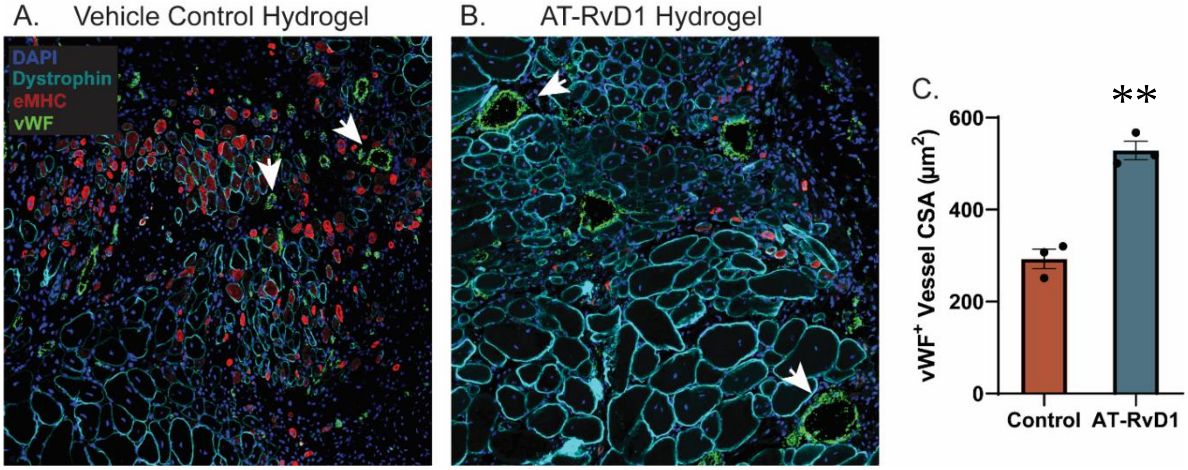

Figure 47. Increased vascular size 14 days post VML injury with local AT-RvD1 delivery. Representative images of vessels (white arrows), represented by a ring of endothelial cells (vWF$^+$; green), around regenerating myofibers in vehicle control (A) and pro-resolving hydrogel (B) treated VML injuries 14 days post VML. Quantification of the average cross-sectional area of vessels (C). Statistical analyses were performed using two-tailed t tests; *p<0.05; n = 3 animals per group.

These results show that local AT-RvD1 delivery in a critical quadriceps VML model decreases the area of the defect and results in a more compact myofiber structure around the defect at 14 days post VML (Fig. 44). This improvement in muscle healing is quantified via the significant decrease in an early marker of muscle regeneration (eMHC) and the increase ofmarkers of more mature regenerating myofibers (centrally located nuclei) (Fig. 45). Furthermore, there is a significant increase in the area of vessels surrounding the regenerating myofibers with AT-RvD1 treatment (Fig. 47). Taken together, these results show that hydrogel-mediated delivery of AT-RvD1 promotes the successful regeneration of muscle after a non-healing quadricep VML injury.

5.2.5 In vivo isometric torque testing shows that local AT-RvD1 delivery is able to recover muscle function 25 days post VML

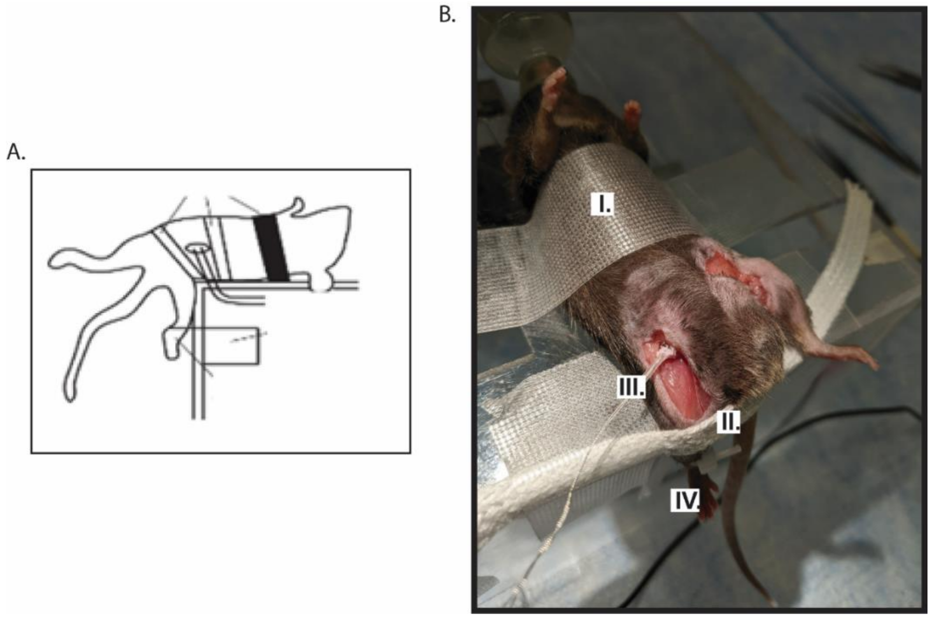

Figure 48. *In vivo* isometric torque setup.
(A) Schematic of the setup to measure quadricep force generation. (B) Setup for the measurement of *in vivo* torque from the right quadriceps muscle. The mouse body and knee are secured (I. and II.) in order to isolate force measurement from the quadricep muscle. The femoral nerve is cuffed (III.) and connected toa stimulator in order to provide the stimulation necessary to generate muscle contraction. Once stimulated, the mouse will kick out and that force is measured by a force transducer attached to the right ankle (IV.).

The main clinical challenge in the treatment of traumatic VML injuries is the recovery of muscle function after treatment. This inability to recover function often results in a permanent disability following such an injury [149]. Thus, an important endpoint of a VML therapeutic is the quantification of *in vivo* force generation after injury. This pre-clinical quadriceps VML injury presents with a sustained loss of function similar to that of clinical VML injuries. Having established the ability of our pro-resolving hydrogel therapeutic to increase biosynthesis of SPMs, promote the cellular resolution of inflammation, and increase various metrics of muscle regeneration, we tested the ability of this therapeutic to recover muscle function. We used an *in vivo* isometric torque assessment that allows us to directly stimulate the femoral nerve and measure the resulting *in vivo* torque of the quadriceps muscle [150] (Fig. 48).

We assessed the ability of the pro-resolving hydrogel therapeutic to improve muscle function at 25 days post VML injury compared to untreated and vehicle control hydrogel VML injuries (Fig. 49). We first compared the maximal torque produced between untreated, vehicle control hydrogel, and AT-RvD1 hydrogel treated VML injuries (Fig. 49A). This quantification shows that muscle treated with local AT-RvD1 produces significantly more torque than an untreated VML injury at 25 days post VML (Fig. 49B). Furthermore, we normalized the force produced in each injured quadricep to its corresponding healthy contralateral quadricep muscle. This produces a percentage indicative of how similar the injured quadricep performs to the healthy control in terms of function (e.g. 100% indicated complete functional equivalence with the uninjured contralateral muscle). Using this metric, the untreated VML muscle is only able to produce, on average, 49.5% of the force compared to its contralateral control (Fig. 49C). Strikingly at 25 days post injury, VML quadricep muscle treated with the pro-resolving hydrogel restore 85.6% of the force compared to its contralateral control, a significant increase compared to untreated VML injuries (Fig. 49E). This data established hydrogel-mediated AT-RvD1 treatment as an effective way to restore muscle function after critical VML injury.

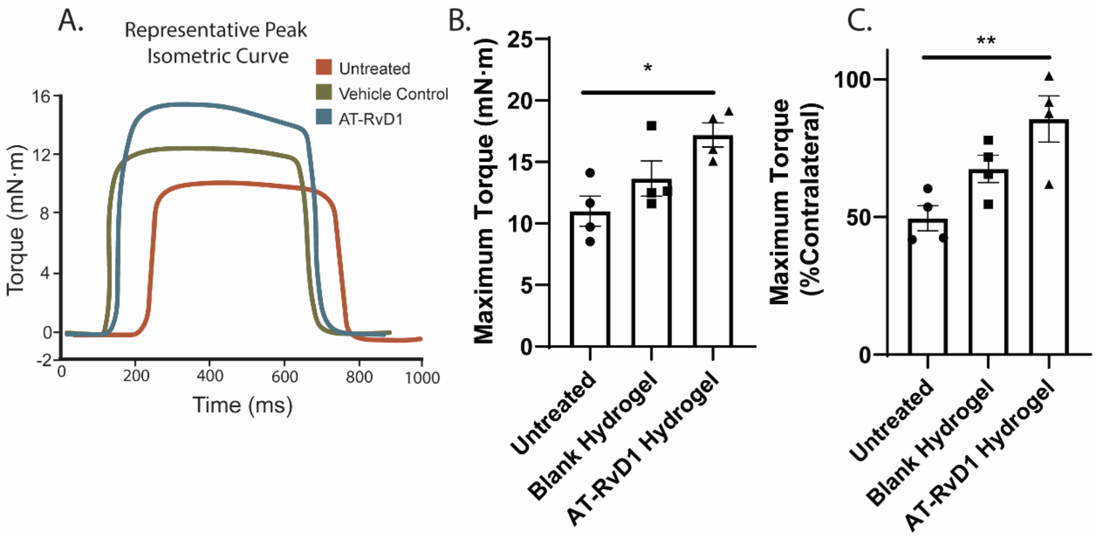

Figure 49. Pro-resolving hydrogel treatment after VML injury improves muscle force generation compared to untreated and vehicle control hydrogel at 25 days post injury.

Smoothed representative isometric force curves for each group (A) shows a sustained force production during quadricep stimulation. The maximum torque was quantified and reported as mN-m (B). This torque was normalized to the torque produced from the healthy contralateral muscle to quantify the percentage of force generated in the injured quad compared to a healthy muscle (C). Statistical analyses were performed using a one-way analysis of variance (ANOVA) with Tukey's multiple comparisons; *$P < 0.05$ and **$P < 0.01$; n =4 animals per group.

5.3 Discussion

Our results in chapter 4 suggest an impairment in the ability of the local injury environment to produce SPMs after a VML injury. We expanded upon those results and leveraged mass-spectrometry based lipidomics to measure the abundance of lipid mediators derived from AA, DHA, and EPA in a pre-clinical model of VML at various timepoints (days 1, 3, 5, 7 and 14 post injury) within the inflammatory cascade. Our findings are among the first comprehensive liquid chromatography mass-spectrometry based lipidomic profiling analysis of SPMs in an established pre-clinical model of VML. Our results suggest that there is a robust but transitory pro-inflammatory response characterized by a sharp spike in Prostaglandins at 1 day post VML that return to uninjured baseline by 3 days post VML. Lipoxins are a class of SPM derived from AA that mark the transition from production of pro-inflammatory to pro-resolving lipid mediators [26]. Interestingly, when analyzing the production of this AA-derived SPM we observe that the concentration of the monohydroxy intermediate in this pathway is significantly increased indicating that 15-LOX activity with AA as the substrate is elevated post VML injury. However, we do not observe an increase in the concentration of the downstream bioactive lipid Lipoxin. Furthermore, when analyzing the SPMs derived from both DHA and EPA we see the concentration follow a general decreasing trend after critical VML injury, with no appreciable accumulation of SPMs. Thus, our results suggest a unique impairment in the ability of the local injury environment to produce SPMs after a VML injury. A similar observation was found in the muscle of aged mice where the local injury environment of aged mice was characterized by the absence of downstream pro-resolving lipid mediators and impaired myofiber regeneration [49].

Our previous results establish the effectiveness of local AT-RvD1 delivery to significantly increase the concentration of many SPMs and generate a pro-regenerative cellular environment after VML. We expanded our ability to identify and quantify immune cell heterogeneity along with muscle progenitor cells in one flow cytometry panel by leveraging spectral flow cytometry [146]. This designed panel allows us to identify 16 unique cellular subsets important to the inflammatory and pro-resolving response along with muscle fiber and ECM remodeling. We used this spectral flow cytometry panel to quantify the modulation of inflammatory cell subsets and muscle progenitor cells at days 3 and 7 post VML after local AT-RvD1 delivery; however, the design and optimization of this panel is also impactful in its usability for various tissue injury and regeneration models. We observe a persistence of immune cell infiltration and a specific persistence and dysregulation of macrophages after critical VML injury [147]. Our results show that local AT-RvD1 promotes the resolution of inflammation via its actions of limiting neutrophil infiltration and promoting “non-classical” monocytes at day 3 post VML and by decreasing the persistence of immune cells at day 7 post VML when compared to vehicle control. Given that a hallmark of VML is the persistence of infiltrating immune cells [10], the ability to decrease the presence of these cells in the defect area with AT-RvD1 treatment is critical to achieving resolution of inflammation.

In chapter 3, we took advantage of whole mount, full-thickness IHC to observe a decrease in defect area after spinotrapezius VML with local AT-RvD1 treatment. Here, we analyzed metrics of muscle regeneration after VML with or without local AT-RvD1 treatment using H&E and IHC staining of quadricep cross-sections. Pro-resolving hydrogel treatment decreases the total defect area at 14 days post VML injury. Furthermore, we observe an increase presence of non-muscle cell types between regenerated myofibers in the vehicle control treated VML injuries. We quantify both eMHC$^+$ and centrally located nuclei as a metric of regenerating myofibers at 14 days post VML. In acute skeletal muscle injury models, eMHC expression is not typically seen after 7 days postinjury [151-153]. However, in vehicle control hydrogel treated VML injuries we still see eMHC expression at 14 days post VML that could indicate a delayed or continued attempt at muscle regeneration, not seen in acute muscle injury models. Local AT-RvD1 treatment ameliorates this outcome as seen by a significant decrease in eMHC expressing myofibers compared to vehicle control. Furthermore, we observe a significant increase in regenerating myofibers as identified via centrally located nuclei with local AT-RvD1 treatment. These results indicate that while VML injuries with a vehicle control hydrogel have a delayed and/or continuous attempt at muscle regeneration, local AT-RvD1 delivery results in the healthy regeneration of muscle characterized by a loss of eMHC expression by day 14 post VML with an increase in more mature regenerated fibers. Additionally, local AT-RvD1 results in an increase in vascular area around regenerating fibers in the defect area at 14 days post VML.

The ultimate clinical goal of a therapeutic aimed at treating traumatic injuries resulting in VML is the improvement of muscle function. The pre-clinical quadriceps VML model allows us to measure *in vivo* force production via an isometric torque analysis. We compared the ability of untreated, vehicle control hydrogel and pro-resolving hydrogel treated VML injuries to generate force at 25 days post VML. We compared the results of the injured quadriceps to the healthy contralateral control in order to measure the percentage of muscle function as compared to a healthy muscle. Remarkably, VML injuries treated with pro-resolving hydrogel generate 85% of the force that a healthy muscle produces at 25 days post VML. This is significantly improved to the 50% of force that a untreated muscle generated with respect to healthy muscle.

5.4 Conclusion

Our work established that the local VML environment is unable to produce pro-resolving lipid mediators mirrored by the persistent and dysregulated inflammatory response. Thus, we utilized our previously engineered pro-resolving hydrogel to achieve functional muscle recovery in the quadriceps pre-clinical VML model. We also take advantage of spectral flow cytometry technology to design and optimize a panel targeted towards important immune cells and muscle progenitor cells. Our results using spectral flow-cytometry show the ability of local AT-RvD1 to begin to decrease persistent immune cells at 7 days post VML. This demonstrates the ability of utilizing biomaterial-mediated delivery of AT-RvD1 to locally resolve the persistent inflammation characterizing VML injuries. Furthermore, we observe a promoted regenerative response 14 days post VML and AT-RvD1 delivery via the increase of regenerating myofibers and increase in vessel size. Finally, we show that this therapeutic platform significantly improves muscle function recovery compared to untreated injuries.

5.5 Materials and Methods

5.5.1 Pro-resolving hydrogel synthesis

Four-arm PEG macromer (10-kDa molecular weight) end functionalized with maleimide (>95% purity; Laysan Bio) at a final density of 4.5% (w/v) was used for all hydrogel formulations as described previously [119, 122]. PEG macromers were functionalized with RGD peptide (GRGDSPC), cross-linked with the protease-degradable cysteine-flanked peptide VPM (GCRDVPMSMRGGDRCG) (AAPPTec) in 0.5 M MES buffer (pH 5.5). The final concentration of RGD was 1.0 mM. Gels were also loaded with 100ng of AT-RvD1 (4 μg/ml) (Cayman Chemical). The cross-linker concentration was adjusted to consume non-reacted maleimide groups remaining on PEG macromers. For hydrogels used in animal studies, all components were filtered through a spin column after pH measurements and kept under sterile conditions until injection into the animals and in situ polymerization.

5.5.2 Quadriceps surgery and hydrogel implantation

Surgical procedure performed as previously reported [139]. Briefly, the left hindlimb was prepped and sterilized. An incision was made above the quadriceps and either a 2mm (for sub-critical VML analysis) or a 3 mm (for critical VML analysis) biopsy punch (VWR, 21909-136) was used to make a full-thickness muscle defect. The skin was closed and animals (Male C57/BL6 mice) were allowed to heal for either 3 or 7 days before euthanasia by CO2 inhalation. Hydrogel components were mixed, loaded into a syringe, and injected in the defect area.

5.5.3 *Mass spectrometry quantification of pro-inflammatory eicosanoids and SPMs from quadricep muscle tissue.*

6mm biopsy punches around the defect area of quadriceps muscle was homogenized using a glass homogenizer with ice cold PBS using a bead homogenizer. Eicosanoids and SPMs were selectively extracted from the homogenized samples by SPE to account for their low concentrations in comparison to lipid species of higher abundance. For this, samples were extracted using an automated C18 SPE manifold (Biotage Extrahera, Uppsala, Sweden). Samples were prepared by depositing homogenized samples on the SPE plate, the sample was rinsed with 800 µL water, followed by 800 µl hexane. The oxylipins were then eluted off from the SPE column with 400 µL methyl formate. The recovered oxylipin fraction was then dried under N2 and subsequently reconstituted in methanol to be analyzed by LC/MS. Extracted lipids were resolved using an Agilent Infinity II/6495c LC-MS/MS system. To quantify the SPMs in extract, 10 µl sample was injected onto an Accucore C18 column (100 x 4.6, Thermo, Waltham, MA) and resolved on a 16-minute gradient using water as Solvent A and acetonitrile as Solvent B, both contain 0.1% formic acid. The column was heated to 50°C in a temperature-controlled column chamber and 0.5mL/min flow rate was used for analysis. Eluted oxylipins were analyzed by Agilent 6495c triple quadrupole mass spectrometer. Instrument parameters (reported below) were optimized using external analytical grade standards and were held consistent over the course of analysis. Oxylipins were analyzed in the negative ion mode using a multiple reaction monitored (MRM) based method. For this, the mass of the target lipid and a characteristic fragment were targeted for detection. Oxylipins were quantified using MassHunter software, where the area under the curve of each identified lipid is calibrated against an external calibration curve. To create the curve, analytical grade standards in the linear range of 0.1nM-10nM are created for each standard. The lower limits of detection and upper limits of detection are determined, plotting concentration versus area under the curve. The slope of the linear regression equation is used for calibration of the corresponding analyte. Instrumental parameters were optimized this lipid class using internal standards and were held constant during the course of the experiment. For each standard, serial dilutions were prepared that cover a broad range of concentrations, typically in the range of 0.01 μM to 1.0 mM, to determine the upper and lower limits of detection (LLOD). It should be noted that the LLOD is at least 10 times the noise level.

5.5.4 *Tissue harvest and spectral flow cytometry analysis*

To collect tissue for flow cytometry analysis, mice were euthanized via CO_2 asphyxiation. For analysis of cell composition in quadriceps muscles, a 6 mm biopsy punch of muscle tissue centered on the defect was taken, weighed, and digested with 5,500 U/mL collagenase II and 2.5 U/mL Dispase II for 1.5 h in a shaking 37°C water bath. The digested muscles were filtered through a cell strainer to obtain a single cell suspension. Single-cell suspensions were stained for live cells using either Zombie NIR(BioLegend) dyes in cell-culture grade PBS per manufacturer instructions. Cells were then stained with cell phenotyping antibodies in a 1:1 volume ratio of 3% FBS and Brilliant Stain Buffer (BD Biosciences) according to standard procedures and analyzed on a FACS Aria III flow cytometer (BD Biosciences). The following antibodies were used for cell phenotyping: CXCR4 (BUV395), NK1.1 (BUV496), CD11b (BUV563), ST2 (BUV737), CD11c (BUV805), Ly6C (BV421), CD25 (BV480), CD31 (BV510), CD4 (BV70), CD62L (BV605), CD29 (BV786), CD3 (FITC), CD163 (AF532), Mertk (BB700), CD45 (Percp Cy5.5), FOXP3 (PE), CD206 (PE-Dazzle 594), SCA-1 (PE-Cy5), CD64 (PE-Cy7), Ly6G (APC).

Single, live cells were selected in Omiq software for subsequent cell subset analysis.

5.5.5 *Quadricep tissue histology and immunostaining*

Tissue histology and immunostaining performed as previously reported [143]. Briefly, ryosections (CryoStar NX70 Cryostat) were taken at 10 μm thickness, and stained with hematoxylin and eosin (H&E) (VWR, 95057-844, -848) according to the manufacturers' instructions. Before antibody staining, tissue sections were blocked and permeabilized using blocking buffer (5% BSA, 0.5% goat serum, 0.5% Triton-X in 1 × PBS) for 30 min and an additional wash with Goat F(ab) antimouse IgG (Abcam; ab6668, 2 μg/mL in blocking buffer) was performed for 1 h. Samples were washed between steps with 0.1% Triton in PBS. Primary antibodies were diluted in blocking buffer at 1:200 for dystrophin (Abcam; ab15277) and von Willebrand factor (vWF) (Abcam; ab6994). Primary antibody for embryonic myosin heavy chain (eMHC) (DSHB, F1.652) was diluted 1:10 in blocking buffer. All primary antibodies were incubated for 1 h. Secondary antibodies were conjugated to Alexa Fluor 488 (Thermo Fisher; Ms: A-11029, Rb: A-11034), 555 (Thermo Fisher; Ms: A-21424, Rb: A-21429), or 647 (Thermo Fisher; Ms: A-21236, Rb: A-21245). All secondary antibodies were diluted 1:250 in blocking buffer and incubated for 30 min. Slides were mounted with Fluoroshield Mounting Medium with DAPI (Abcam; ab104139) and stored at 4°C.

5.5.6 *Confocal imaging and quantification of eMHC$^+$ fibres, centrally located nuclei and fibre cross-sectional area.*

Confocal imaging and quantification performed as previously reported [143]. Immunofluorescence images were taken on Nikon W1 Spinning Disk Confocal microscopes at 20 × and stitched together with Nikon Elements AR. The dystrophin images were analyzed using ImageJ by thresholding and using the Analyze Particle function for particles of 0.25–1.0 circularity and 150–6000 μm2 in area to measure muscle fiber cross-sectional area in a 1.5 by 1.5mm area around the defect. Area histograms were created in GraphPad Prism 7 (GraphPad Software, Inc., San Diego, CA). Data were grouped by injury size or contralateral control, with three replicate measurements taken from 4 (n) animals for each group. Quantification of eMHC+ myofibers was done on images containing all channels (eMHC, dystrophin, DAPI). The brightest fibers of entire stitched sections were counted using the ImageJ multipoint tool. Each replicate slide was counted twice, and all counts for each injury size were analyzed. Centrally located nuclei were analyzed by taking five representative regions of each section, three replicates per animal (n = 3), and counted using the Image J multipoint tool.

5.5.7 In vivo isometric torque analysis

Quadriceps function was assessed isometric torque about the knee, with a set up and protocol adapted from previous studies in rat quadriceps VML [150]. Briefly, mice were anesthetized with 2% isoflurane. Hindlimbs were shaved and a 1 cm incision was made in the skin on each side to expose the quadriceps and medial vasculature and motor neurons. The femoral nerve was isolated from the surrounding connective tissue. Mice were fixed in place in a supine position on the testing box and the ankle of one limb at a time was secured to a force transducer.The femoral nerve was stimulated with a nerve cuff attached to a Grass S11 Stimulator set to 0.2 ms pulse duration, 5.7 ms pulse interval, and 500 ms train duration. The stimulus was directed through a Grass Stimulus Isolation Unit (SIU) before connecting to the nerve cuff. Force data was recorded using a data acquisition board (USB-1608G) and LabView software. Voltage was varied until maximal torque was measured, then 3 trials were recorded. Data analysis was done using MATLAB (Mathworks, Natick, MA). The find peaks function was used to pick out the 3 peaks from the testing file.

Voltage values were converted to force and then multiplied by an average mouse tibia length (2 cm) to get torque about the knee.

CHAPTER 6. CONCLUSIONS AND FUTURE DIRECTIONS

6.1 Overall Summary

The work presented in this thesis represents a significant contribution to the fields of biomaterials and regenerative medicine by demonstrating that local delivery of a pro-resolving lipid mediator can enhance the endogenous biosynthesis of specialized pro-resolving lipid mediators and promote the resolution of cellular inflammation to improve the recovery of functional muscle after traumatic injury. This work expands the understanding of the pro-inflammatory and pro-resolving lipid mediator response after a traumatic injury and develops a platform to modulate the lipid response towards resolution.

In aim 1, we explored how biomaterial-mediated delivery of the SPM AT-RvD1 modulates the infiltration of immune cells and their polarization states to improve microvascular remodeling and wound healing in two different inflammatory injury models. We utilized PLGA thin films as a model biomaterial delivery system to establish the effectiveness of local AT-RvD1 delivery on early immune cell infiltration. We found that the local delivery of AT-RvD1 modulates neutrophil dynamics to accumulate the pro-angiogenic subset of neutrophils. This led to improved microvascular remodeling, finding significantly increased expansion of $CD31^+$ capillary networks in peri-implant areas. We then designed a PEG-4MAL hydrogel platform to deliver AT-RvD1 for translatability to larger injury contexts. We validated the results of the hydrogel-mediated delivery of AT-RvD1 in the same model of inflammation and found similar results of improved microvascular remodeling and accumulation of pro-regenerative immune cell subsets. Furthermore, in a model of murine skin transplant this pro-resolving hydrogel enriches the local transplant environment with pro-regenerative macrophages and dendritic cells to promote wound healing. Taken together, these results indicate the ability of local delivery of AT-RvD1 to promote wound healing via modulation of infiltrating immune cells.

In aim 2, we demonstrate for the first time the ability of a locally delivered pro-resolving therapeutic to enhance the endogenous biosynthesis of SPMs after traumatic VML injury. Mounting evidence suggests that a dysregulated lipid mediator response is responsible for persistent and chronic inflammation, and we show via LC-MS/MS after VML injuries that there is a dysregulated lipid mediator response following VML injury. We treated VML injuries with our pro-resolving hydrogel to show that we activate pathways of resolution via the increase in concentration of various SPMs. Furthermore, we see activation of cellular inflammation characterized by a decrease in early neutrophil infiltration and polarization of monocytes and macrophages towards pro-resolving and pro-regenerative phenotypes. Assessment of muscle healing via whole mount immunohistochemistry at 14 days post VML reveals that local AT-RvD1 delivery promotes muscle regeneration to achieve a 90% increase in defect closure compared to untreated vehicle control hydrogel. Additionally, second harmonic generation imaging shows that pro-resolving hydrogel treatment after VML injury results in increased collagen and muscle fiber organization. These results demonstrate the effectiveness of a local AT-RvD1 hydrogel delivery platform to promote endogenous biosynthesis of SPMs and locally enhanced muscle regeneration.

In aim 3, we applied these pro-resolving hydrogels to a pre-clinical quadriceps VML model that exhibits the hallmarks of clinical VML. We explored the lipid mediator response to VML in depth at various timepoints after VML to reveal a robust but transient pro-inflammatory lipid mediator production followed by the absence of SPM production. We designed a novel, high-dimensional spectral flow cytometry panel to target important immune cells and muscle progenitor cells involved during inflammation and muscle regeneration. Using this panel, we found that local

AT-RvD1 delivery at 3 days post VML significantly decreases neutrophil and pro-fibrotic macrophage infiltration along with increasing “non-classical” monocytes. Furthermore, at 7 days post VML there is a broad decrease in the persistence of immune cells with local AT-RvD1 delivery. We observe a decrease in fatty infiltration, decrease in non-muscle cell types between regenerating fibers, increase in myofiber regeneration and increase in vascular area with local AT-RvD1 delivery 14 days post VML. Finally, we compare the *in vivo* force production at 25 days post VML between untreated, vehicle control hydrogel, and pro-resolving hydrogel groups. Strikingly, local AT-RvD1 delivery results in a significant increase in quadricep force production via isometric torque analysis compared to other groups. Specifically, local AT-RvD1 recovers 85% of the muscle force compared to healthy controls while untreated VML injuries only generate 50% of the muscle force compared to healthy controls. To our knowledge, this is the most robust functional improvement seen in this pre-clinical VML model.

6.2 Further characterization of fibrosis with pro-resolving hydrogel treatment following VML injury.

Fibrosis is an important characterization of not only traumatic injury healing but many other injuries and chronic inflammatory conditions. Many fibrotic diseases present a large clinical burden and are characterized by the development of severe organ fibrosis without any obvious cause, such as idiopathic pulmonary fibrosis (IPF) and scleroderma. The ability of a therapeutic to decrease and especially reverse fibrosis holds immense clinical value. Focusing on our VML injury model, an important consideration is whether the pro-resolving hydrogel can have an effect on the fibrotic response. In collaboration with the Stanislav Emelianov and his lab, we are optimizing an ultrasound imaging technique that allows us to track the kinetic stiffness of tissue, and thus fibrosis, throughout the healing response (Fig. 50). This would open an avenue to exploring AT-RvD1 delivery at different timepoints and stages along the fibrotic healing response to VML in order to quantify whether we can improve, avoid or even reverse fibrosis once it begins to set in.

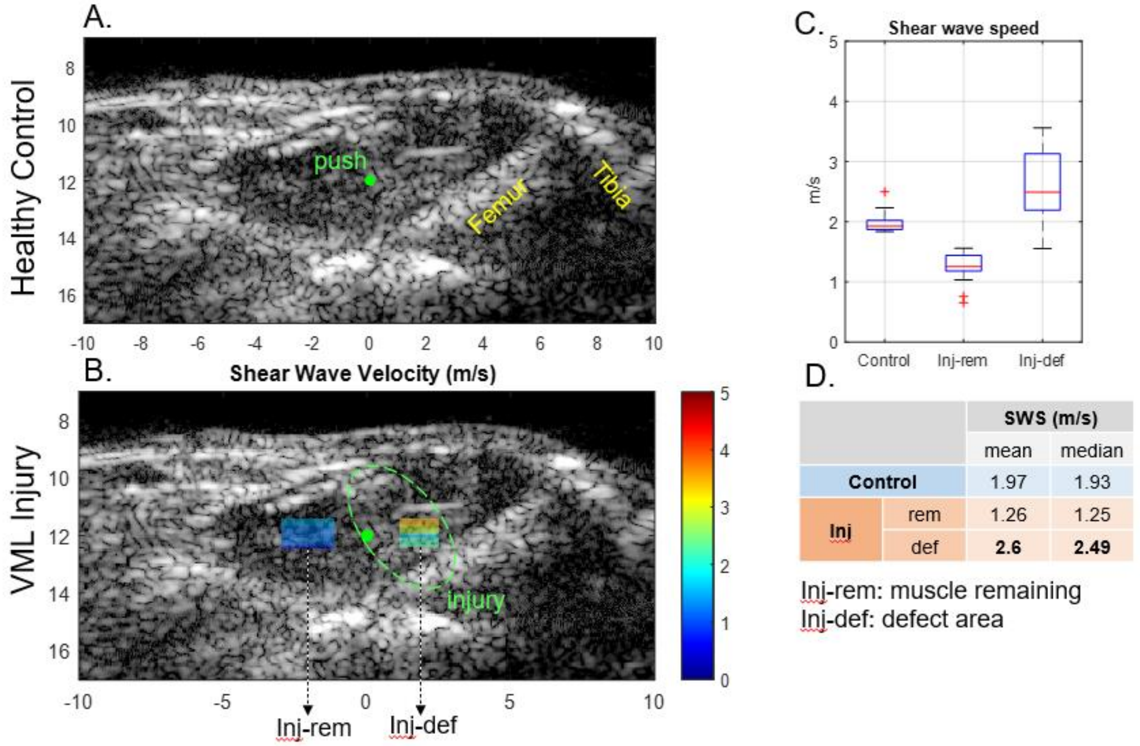

		SWS (m/s)	
		mean	median
Control		1.97	1.93
Inj	rem	1.26	1.25
	def	**2.6**	**2.49**

Inj-rem: muscle remaining
Inj-def: defect area

Figure 50. Monitoring muscle fibrosis of VML injury in mouse quadriceps muscle using ultrasound shear wave elasticity imaging (US-SWEI).
Ultrasound images of contralateral healthy control quadricep muscle (A) and critical VML injured muscle (B). Increased shear wave speed corresponds to a stiffer tissue. Quantification of shear wave speed indicates a higher speed in the defect area (inj-defect), a lower speed in the healthy control, and a lower speed in peri-injury area (inj-rem) (C and D). This indicates that stiffness is highest in the defect followed by healthy muscle and then followed by peri-injury area.

6.3 Extension of pro-resolving hydrogel platform to other regenerative medicine applications.

We characterize the ability of pro resolving hydrogels to improve microvascular remodeling in the skinfold window chamber model, improve wound healing in a model of skin transplant, and improve functional muscle recovery after non-healing VML injuries. These results establish the versatility of our therapeutic platform and indicate its usability in additional injury models. Some models of particular interest include promoting wound healing after diabetic non-healing wounds (a model that could exhibit similar features to non-healing muscle injuries), improving cardiac repair after infarct injury and directing palatal wound healing to prevent fistula formation after cleft palate repair. Furthermore, a comprehensive characterization of the pro-inflammatory lipid mediator and pro-resolving lipid mediator response after many of these injuries would be valuable information towards developing a tailored pro-resolving therapeutic for a specific injury context.

Furthermore, one particular interest of mine is the utilization of the pro-resolving hydrogel to prevent post-surgical inflammation, pain and fibrosis. Inflammatory reaction to orthopedic surgery is normal and often controlled with systemic anti-inflammatory drugs. However, in some cases there is a pathological stiffening of the joint or pathological fibrosis following surgery that leaves the patient with a loss of function rather than a gain of it. Particularly during repeated surgeries this issue becomes more common. Unfortunately, systemic anti-inflammatories are often not sufficient in controlling the inflammatory response or, if they are, they come with the collateral damage of inhibiting key regenerative pathways. Thus, the patient is left with no options. Given the fact that during surgery the patient injury is exposed and amenable to hydrogel implantation, the treatment of a surgery site with a pro-resolving hydrogel such as this one is very feasible. In fact, AT-RvD1, along with other SPMs, have been shown to effectively limit pain during certain injuries and inflammatory conditions [154]. Thus, the ability to not only limit the amount (or potentially eliminate) of post operative anti-inflammatory drugs but also control pain, effectively promote local resolution of inflammation, and avoid fibrosis or other common post-operative complications is potentially impactful. Furthermore, such a surgical wound recapitulates the sterile wound models that we have used herein to characterize this pro-resolving hydrogel platform.

6.4 Pro-resolving aptamer design to agonize pro-resolving receptor pathways.

SPMs are highly potent and efficacious endogenous ligands that have shown great potential in pre-clinical models of inflammation and injury. However, one of the main barriers to clinical translation is the fact that (1) due to their delicate physiochemical nature SPMs are highly prone to metabolic inactivation and (2) the routes to synthesize them are complex and costly [29]. Aptamers could be an attractive alternative in art due to their stability, sensitivity, specificity and low-cost production. Furthermore, they exhibit low immunogenicity and high tissue penetration. Aptamers are single-stranded DNA- or RNA- based oligonucleotides that bind target molecules with high affinity and specificity. Thus, aptamers can be designed and characterized to activate specific pro-resolving receptors such as the receptor of RvD1 ALX/FPR2 and other SPM receptors to promote inflammation resolution. Additionally, aptamers are easily modified so as to be readily incorporated into the backbone of hydrogel platforms to allow for sustained release or other release dynamics of interest.

REFERENCES

[1] K. Garg, C.L. Ward, B.J. Hurtgen, J.M. Wilken, D.J. Stinner, J.C. Wenke, J.G. Owens, B.T. Corona, Volumetric muscle loss: persistent functional deficits beyond frank loss of tissue, J Orthop Res 33(1) (2015) 40-6.

[2] Y.J. Choi, Y.J. Jun, D.Y. Kim, H.G. Yi, S.H. Chae, J. Kang, J. Lee, G. Gao, J.S. Kong, J. Jang, W.K. Chung, J.W. Rhie, D.W. Cho, A 3D cell printed muscle construct with tissue-derived bioink for the treatment of volumetric muscle loss, Biomaterials 206 (2019) 160-169.

[3] M. Quarta, M. Cromie, R. Chacon, J. Blonigan, V. Garcia, I. Akimenko, M. Hamer, P. Paine, M. Stok, J.B. Shrager, T.A. Rando, Bioengineered constructs combined with exercise enhance stem cell-mediated treatment of volumetric muscle loss, Nat Commun 8 (2017) 15613.

[4] N.J. Turner, J.S. Badylak, D.J. Weber, S.F. Badylak, Biologic scaffold remodeling in a dog model of complex musculoskeletal injury, J Surg Res 176(2) (2012) 490-502.

[5] B.D. Owens, J.F. Kragh, Jr., J. Macaitis, S.J. Svoboda, J.C. Wenke, Characterization of extremity wounds in Operation Iraqi Freedom and Operation Enduring Freedom, J Orthop Trauma 21(4) (2007) 254-7.

[6] E.J. Fitzgerald O'Connor, M. Vesely, P.J. Holt, K.G. Jones, M.M. Thompson, R.J. Hinchliffe, A systematic review of free tissue transfer in the management of non-traumatic lower extremity wounds in patients with diabetes, Eur J Vasc Endovasc Surg 41(3) (2011) 391-9.

[7] M. Klebuc, Z. Menn, Muscle flaps and their role in limb salvage, Methodist Debakey Cardiovasc J 9(2) (2013) 95-9.

[8] K. Garg, C.L. Ward, C.R. Rathbone, B.T. Corona, Transplantation of devitalized muscle scaffolds is insufficient for appreciable de novo muscle fiber regeneration after volumetric muscle loss injury, Cell Tissue Res 358(3) (2014) 857-73.

[9] B.M. Sicari, V. Agrawal, B.F. Siu, C.J. Medberry, C.L. Dearth, N.J. Turner, S.F. Badylak, A murine model of volumetric muscle loss and a regenerative medicine approach for tissue replacement, Tissue Eng Part A 18(19-20) (2012) 1941-8.

[10] C.A. Aguilar, S.M. Greising, A. Watts, S.M. Goldman, C. Peragallo, C. Zook, J. Larouche, B.T. Corona, Multiscale analysis of a regenerative therapy for treatment of volumetric muscle loss injury, Cell Death Discov 4 (2018) 33.

[11] B.T. Corona, X. Wu, C.L. Ward, J.S. McDaniel, C.R. Rathbone, T.J. Walters, The promotion of a functional fibrosis in skeletal muscle with volumetric muscle loss injury following the transplantation of muscle-ECM, Biomaterials 34(13) (2013) 3324-35.

[12] R. Matsuda, A. Nishikawa, H. Tanaka, Visualization of dystrophic muscle fibers in mdx mouse by vital staining with Evans blue: evidence of apoptosis in dystrophin-deficient muscle, J Biochem 118(5) (1995) 959-64.

[13] R.A. Fielding, T.J. Manfredi, W. Ding, M.A. Fiatarone, W.J. Evans, J.G. Cannon, Acute phase response in exercise. III. Neutrophil and IL-1 beta accumulation in skeletal muscle, Am J Physiol 265(1 Pt 2) (1993) R166-72.

[14] B. Uhl, Y. Vadlau, G. Zuchtriegel, K. Nekolla, K. Sharaf, F. Gaertner, S. Massberg, F. Krombach, C.A. Reichel, Aged neutrophils contribute to the first line of defense in the acute inflammatory response, Blood 128(19) (2016) 2327-2337.

[15] J.G. Tidball, Regulation of muscle growth and regeneration by the immune system, Nat Rev Immunol 17(3) (2017) 165-178.

[16] D.R. Lemos, F. Babaeijandaghi, M. Low, C.K. Chang, S.T. Lee, D. Fiore, R.H. Zhang, A. Natarajan, S.A. Nedospasov, F.M. Rossi, Nilotinib reduces muscle fibrosis in chronic muscle injury by promoting TNF-mediated apoptosis of fibro/adipogenic progenitors, Nat Med 21(7) (2015) 786-94.

[17] M.L. Novak, E.M. Weinheimer-Haus, T.J. Koh, Macrophage activation and skeletal muscle healing following traumatic injury, J Pathol 232(3) (2014) 344-55.

[18] J. Tonkin, L. Temmerman, R.D. Sampson, E. Gallego-Colon, L. Barberi, D. Bilbao, M.D. Schneider, A. Musaro, N. Rosenthal, Monocyte/Macrophage-derived IGF-1 Orchestrates Murine Skeletal Muscle Regeneration and Modulates Autocrine Polarization, Mol Ther 23(7) (2015) 1189-1200.

[19] B.J. Hurtgen, C.L. Ward, K. Garg, B.E. Pollot, S.M. Goldman, T.O. McKinley, J.C. Wenke, B.T. Corona, Severe muscle trauma triggers heightened and prolonged local musculoskeletal inflammation and impairs adjacent tibia fracture healing, J Musculoskelet Neuronal Interact 16(2) (2016) 122-34.

[20] T.T. Braga, J.S. Agudelo, N.O. Camara, Macrophages During the Fibrotic Process: M2 as Friend and Foe, Front Immunol 6 (2015) 602.

[21] B. Chazaud, Inflammation and Skeletal Muscle Regeneration: Leave It to the Macrophages!, Trends Immunol 41(6) (2020) 481-492.

[22] C.N. Serhan, Treating inflammation and infection in the 21st century: new hints from decoding resolution mediators and mechanisms, FASEB J 31(4) (2017) 1273-1288.

[23] I. Tabas, C.K. Glass, Anti-inflammatory therapy in chronic disease: challenges and opportunities, Science 339(6116) (2013) 166-72.

[24] C.N. Serhan, Pro-resolving lipid mediators are leads for resolution physiology, Nature 510(7503) (2014) 92-101.

[25] R.J. Flower, Prostaglandins, bioassay and inflammation, Br J Pharmacol 147 Suppl 1 (2006) S182-92.

[26] B.D. Levy, C.B. Clish, B. Schmidt, K. Gronert, C.N. Serhan, Lipid mediator class switching during acute inflammation: signals in resolution, Nat Immunol 2(7) (2001) 612-9.

[27] J. Dalli, C.N. Serhan, Specific lipid mediator signatures of human phagocytes: microparticles stimulate macrophage efferocytosis and pro-resolving mediators, Blood 120(15) (2012) e60-72.

[28] J. Dalli, C. Serhan, Macrophage Proresolving Mediators-the When and Where, Microbiol Spectr 4(3) (2016).

[29] J. Park, C.J. Langmead, D.M. Riddy, New Advances in Targeting the Resolution of Inflammation: Implications for Specialized Pro-Resolving Mediator GPCR Drug Discovery, ACS Pharmacol Transl Sci 3(1) (2020) 88-106.

[30] N. Chiang, C.N. Serhan, Specialized pro-resolving mediator network: an update on production and actions, Essays Biochem 64(3) (2020) 443-462.

[31] N. Chiang, C.N. Serhan, Structural elucidation and physiologic functions of specialized pro-resolving mediators and their receptors, Mol Aspects Med 58 (2017) 114-129.

[32] Y.P. Sun, S.F. Oh, J. Uddin, R. Yang, K. Gotlinger, E. Campbell, S.P. Colgan, N.A. Petasis, C.N. Serhan, Resolvin D1 and its aspirin-triggered 17R epimer. Stereochemical assignments, anti-inflammatory properties, and enzymatic inactivation, J Biol Chem 282(13) (2007) 9323-9334.

[33] J.Y. Lee, S.H. Han, M.H. Park, I.S. Song, M.K. Choi, E. Yu, C.M. Park, H.J. Kim, S.H. Kim, E.H. Schuchman, H.K. Jin, J.S. Bae, N-AS-triggered SPMs are direct regulators of microglia in a model of Alzheimer's disease, Nat Commun 11(1) (2020) 2358.

[34] S. Krishnamoorthy, A. Recchiuti, N. Chiang, S. Yacoubian, C.H. Lee, R. Yang, N.A. Petasis, C.N. Serhan, Resolvin D1 binds human phagocytes with evidence for proresolving receptors, Proc Natl Acad Sci U S A 107(4) (2010) 1660-5.

[35] M.M. Gilligan, A. Gartung, M.L. Sulciner, P.C. Norris, V.P. Sukhatme, D.R. Bielenberg, S. Huang, M.W. Kieran, C.N. Serhan, D. Panigrahy, Aspirin-triggered proresolving mediators stimulate resolution in cancer, Proc Natl Acad Sci U S A 116(13) (2019) 6292-6297.

[36] M.B. Goldring, M. Otero, Inflammation in osteoarthritis, Curr Opin Rheumatol 23(5) (2011) 471-8.

[37] C.A. Dinarello, A. Simon, J.W. van der Meer, Treating inflammation by blocking interleukin-1 in a broad spectrum of diseases, Nat Rev Drug Discov 11(8) (2012) 633-52.

[38] H. Suleyman, B. Demircan, Y. Karagoz, Anti-inflammatory and side effects of cyclooxygenase inhibitors, Pharmacol Rep 59(3) (2007) 247-58.

[39] J.L. Goldstein, B. Cryer, Gastrointestinal injury associated with NSAID use: a case study and review of risk factors and preventative strategies, Drug Healthc Patient Saf 7 (2015) 31-41.

[40] A.S. Tarnawski, M.K. Jones, Inhibition of angiogenesis by NSAIDs: molecular mechanisms and clinical implications, J Mol Med (Berl) 81(10) (2003) 627-36.

[41] A.E. Barden, M. Moghaddami, E. Mas, M. Phillips, L.G. Cleland, T.A. Mori, Specialised pro-resolving mediators of inflammation in inflammatory arthritis, Prostaglandins Leukot Essent Fatty Acids 107 (2016) 24-9.

[42] H.S. Jonasdottir, H. Brouwers, J.C. Kwekkeboom, H.M.J. van der Linden, T. Huizinga, M. Kloppenburg, R.E.M. Toes, M. Giera, A. Ioan-Facsinay, Targeted lipidomics reveals activation of resolution pathways in knee osteoarthritis in humans, Osteoarthritis Cartilage 25(7) (2017) 1150-1160.

[43] G. Fredman, J. Hellmann, J.D. Proto, G. Kuriakose, R.A. Colas, B. Dorweiler, E.S. Connolly, R. Solomon, D.M. Jones, E.J. Heyer, M. Spite, I. Tabas, An imbalance between specialized pro-resolving lipid mediators and pro-inflammatory leukotrienes promotes instability of atherosclerotic plaques, Nat Commun 7 (2016) 12859.

[44] O. Kowal-Bielecka, K. Kowal, O. Distler, J. Rojewska, A. Bodzenta-Lukaszyk, B.A. Michel, R.E. Gay, S. Gay, S. Sierakowski, Cyclooxygenase- and lipoxygenase-derived eicosanoids in bronchoalveolar lavage fluid from patients with scleroderma lung disease: an imbalance between proinflammatory and antiinflammatory lipid mediators, Arthritis Rheum 52(12) (2005) 3783-91.

[45] A.R. Sun, X. Wu, B. Liu, Y. Chen, C.W. Armitage, A. Kollipara, R. Crawford, K.W. Beagley, X. Mao, Y. Xiao, I. Prasadam, Pro-resolving lipid mediator ameliorates obesity induced osteoarthritis by regulating synovial macrophage polarisation, Sci Rep 9(1) (2019) 426.

[46] L. Habouri, F.E. El Mansouri, Y. Ouhaddi, B. Lussier, J.P. Pelletier, J. Martel-Pelletier, M. Benderdour, H. Fahmi, Deletion of 12/15-lipoxygenase accelerates the development of aging-associated and instability-induced osteoarthritis, Osteoarthritis Cartilage 25(10) (2017) 1719-1728.

[47] J. Huang, J.J. Burston, L. Li, S. Ashraf, P.I. Mapp, A.J. Bennett, S. Ravipati, P. Pousinis, D.A. Barrett, B.E. Scammell, V. Chapman, Targeting the D Series Resolvin Receptor System for the Treatment of Osteoarthritis Pain, Arthritis Rheumatol 69(5) (2017) 996-1008.

[48] J. Dalli, N. Chiang, C.N. Serhan, Identification of 14-series sulfido-conjugated mediators that promote resolution of infection and organ protection, Proc Natl Acad Sci U S A 111(44) (2014) E4753-61.

[49] J.F. Markworth, L.A. Brown, E. Lim, J.A. Castor-Macias, J. Larouche, P.C.D. Macpherson, C. Davis, C.A. Aguilar, K.R. Maddipati, S.V. Brooks, Metabolipidomic profiling reveals an age-related deficiency of skeletal muscle pro-resolving mediators that contributes to maladaptive tissue remodeling, Aging Cell 20(6) (2021) e13393.

[50] N. Giannakis, B.E. Sansbury, A. Patsalos, T.T. Hays, C.O. Riley, X. Han, M. Spite, L. Nagy, Dynamic changes to lipid mediators support transitions among macrophage subtypes during muscle regeneration, Nat Immunol 20(5) (2019) 626-636.

[51] J. Dort, Z. Orfi, P. Fabre, T. Molina, T.C. Conte, K. Greffard, O. Pellerito, J.F. Bilodeau, N.A. Dumont, Resolvin-D2 targets myogenic cells and improves muscle regeneration in Duchenne muscular dystrophy, Nat Commun 12(1) (2021) 6264.

[52] J.F. Markworth, L.A. Brown, E. Lim, C. Floyd, J. Larouche, J.A. Castor-Macias, K.B. Sugg, D.C. Sarver, P.C. Macpherson, C. Davis, C.A. Aguilar, K.R. Maddipati, S.V. Brooks, Resolvin D1 supports skeletal myofiber regeneration via actions on myeloid and muscle stem cells, JCI Insight 5(18) (2020).

[53] G. Juban, B. Chazaud, Efferocytosis during Skeletal Muscle Regeneration, Cells 10(12) (2021).

[54] R. Huang, L. Vi, X. Zong, G.S. Baht, Maresin 1 resolves aged-associated macrophage inflammation to improve bone regeneration, FASEB J 34(10) (2020) 13521-13532.

[55] S. Hong, T.F. Porter, Y. Lu, S.F. Oh, P.S. Pillai, C.N. Serhan, Resolvin E1 metabolome in local inactivation during inflammation-resolution, J Immunol 180(5) (2008) 3512-9.

[56] M. Arita, S.F. Oh, T. Chonan, S. Hong, S. Elangovan, Y.P. Sun, J. Uddin, N.A. Petasis, C.N. Serhan, Metabolic inactivation of resolvin E1 and stabilization of its anti-inflammatory actions, J Biol Chem 281(32) (2006) 22847-54.

[57] C.N. Serhan, J. Savill, Resolution of inflammation: the beginning programs the end, Nat Immunol 6(12) (2005) 1191-7.

[58] L.V. Norling, M. Spite, R. Yang, R.J. Flower, M. Perretti, C.N. Serhan, Cutting edge: Humanized nano-proresolving medicines mimic inflammation-resolution and enhance wound healing, J Immunol 186(10) (2011) 5543-7.

[59] K.D. Lance, A. Chatterjee, B. Wu, G. Mottola, H. Nuhn, P.P. Lee, B.E. Sansbury, M. Spite, T.A. Desai, M.S. Conte, Unidirectional and sustained delivery of the proresolving lipid mediator resolvin D1 from a biodegradable thin film device, J Biomed Mater Res A 105(1) (2017) 31-41.

[60] B. Wu, E.C. Werlin, M. Chen, G. Mottola, A. Chatterjee, K.D. Lance, D.A. Bernards, B.E. Sansbury, M. Spite, T.A. Desai, M.S. Conte, Perivascular delivery of resolvin D1 inhibits neointimal hyperplasia in a rabbit vein graft model, J Vasc Surg 68(6S) (2018) 188S-200S e4.

[61] M.C.P. Sok, M.C. Tria, C.E. Olingy, C.L. San Emeterio, E.A. Botchwey, Aspirin-Triggered Resolvin D1-modified materials promote the accumulation of pro-regenerative immune cell subsets and enhance vascular remodeling, Acta Biomater 53 (2017) 109-122.

[62] M. Quiros, D. Feier, D. Birkl, R. Agarwal, D.W. Zhou, A.J. Garcia, C.A. Parkos, A. Nusrat, Resolvin E1 is a pro-repair molecule that promotes intestinal epithelial wound healing, Proc Natl Acad Sci U S A 117(17) (2020) 9477-9482.

[63] A.A. Dravid, M.D. K, S. Agarwal, R. Agarwal, Resolvin D1-loaded nanoliposomes promote M2 macrophage polarization and are effective in the treatment of osteoarthritis, Bioeng Transl Med 7(2) (2022) e10281.

[64] C. Rosales, Neutrophil: A Cell with Many Roles in Inflammation or Several Cell Types?, Front Physiol 9 (2018) 113.

[65] J.F. Deniset, P. Kubes, Neutrophil heterogeneity: Bona fide subsets or polarization states?, J Leukoc Biol 103(5) (2018) 829-838.

[66] E. Kolaczkowska, P. Kubes, Neutrophil recruitment and function in health and inflammation, Nat Rev Immunol 13(3) (2013) 159-75.

[67] T.N. Mayadas, X. Cullere, C.A. Lowell, The multifaceted functions of neutrophils, Annu Rev Pathol 9 (2014) 181-218.

[68] G.B. Segel, M.W. Halterman, M.A. Lichtman, The paradox of the neutrophil's role in tissue injury, J Leukoc Biol 89(3) (2011) 359-72.

[69] Y. Gong, D.R. Koh, Neutrophils promote inflammatory angiogenesis via release of preformed VEGF in an in vivo corneal model, Cell Tissue Res 339(2) (2010) 437-48.

[70] M. Liu, K. Chen, T. Yoshimura, Y. Liu, W. Gong, Y. Le, J.L. Gao, J. Zhao, J.M. Wang, A. Wang, Formylpeptide receptors mediate rapid neutrophil mobilization to accelerate wound healing, PLoS One 9(6) (2014) e90613.

[71] G. Christoffersson, E. Vagesjo, J. Vandooren, M. Liden, S. Massena, R.B. Reinert, M. Brissova, A.C. Powers, G. Opdenakker, M. Phillipson, VEGF-A recruits a proangiogenic MMP-9-delivering neutrophil subset that induces angiogenesis in transplanted hypoxic tissue, Blood 120(23) (2012) 4653-62.

[72] M.J. Zhang, B.E. Sansbury, J. Hellmann, J.F. Baker, L. Guo, C.M. Parmer, J.C. Prenner, D.J. Conklin, A. Bhatnagar, M.A. Creager, M. Spite, Resolvin D2 enhances postischemic revascularization while resolving inflammation, Circulation 134(9) (2016) 666-680.

[73] H.T. Maecker, J.P. McCoy, R. Nussenblatt, Standardizing immunophenotyping for the Human Immunology Project, Nat Rev Immunol 12(3) (2012) 191-200.

[74] J.R. Krieger, M.E. Ogle, J. McFaline-Figueroa, C.E. Segar, J.S. Temenoff, E.A. Botchwey, Spatially localized recruitment of anti-inflammatory monocytes by SDF-1alpha-releasing hydrogels enhances microvascular network remodeling, Biomaterials 77 (2016) 280-90.

[75] B. Anchang, T.D. Hart, S.C. Bendall, P. Qiu, Z. Bjornson, M. Linderman, G.P. Nolan, S.K. Plevritis, Visualization and cellular hierarchy inference of single-cell data using SPADE, Nat Protoc 11(7) (2016) 1264-79.

[76] E. Becht, L. McInnes, J. Healy, C.A. Dutertre, I.W.H. Kwok, L.G. Ng, F. Ginhoux, E.W. Newell, Dimensionality reduction for visualizing single-cell data using UMAP, Nat Biotechnol (2018).

[77] P. Qiu, E.F. Simonds, S.C. Bendall, K.D. Gibbs, Jr., R.V. Bruggner, M.D. Linderman, K. Sachs, G.P. Nolan, S.K. Plevritis, Extracting a cellular hierarchy from high-dimensional cytometry data with SPADE, Nat Biotechnol 29(10) (2011) 886-91.

[78] B.N. Brown, B.M. Sicari, S.F. Badylak, Rethinking regenerative medicine: a macrophage-centered approach, Front Immunol 5 (2014) 510.

[79] H. Li, B. Shi, Tolerogenic dendritic cells and their applications in transplantation, Cell Mol Immunol 12(1) (2015) 24-30.

[80] R. Grieshaber-Bouyer, P.A. Nigrovic, Neutrophil Heterogeneity as Therapeutic Opportunity in Immune-Mediated Disease, Front Immunol 10 (2019) 346.

[81] S. Tazzyman, C.E. Lewis, C. Murdoch, Neutrophils: key mediators of tumour angiogenesis, Int J Exp Pathol 90(3) (2009) 222-31.

[82] K.L. Wofford, B.S. Singh, D.K. Cullen, K.L. Spiller, Biomaterial-mediated reprogramming of monocytes via microparticle phagocytosis for sustained modulation of macrophage phenotype, Acta Biomater 101 (2020) 237-248.

[83] S.A. Ballestas, T.C. Turner, A. Kamalakar, Y.C. Stephenson, N.J. Willett, S.L. Goudy, E.A. Botchwey, Improving hard palate wound healing using immune modulatory autotherapies, Acta Biomater 91 (2019) 209-219.

[84] K. Sadtler, B.W. Allen, K. Estrellas, F. Housseau, D.M. Pardoll, J.H. Elisseeff, The Scaffold Immune Microenvironment: Biomaterial-Mediated Immune Polarization in Traumatic and Nontraumatic Applications<sup/>, Tissue Eng Part A 23(19-20) (2017) 1044-1053.

[85] S. Palit, C. Heuser, G.P. de Almeida, F.J. Theis, C.E. Zielinski, Meeting the Challenges of High-Dimensional Single-Cell Data Analysis in Immunology, Front Immunol 10 (2019) 1515.

[86] C. Trapnell, D. Cacchiarelli, J. Grimsby, P. Pokharel, S. Li, M. Morse, N.J. Lennon, K.J. Livak, T.S. Mikkelsen, J.L. Rinn, The dynamics and regulators of cell fate decisions are revealed by pseudotemporal ordering of single cells, Nat Biotechnol 32(4) (2014) 381-386.

[87] D. Ramskold, S. Luo, Y.C. Wang, R. Li, Q. Deng, O.R. Faridani, G.A. Daniels, I. Khrebtukova, J.F. Loring, L.C. Laurent, G.P. Schroth, R. Sandberg, Full-length mRNA-Seq from single-cell levels of RNA and individual circulating tumor cells, Nat Biotechnol 30(8) (2012) 777-82.

[88] L.G. Ng, R. Ostuni, A. Hidalgo, Heterogeneity of neutrophils, Nat Rev Immunol 19(4) (2019) 255-265.

[89] J.M. Adrover, J.A. Nicolas-Avila, A. Hidalgo, Aging: A Temporal Dimension for Neutrophils, Trends Immunol 37(5) (2016) 334-345.

[90] G.E. Majai, P. Gogolak, M. Toth, J. Hodrea, D. Horvath, L. Fesus, E. Rajnavolgyi, A. Bacsi, Autologous apoptotic neutrophils inhibit inflammatory cytokine secretion by human dendritic cells, but enhance Th1 responses, FEBS Open Bio 10(8) (2020) 1492-1502.

[91] N. Maimon, Z.Z. Zamir, P. Kalkar, O. Zeytuni-Timor, S. Schif-Zuck, S. Larisch, A. Ariel, The pro-apoptotic ARTS protein induces neutrophil apoptosis, efferocytosis, and macrophage reprogramming to promote resolution of inflammation, Apoptosis 25(7-8) (2020) 558-573.

[92] K. Garg, C.L. Ward, B.J. Hurtgen, J.M. Wilken, D.J. Stinner, J.C. Wenke, J.G. Owens, B.T. Corona, Volumetric Muscle Loss : Persistent Functional Deficits Beyond Frank Loss of Tissue, (January) (2015) 40-46.

[93] B.T. Corona, J.C. Rivera, J.G. Owens, J.C. Wenke, C.R. Rathbone, Volumetric muscle loss leads to permanent disability following extremity trauma, Journal of Rehabilitation Research and Development 52(7) (2015) 785-792.

[94] K. Sadtler, K. Estrellas, B.W. Allen, M.T. Wolf, H. Fan, A.J. Tam, C.H. Patel, B.S. Luber, H. Wang, K.R. Wagner, J.D. Powell, F. Housseau, D.M. Pardoll, J.H. Elisseeff, Developing a pro-regenerative biomaterial scaffold microenvironment requires T helper 2 cells, Science 352(6283) (2016) 366-70.

[95] M.E. Carnes, G.D. Pins, Skeletal Muscle Tissue Engineering: Biomaterials-Based Strategies for the Treatment of Volumetric Muscle Loss, Bioengineering (Basel) 7(3) (2020).

[96] S. Das, K.D. Browne, F.A. Laimo, J.C. Maggiore, M.C. Hilman, H. Kaisaier, C.A. Aguilar, Z.S. Ali, F. Mourkioti, D.K. Cullen, Pre-innervated tissue-engineered muscle promotes a pro-regenerative microenvironment following volumetric muscle loss, Commun Biol 3(1) (2020) 330.

[97] G. Krischak, The effects of non-steroidal anti-inflammatory drug application on incisional wound healing in rats, (March) (2007).

[98] J. Larouche, S.M. Greising, B.T. Corona, C.A. Aguilar, Robust inflammatory and fibrotic signaling following volumetric muscle loss: A barrier to muscle regeneration comment, Cell Death and Disease 9(3) (2018) 18-20.

[99] B. Chazaud, Inflammation and Skeletal Muscle Regeneration: Leave It to the Macrophages!, Trends in Immunology 41(6) (2020) 481-492.

[100] M.L. Novak, E.M. Weinheimer-Haus, T.J. Koh, Macrophage activation and skeletal muscle healing following traumatic injury, Journal of Pathology 232(3) (2014) 344-355.

[101] B. Malecova, S. Gatto, U. Etxaniz, M. Passafaro, A. Cortez, C. Nicoletti, L. Giordani, A. Torcinaro, M. De Bardi, S. Bicciato, F. De Santa, L. Madaro, P.L. Puri, Dynamics of cellular states of fibro-adipogenic progenitors during myogenesis and muscular dystrophy, Nature Communications 9(1) (2018).

[102] W.-h. Su, M.-h. Cheng, W.-l. Lee, T.-s. Tsou, W.-h. Chang, C.-s. Chen, P.-h. Wang, Nonsteroidal Anti-Inflammatory Drugs for Wounds : Pain Relief or Excessive Scar Formation ?, 2010 (2010).

[103] A.S. Tarnawski, M.K. Jones, Inhibition of angiogenesis by NSAIDs: Molecular mechanisms and clinical implications, Journal of Molecular Medicine 81(10) (2003) 627-636.

[104] C.D. Funk, Prostaglandins and leukotrienes: Advances in eicosanoid biology, Science 294(5548) (2001) 1871-1875.

[105] J. Dort, Z. Orfi, P. Fabre, T. Molina, T.C. Conte, K. Greffard, O. Pellerito, J.-F. Bilodeau, N.A. Dumont, Resolvin-D2 targets myogenic cells and improves muscle regeneration in Duchenne muscular dystrophy, Nature Communications 12(1) (2021) 1-17.

[106] N. Giannakis, B.E. Sansbury, A. Patsalos, T.T. Hays, C.O. Riley, X. Han, M. Spite, L. Nagy, Dynamic changes to lipid mediators support transitions among macrophage subtypes during muscle regeneration, Nature Immunology (2019).

[107] R.J. Flower, Prostaglandins, bioassay and inflammation, British Journal of Pharmacology 147(SUPPL. 1) (2006) 182-192.

[108] C.D. Buckley, D.W. Gilroy, C.N. Serhan, Proresolving lipid mediators and mechanisms in the resolution of acute inflammation, Immunity 40(3) (2014) 315-327.

[109] B.D. Levy, C.B. Clish, B. Schmidt, K. Gronert, C.N. Serhan, Lipid mediator class switching during acute inflammation: Signals in resolution, Nature Immunology 2(7) (2001) 612-619.

[110] J. Dalli, C.N. Serhan, Specific lipid mediator signatures of human phagocytes: Microparticles stimulate macrophage efferocytosis and pro-resolving mediators, Blood 120(15) (2012) 60-72.

[111] J. Dalli, C. Serhan, Macrophage Proresolving Mediators — the When and Where, (2016).

[112] M. Shang, F. Cappellesso, R. Amorim, J. Serneels, F. Virga, G. Eelen, S. Carobbio, M.Y. Rincon, P. Maechler, K. De Bock, P.C. Ho, M. Sandri, B. Ghesquiere, P. Carmeliet, M. Di Matteo, E. Berardi, M. Mazzone, Macrophage-derived glutamine boosts satellite cells and muscle regeneration, Nature 587(7835) (2020) 626-631.

[113] Y.P. Sun, S.F. Oh, J. Uddin, R. Yang, K. Gotlinger, E. Campbell, S.P. Colgan, N.A. Petasis, C.N. Serhan, Resolvin D1 and its aspirin-triggered 17R epimer: Stereochemical assignments, anti-inflammatory properties, and enzymatic inactivation, Journal of Biological Chemistry 282(13) (2007) 9323-9334.

[114] V.K. Yellepeddi, O.J. Baker, Predictive modeling of aspirin-triggered resolvin D1 pharmacokinetics for the study of Sjögren ' s syndrome, (August 2019) (2020).

[115] M.M. Gilligan, A. Gartung, M.L. Sulciner, P.C. Norris, V.P. Sukhatme, D.R. Bielenberg, S. Huang, M.W. Kieran, C.N. Serhan, D. Panigrahy, Aspirin-triggered proresolving mediators

stimulate resolution in cancer, Proceedings of the National Academy of Sciences of the United States of America 116(13) (2019) 6292-6297.

[116] C.N. Serhan, Treating inflammation and infection in the 21st century: New hints from decoding resolution mediators and mechanisms, FASEB Journal 31(4) (2017) 1273-1288.

[117] T.C. Turner, M.C.P. Sok, L.A. Hymel, F.S. Pittman, W.Y. York, Q.D. Mac, S. Vyshnya, H.S. Lim, G.A. Kwong, P. Qiu, E.A. Botchwey, Harnessing lipid signaling pathways to target specialized pro-angiogenic neutrophil subsets for regenerative immunotherapy, Science Advances 6(44) (2020) 1-14.

[118] M.C.P. Sok, N. Baker, C. McClain, H.S. Lim, T. Turner, L. Hymel, M. Ogle, C. Olingy, J.I. Palacios, J.R. Garcia, K. Srithar, A.J. García, P. Qiu, E.A. Botchwey, Dual delivery of IL-10 and AT-RvD1 from PEG hydrogels polarize immune cells towards pro-regenerative phenotypes, Biomaterials 268(March 2020) (2021).

[119] M.C.P. Sok, N. Baker, C. McClain, H.S. Lim, T. Turner, L. Hymel, M. Ogle, C. Olingy, J.I. Palacios, J.R. Garcia, K. Srithar, A.J. Garcia, P. Qiu, E.A. Botchwey, Dual delivery of IL-10 and AT-RvD1 from PEG hydrogels polarize immune cells towards pro-regenerative phenotypes, Biomaterials 268 (2021) 120475.

[120] E.A. Phelps, N.O. Enemchukwu, V.F. Fiore, J.C. Sy, N. Murthy, T.A. Sulchek, T.H. Barker, A.J. Garcia, Maleimide cross-linked bioactive PEG hydrogel exhibits improved reaction kinetics and cross-linking for cell encapsulation and in situ delivery, Adv Mater 24(1) (2012) 64-70, 2.

[121] W.M. Han, M. Mohiuddin, S.E. Anderson, A.J. Garcia, Y.C. Jang, Co-delivery of Wnt7a and muscle stem cells using synthetic bioadhesive hydrogel enhances murine muscle regeneration and cell migration during engraftment, Acta Biomater 94 (2019) 243-252.

[122] T.C. Turner, M.C.P. Sok, L.A. Hymel, F.S. Pittman, W.Y. York, Q.D. Mac, S. Vyshnya, H.S. Lim, G.A. Kwong, P. Qiu, E.A. Botchwey, Harnessing lipid signaling pathways to target specialized pro-angiogenic neutrophil subsets for regenerative immunotherapy, Sci Adv 6(44) (2020).

[123] K. Ley, H.M. Hoffman, P. Kubes, M.A. Cassatella, A. Zychlinsky, C.C. Hedrick, S.D. Catz, Neutrophils: New insights and open questions, Sci Immunol 3(30) (2018).

[124] E. Frangou, D. Vassilopoulos, J. Boletis, D.T. Boumpas, An emerging role of neutrophils and NETosis in chronic inflammation and fibrosis in systemic lupus erythematosus (SLE) and ANCA-associated vasculitides (AAV): Implications for the pathogenesis and treatment, Autoimmun Rev 18(8) (2019) 751-760.

[125] M.A. Fernandez-Yague, L.A. Hymel, C.E. Olingy, C. McClain, M.E. Ogle, J.R. Garcia, D. Minshew, S. Vyshnya, H.S. Lim, P. Qiu, A.J. Garcia, E.A. Botchwey, Analyzing immune response to engineered hydrogels by hierarchical clustering of inflammatory cell subsets, Sci Adv 8(8) (2022) eabd8056.

[126] K. Forouhesh Tehrani, E.G. Pendleton, W.M. Southern, J.A. Call, L.J. Mortensen, Spatial frequency metrics for analysis of microscopic images of musculoskeletal tissues, Connect Tissue Res 62(1) (2021) 4-14.

[127] M. Klebuc, Z. Menn, M. D, Muscle flaps and their role in limb salvage, (D) (2013) 95-98.

[128] S. Population, AN ANALYSIS OF OUTCOMES OF RECONSTRUCTION OR AMPUTATION OF LEG-THREATENING INJURIES, 347(24) (2002) 1924-1931.

[129] B.T. Corona, X. Wu, C.L. Ward, J.S. McDaniel, C.R. Rathbone, T.J. Walters, The promotion of a functional fi brosis in skeletal muscle with volumetric muscle loss injury following the transplantation of muscle-ECM, Biomaterials 34(13) (2013) 3324-3335.

[130] K. Garg, C.L. Ward, C.R. Rathbone, B.T. Corona, Transplantation of devitalized muscle scaffolds is insufficient for appreciable de novo muscle fiber regeneration after volumetric muscle loss injury, (2014) 857-873.

[131] S.M. Greising, J.C. Rivera, S.M. Goldman, A. Watts, C.A. Aguilar, B.T. Corona, Unwavering Pathobiology of Volumetric Muscle Loss Injury, Scientific Reports 7(1) (2017) 1-14.

[132] M. Quarta, M. Cromie, R. Chacon, J. Blonigan, V. Garcia, I. Akimenko, M. Hamer, P. Paine, M. Stok, J.B. Shrager, T.A. Rando, Bioengineered constructs combined with exercise enhance stem cell-mediated treatment of volumetric muscle loss, Nature Communications 8 (2017) 1-17.

[133] J. Gilbert-Honick, W. Grayson, Vascularized and Innervated Skeletal Muscle Tissue Engineering, Advanced Healthcare Materials 9(1) (2020) 1-27.

[134] S.M. Greising, B.T. Corona, C. McGann, J.K. Frankum, G.L. Warren, Therapeutic Approaches for Volumetric Muscle Loss Injury: A Systematic Review and Meta-Analysis, Tissue Engineering - Part B: Reviews 25(6) (2019) 510-525.

[135] C.N. Serhan, J. Savill, Resolution of inflammation: The beginning programs the end, Nature Immunology 6(12) (2005) 1191-1197.

[136] A.E. Coutinho, K.E. Chapman, The anti-inflammatory and immunosuppressive effects of glucocorticoids , recent developments and mechanistic insights, Molecular and Cellular Endocrinology 335(1) (2011) 2-13.

[137] W.M. Han, S.E. Anderson, M. Mohiuddin, D. Barros, S.A. Nakhai, E. Shin, I.F. Amaral, A.P. Pêgo, A.J. García, Y.C. Jang, Synthetic matrix enhances transplanted satellite cell engraftment in dystrophic and aged skeletal muscle with comorbid trauma, Science Advances 4(8) (2018).

[138] G. Sollberger, D.O. Tilley, A. Zychlinsky, Neutrophil Extracellular Traps: The Biology of Chromatin Externalization, Developmental Cell 44(5) (2018) 542-553.

[139] L.A. Hymel, M.E. Ogle, S.E. Anderson, C.L. San Emeterio, T.C. Turner, W.Y. York, A.Y. Liu, C.E. Olingy, S. Sridhar, H.S. Lim, T. Sulchek, P. Qiu, Y.C. Jang, N.J. Willett, E.A. Botchwey,

Modulating local S1P receptor signaling as a regenerative immunotherapy after volumetric muscle loss injury, J Biomed Mater Res A 109(5) (2021) 695-712.

[140] C.L. San Emeterio, L.A. Hymel, T.C. Turner, M.E. Ogle, E.G. Pendleton, W.Y. York, C.E. Olingy, A.Y. Liu, H.S. Lim, T.A. Sulchek, G.L. Warren, L.J. Mortensen, P. Qiu, Y.C. Jang, N.J. Willett, E.A. Botchwey, Nanofiber-Based Delivery of Bioactive Lipids Promotes Pro-regenerative Inflammation and Enhances Muscle Fiber Growth After Volumetric Muscle Loss, Front Bioeng Biotechnol 9 (2021) 650289.

[141] P. Qiu, E.F. Simonds, S.C. Bendall, K.D. Gibbs, R.V. Bruggner, M.D. Linderman, K. Sachs, G.P. Nolan, S.K. Plevritis, Extracting a cellular hierarchy from high-dimensional cytometry data with SPADE, Nature Biotechnology 29(10) (2011) 886-893.

[142] K.F. Tehrani, C.V. Latchoumane, W.M. Southern, E.G. Pendleton, A. Maslesa, L. Karumbaiah, J.A. Call, L.J. Mortensen, Five-dimensional two-photon volumetric microscopy of in-vivo dynamic activities using liquid lens remote focusing, Biomed Opt Express 10(7) (2019) 3591-3604.

[143] S.E. Anderson, W.M. Han, V. Srinivasa, M. Mohiuddin, M.A. Ruehle, J.Y. Moon, E. Shin, C.L. San Emeterio, M.E. Ogle, E.A. Botchwey, N.J. Willett, Y.C. Jang, Determination of a Critical Size Threshold for Volumetric Muscle Loss in the Mouse Quadriceps, Tissue Eng Part C Methods 25(2) (2019) 59-70.

[144] M. Wehling-Henricks, M.C. Jordan, T. Gotoh, W.W. Grody, K.P. Roos, J.G. Tidball, Arginine metabolism by macrophages promotes cardiac and muscle fibrosis in mdx muscular dystrophy, PLoS One 5(5) (2010) e10763.

[145] G.Q. Wallace, E.M. McNally, Mechanisms of muscle degeneration, regeneration, and repair in the muscular dystrophies, Annu Rev Physiol 71 (2009) 37-57.

[146] J.P. Nolan, D. Condello, Spectral flow cytometry, Curr Protoc Cytom Chapter 1 (2013) Unit1 27.

[147] L.A. Hymel, S.E. Anderson, T.C. Turner, W.Y. York, H.S. Lim, P. Qiu, Y.C. Jang, N.J. Willett, E.A. Botchwey, Identifying dysregulated immune cell subsets following critical volumetric muscle loss with pseudo-time trajectories, bioRxiv (2021) 2021.05.25.445480.

[148] S. Schiaffino, A.C. Rossi, V. Smerdu, L.A. Leinwand, C. Reggiani, Developmental myosins: expression patterns and functional significance, Skelet Muscle 5 (2015) 22.

[149] B.T. Corona, J.C. Rivera, J.G. Owens, J.C. Wenke, C.R. Rathbone, Volumetric muscle loss leads to permanent disability following extremity trauma, J Rehabil Res Dev 52(7) (2015) 785-92.

[150] M.T. Li, N.J. Willett, B.A. Uhrig, R.E. Guldberg, G.L. Warren, Functional analysis of limb recovery following autograft treatment of volumetric muscle loss in the quadriceps femoris, J Biomech 47(9) (2014) 2013-21.

[151] F.X. Pizza, J.M. Peterson, J.H. Baas, T.J. Koh, Neutrophils contribute to muscle injury and impair its resolution after lengthening contractions in mice, J Physiol 562(Pt 3) (2005) 899-913.

[152] C. Elabd, W. Cousin, P. Upadhyayula, R.Y. Chen, M.S. Chooljian, J. Li, S. Kung, K.P. Jiang, I.M. Conboy, Oxytocin is an age-specific circulating hormone that is necessary for muscle maintenance and regeneration, Nat Commun 5 (2014) 4082.

[153] F. Langone, S. Cannata, C. Fuoco, D. Lettieri Barbato, S. Testa, A.P. Nardozza, M.R. Ciriolo, L. Castagnoli, C. Gargioli, G. Cesareni, Metformin protects skeletal muscle from cardiotoxin induced degeneration, PLoS One 9(12) (2014) e114018.

[154] X. Luo, Y. Gu, X. Tao, C.N. Serhan, R.R. Ji, Resolvin D5 Inhibits Neuropathic and Inflammatory Pain in Male But Not Female Mice: Distinct Actions of D-Series Resolvins in Chemotherapy-Induced Peripheral Neuropathy, Front Pharmacol 10 (2019) 745.